Multiphase Flow in Porous Media: Dewatering and Consolidation

Zhihao Huangfu

B.Eng (Civil/Struct) (Hons 1)

Thesis submitted in fulfilment of the requirements for the degree of Doctor of Philosophy

The University of Adelaide

Faculty of Sciences, Engineering and Technology

School of Architecture and Civil Engineering

This page is intentionally blank.

Abstract

Multiphase flow in porous media represents one of the most complicated processes that occur in a range of applications across science and engineering disciplines. The complexity escalates when the flows are driven under a negative pressure as often encountered in geotechnical engineering, petroleum exploration, and underground water resource cycling. The proposed study aims to model gas–liquid flows in porous media, calculate deformation of porous media induced by the two-phase flows, and capture pressure variation in vertical drains. This thesis comprises four article publications (Chapters 2 to 5) which are either published or submitted to journals for possible publication by the time of thesis lodgement.

Chapter 1 is the Introduction. This chapter provides an overview of the research, highlights the research gaps, presents the research aims and objectives, and outlines the thesis structure.

Chapter 2 comprises a paper “Large Strain Consolidation of Unsaturated Soil: Model Formulation and Numerical Analysis”. This paper has been published in the ACSE *International Journal of Geomechanics*. The content presents a novel numerical model to simulate the unsaturated soil consolidation utilising the Lagrangian–Convective coordinate system. The proposed model was solved via the explicit finite difference method and was verified against the conventional analytical solution. The developed model enabled the nonlinear soil properties including soil water characteristic curve, shrinkage curve, compressibility curve and permeability curve. A parametric study was conducted to focus on the effect of the initial soil

degree of saturation on the consolidation degree. The results indicated that soil with a higher initial degree of saturation has a greater consolidation settlement, and vice versa.

Chapter 3 presents the second paper manuscript, entitled “Vertical drain aided consolidation and solute transport”, which is under review by *Computers and Geotechnics*. This study coupled the consolidation model in Chapter 2 with the solute transport model and studied the dewatering and solute discharge efficiency under different consolidation conditions. The coupled equations were solved via the alternative direction finite difference time domain method. The model was experimentally verified and then applied to examine the effects of soil saturation conditions, solute transport conditions, and consolidation efforts on solute transport. The results showed that the dispersion process contributes to the solute discharge, whereas the contribution becomes less noticeable in unsaturated conditions. The solute sorption process counteracts the solute transport and delays the clean-up. The consolidation accelerates the transport of reactive chemicals but shows limited effects on the transport of non-reactive chemicals.

Chapter 4 presents the third paper manuscript, entitled “Large strain consolidation model of vacuum and air-booster combined dewatering”. This manuscript was submitted to *Computers and Geotechnics*. The work presented a finite strain model for solving the vacuum and air-booster combined consolidation problem. The model also took account of soil desaturation due to air injection. The model was solved numerically via the alternative direction finite difference time domain method, and the solution was verified against the field test and laboratory measurement.

Chapter 5 contains the fourth paper manuscript, entitled “Modelling air-water flow in the vacuum-aided vertical drain”, which was submitted to *Geosynthetic International*. This modelling work presented a numerical method used to estimate the vacuum-induced two-phase flow pressure distribution along the vertical drain. The soil medium was modelled as the orifice along the vertical drain. The proposed model was validated against the experiment and computational fluid dynamic results. A parametric study was conducted, and the results indicated that the nonlinear pressure distributions occurred in the drainpipe, and the pressure dropped more noticeably in the presence of air. The modelling suggests under one-atmosphere vacuum pressure, the drain lift depth is approximately 6.3 to 7.5m depending on the orifice size.

Chapter 6 is the Summary of this thesis, concluding research contributions achieved and suggestions for further work.

Keywords: Unsaturated soil; Soil consolidation; Large strain consolidation; Computational geomechanics; Dewatering; Ground improvement; Vertical drain; Finite difference method; Nonlinearity； Semi-analytical.

Statement of Originality

I certify that this work contains no material which has been accepted for the award of any other degree or diploma in my name, in any university or other tertiary institution and, to the best of my knowledge and belief, contains no material previously published or written by another person, except where due reference has been made in the text. In addition, I certify that no part of this work will, in the future, be used in a submission in my name, for any other degree or diploma in any university or other tertiary institution without the prior approval of the University of Adelaide and where applicable, any partner institution responsible for the joint-award of this degree.

I acknowledge that copyright of published works contained within this thesis resides with the copyright holder(s) of those works.

I also give permission for the digital version of my thesis to be made available on the web, via the University's digital research repository, the Library Search and also through web search engines, unless permission has been granted by the University to restrict access for a period of time.

Signed: ……Date: 11/07/2023

This page is intentionally blank.

Acknowledgements

I would like to express my deepest gratitude to my supervisors Dr An Deng and Dr Zhao Feng Tian. Your substantial support and mentorship have made this journey viable and enjoyable. A special appreciation goes to Dr Deng for his selfless and detailed technical support, professional suggestions, encouragement, and support over past years. Words cannot express my gratitude especially for his substantial support even after hours or during his leave. I also had the pleasure of working with Dr Tian. His professional suggestions and support from a mechanical engineering perspective have truly broadened my horizons.

Gratitude is also extended to Dr. Chaoshui Xu for his mentorship and suggestions during my undergraduate years, which inspired and paved the way for me to embark on this PhD journey.

I would like to thank all my friends and colleagues in the school for their friendship and support. I am immensely thankful to Dr. Peng Wang, as this endeavour would not have been possible without your invaluable suggestions and support, from the PhD application process to my career development.

I would like to express my heartfelt appreciation to my parents, Mingming Huangfu and Guo Wang, for the countless sacrifices they have made on my behalf over the years. Their unwavering support for my academic pursuits has been invaluable. Appreciate also gives to my fiancée, Shujin Wang, who has been always being patient and

supportive. We are ready to move into the next phase of our life I believe. Lastly, a special mention goes to my fluffy baby, Young Shell. You made my life fantastic.

Lastly, I acknowledge the joint financial support that I have received for my research through the provision of the University of Adelaide and China Scholarship Council (CSC).

This page is intentionally blank.

Table of Contents

Publications Arising from This Thesis

The following peer-reviewed journal paper and unpublished manuscripts are the major outcomes of this research and they form the main body of this thesis.

1. Huangfu, Z., and Deng, A., 2023. Large strain consolidation of unsaturated soil: Model formulation and numerical analysis. International Journal of Geomechanics, 23(9), https://doi.org/10.1061/IJGNAI.GMENG-7120

2. Huangfu, Z., and Deng, A., 2023. Vertical drain aided consolidation and solute transport. Computers and Geotechnics. (Under review).

3. Huangfu, Z., and Deng, A., 2023. Large strain consolidation model of vacuum and air-booster combined dewatering method. Computers and Geotechnics. (Under review).

4. Huangfu, Z., Deng, A., and Tian, Z., 2023. Modelling of orifice induced air-water flow in vertical drains. Geosynthetics International. (Under review)

List of Tables

This page is intentionally blank

List of Figures

This page is intentionally blank.

Chapter 1 Introduction

1.1 Background

Soils with poor engineering properties are commonly found in various locations, including wastewater treatment plants, port lands, marine shores, and artificial islands. These areas are highly valuable for human activities; however, the presence of subsoil profiles with inherent limitations hinders site development. Piling is often regarded as a feasible foundation solution, transferring superstructure loads to underlying firm strata. However, the soils under development are often weak and soft and not in an acceptable shape to provide access to piling machinery.

To upscale ground conditions, dewatering and consolidation can be used to improve the soft soil. The technique densifies the soil by removing the moisture and air from the soil pores. By implementing the soil consolidation, the bearing and shear capacity of the soil are significantly enhanced, thereby rendering shallow foundations a more favorable option compared to costly deep foundations. Common consolidation technologies include the preloading consolidation, vacuum consolidation, electro-osmosis consolidation, and vacuum-air booster consolidation. These methods have been successfully adopted in many ground improvement projects including Indraratna et al. (2011); Shen et al. (2015); Micic et al. (2001) to name a few. Field studies have consistently yielded positive results, demonstrating the capacity of consolidation to enhance soil bearing capacity and shear strength.

The selection of the consolidation technology depends on factors such as in-situ subsoil conditions, site drainage requirement, buried utilities, project budget and timeline. Numerous numerical and analytical models have been proposed to estimate consolidation settlement, time, and the extent of soil improvement. These models range from the conventional preloading consolidation model by Terzaghi (1943) to the more recently vacuum consolidation model by Song et al. (2023). These models aid in scoping ground improvement project planning and managing associated risks.

1.2 Limitation of existing consolidation analysis

The emerged components of liquid, gas and organic matter in the subsurface has been an increasing concern in earth science. However, current studies in ground dewatering and consolidation are mainly focused on the fully saturated subsoils. The presence of air in soil pores are mostly neglected.

Where air is present in soil pores, soil capillary effect governs the consolidation process. The difficulty for researchers in both analytical derivation and numerical simulation lies in soil nonlinear soil behaviour arising from the capillary effect. The capillary effect was first formulated by Leverett (1941) who examined only the subsurface capillary force and associated water flow. Owing to high non-linear behaviour, the inclusion of the capillary effect in two-phase porous media flow can only be solved numerically (Chen 1988; McWhorter and Sunada 1990). In the geotechnical engineering practice, the soil strain induced by capillary effect are commonly depicts by combination of three curves, namely soil water characteristic curve (SWCC), compressibility curve

and shrinkage curve (Fredlund and Morgenstern 1976). The SWCC depicts the soil hydraulic condition by correlating the soil moisture condition with suction level. The compressibility depicts the soil mechanical behaviour by correlating soil void ratio to the applied net stress. The shrinkage curve depicts the correlation between the soil void ratio and moisture condition and hence coupling the soil hydro-mechanical condition. These constitutive relations have been applied to soil consolidation problem since Fredlund and Hasan (1979) in a simple linear form until the recent improved approaches by Qi et al. (2017) and Qi et al. (2020) who utilised the non-linear SWCC, compressibility and shrinkage curves. The utilisation of the non-linear curves enables an accurate mapping of the soil hydro-mechanical state during the consolidation simulation, and hence enhance the model accuracy (Qi et al. 2017). However, models were developed specifically to solve the one-dimensional self-weight and/or preloading consolidation problem.

Soils that require consolidation treatment are clay in nature with poor drainage conditions. Conventional preloading consolidation methods are known time-consuming, and the consolidation degree at deep layers is suboptimal due to the one-way drainage. Installation of the vertical drain, and hence lateral drainage, is considered an alternative solution to accelerating the consolidation. Common consolidation methods utilising the vertical drains are preloading consolidation, vacuum consolidation, air booster consolidation or the combination thereof, and when drain aided soil consolidation is required, it shall be modelled using multi-dimensional models that simulates the lateral and vertical drainage. However, established models are mostly developed based on the fully saturated soil mechanics (Rujikiatkamjorn et al. 2008), despite models are commonly adopted in modelling the unsaturated soil consolidation (Sun and Lu 2023).

To formulate the vertical drain aided consolidation on partially saturated soil, an earlier attempt by Qin et al. (2010) developed a semi-analytical solution by utilising the simplified linear Fredlund and Morgenstern (1976)'s constitutive model. The model was further extended by many researchers incorporating the cyclic loading condition (Wang et al. 2019), analytical solution (Ho et al. 2016a; Ho and Fatahi 2015), and well resistance and smear effect (Chen et al. 2021); however, without improvement on the linear soil parameters. Clayey soils where require the drain-aided consolidation are often associated with the large deformation (Gibson et al. 1981). The deformation causes changes to soil parameters non-linearly, in an exponential or logarithmic function form (Geng & Yu, 2017; Wang et al., 2020). Conventional small strain linear modelling in an Eulerian coordinate system (such as Huang and Zhao 2021; Zhou 2013) is not adequately accurate as it neglects the non-linear changes in soil parameters. Drain-aided partially saturated soil consolidation with large strain non-linear modelling approach is needed.

In addition to the soil consolidation model, when soil is partially saturated and vacuum consolidation is required, the presence of the air in soil pores also reduces the drain well efficiency (Qiu et al. 2007). Where air is present in the drain well, a two-phase flow exists and the mixture pressure drop governs the vacuum pressure distributions (Qiu et al. 2007). Many researcher have contributed to studying the two phase flow pressure drop in vertical drain well Lote et al. (2018). However, developed pressure drop correlations require the inlet flow velocities to be specified. In ground dewatering, gas and liquid flow velocities are not available to calculate pressure distributions. Only outlet vacuum pressure and soil void ratio are specified. Limited model was focused on the pressure distributions in drain wells where only the vacuum pressure and void ratio were available, and hence warrant a

model to study the extent of the pressure drop in the drain well when air phase is present in ground improvement application.

The reviewing of the related studies arrives at the following research gaps: 1) existing drain-aided two-phase porous media dewatering and consolidation models were based on the small strain theory; 2) the two-phase flow pressure gradient in drain wells that is driven by vacuum force was not studied.

1.3 Research aim and objectives

This research aims to study vertical drain induced dewatering and consolidation of partially saturated soil using the finite strain consolidation modelling approach. Three consolidation methods, including drain-aided preloading consolidation, vacuum consolidation and vacuum air-booster consolidation, and their relevant drain efficiency are of interest. Research efforts on these topics will enable greater understanding of the ground improvement method, and hence guide engineering decision on consolidation method selection. For this purpose, the research objectives are:

Objective 1. To propose a finite-strain soil consolidation model on drain-aided consolidation of unsaturated soil

Objective 2. To propose a finite-strain soil consolidation model on vacuum-air booster consolidation considering the soil unsaturation induced by the injected air.

Objective 3. To propose a two-phase flow model for drain well to estimate the pressure distribution in the vertical drain when air phase present.

To achieve the research objectives, following task break down are proposed:

Objective 1:

Task 1.1. To study the effect of soil saturation degree on consolidation efficiency for conventional drain-aided preloading consolidation.

Task 1.2. To study the effect of soil saturation degree on consolidation efficiency for vacuum preloading consolidation.

Task 1.3. To couple the consolidation model with the solute transport model to study the contaminate transport efficiency associate with different consolidation method.

Objective 2:

Task 2.1. To validate the model against the field measurement.

Task 2.2. To suggest a new modelling approach that appropriately model the vacuum air-booster combined consolidation.

Objective 3:

Task 3.1. To study the effect of the air entrance location to the drainage efficiency

Task 3.2. To study the effect of the air entrance quantity to the drainage efficiency

Task 3.3. To propose a new modelling approach that appropriately model the vertical drain pressure distribution when air is present in soil.

1.4 Organisation of the Thesis

The main body of this thesis (Chapters 2 to 5) comprises the collection of four journal articles produced within this research[1]. A summary of the thesis chapters is given below.

Chapter 2 (Journal paper 1) focuses on proposing a finite strain consolidation model for unsaturated soil consolidation and conducing a detailed parametric study to assess the effect of soil unsaturation on soil consolidation efficiency for the drain-aided preloading consolidation method.

Chapter 3 (Journal paper 2) focuses on the coupling of the finite strain unsaturated soil consolidation model with the solute transport model and apply the coupled model on preloading, drain aided preloading, and vacuum preloading consolidation and contaminate transport problem. Moreover, a parametric study conducted evaluating the dewatering and contaminate discharge efficiency associate with different consolidation terminology.

[1] The journal paper manuscripts have been reformatted in accordance with University of Adelaide guidelines, and sections have been renumbered for inclusion within this thesis.

Chapter 4 (Journal paper 3) proposes a finite strain consolidation model for vacuum air booster consolidation method considering the soil unsaturation induced by the pressurised air booster system.

Chapter 5 (Journal paper 3) proposes a two-phase flow model for vertical drain well and conducts a parametric study to assess the effect of the air phase on dewatering efficiency.

Chapter 6 summarises the contributions of the research and recommends research work to undertake in the further.

Chapter 2 Large strain consolidation of unsaturated soil: Model formulation and numerical analysis

Zhihao Huangfu[1], An Deng[2]

[1] School of Architecture and Civil Engineering, The University of Adelaide, Adelaide, SA 5005, Australia.

[2] School of Architecture and Civil Engineering, The University of Adelaide, Adelaide, SA 5005, Australia. (Corresponding author). E-mail: an.deng@adelaide.edu.au

Citation: Huangfu, Z., & Deng, A., 2023. Large strain consolidation of unsaturated soil: Model formulation and numerical analysis. International Journal of Geomechanics, 23(9), https://doi.org/10.1061/IJGNAI.GMENG-7120.

Statement of Authorship

Title of Paper	Large strain consolidation of unsaturated soil: Model formulation and numerical analysis
Publication Status	☑ Published ☐ Accepted for Publication ☐ Submitted for Publication ☐ Unpublished and Unsubmitted w ork w ritten in manuscript style
Publication Details	Huangfu, Z., and Deng, A., 2023. Large strain consolidation of unsaturated soil: Model formulation and numerical analysis. International Journal of Geomechanics, 23(9), https://doi.org/10.1061/IJGNAI.GMENG-7120

Principal Author

Name of Principal Author (Candidate)	Zhihao Huangfu		
Contribution to the Paper	Conception; Acquiring data; Knowledge; Analysis; Drafting		
Overall percentage (%)	85%		
Certification:	This paper reports on original research I conducted during the period of my Higher Degree by Research candidature and is not subject to any obligations or contractual agreements with a third party that would constrain its inclusion in this thesis. I am the primary author of this paper.		
Signature		Date	05 July 2023

Co-Author Contributions

By signing the Statement of Authorship, each author certifies that:

I. the candidate's stated contribution to the publication is accurate (as detailed above);
II. permission is granted for the candidate in include the publication in the thesis; and
III. the sum of all co-author contributions is equal to 100% less the candidate's stated contribution.

Name of Co-Author	An Deng		
Contribution to the Paper	Conception; Knowledge; Analysis; Review		
Signature		Date	6/07/2023

Name of Co-Author			
Contribution to the Paper			
Signature		Date	

Please cut and paste additional co-author panels here as required.

Abstract

A non-linear large strain consolidation model for unsaturated soils is presented. The model uses the Lagrangian−convective coordinate to track the flow of air and water through a deformed layer, and the state surface approach to approximate the hydro-mechanical behaviour of unsaturated soils. The model comprises a set of governing equations to integrate the water flow, air flow and layer consolidation where large strain deformation of the layer occurs. The governing equations were discretised and solved using the finite difference method, with the solutions verified against the analytical answers. The model was implemented to surcharge preloading studies with a focus on the effects of initial wet degree of layers on consolidation. The results suggest that the initial wet degree affects the consolidation curves. Higher consolidation settlement occurs to the wet soil layers than to the less wet layers. In the same layer, the pore air pressure dissipation is completed earlier than the pore water pressure.

Keywords: Unsaturated soil, nonlinearity, large strain consolidation, finite difference method, Lagrangian−convective, varied permeability

2.1 Introduction

Although one usually assumes a saturated condition for consolidation analysis, the soils of concern often are partially saturated due to presence of air. Consolidation in a partially saturated condition involves flow of moisture and air and is relatively complex due to coupled hydro-mechanical behaviour of soils. To this, Fredlund and Morgenstern (1976) analysed hydro-mechanical behaviour of unsaturated soils and proposed a semi-linear constitutive surface for soil deformation caused by flow of air and water. Based on the constitutive surfaces, Fredlund and Hasan (1979) developed the one-dimensional (1D) consolidation model of unsaturated soils. The model was then extended to plane strain (Ho and Fatahi 2015; Huang and Zhao 2021; Liu et al. 2022; Wang et al. 2018, 2020b) and axisymmetric consolidation (Ho et al. 2016b; Jiang et al. 2022; Wang et al. 2020c). These models are valid for small strain consolidation and add to developing large strain consolidation models.

Large strain consolidation needs to use deformable coordinate systems, therefore keeping track of flow of water and air accompanied by soil layer deformation. Deformable coordinate systems enable updating of soil parameters at each time step and therefore provide room to consider soil nonlinearity. Earlier studies have successfully integrated soil nonlinearity in consolidation analyses (e.g. Lloret and Alonso 1980, Qin et al. 2010). Most studies however took account of effects of a single parameter e.g., void ratio or stress. These single-variable approaches work if limited changes occur to the parameters that are assumed constant, for example, when consolidating a relatively thinner layer. Multivariable modelling was conducted in Tang

et al. (2018). They modelled the hydraulic conductivity as a function of two variables, i.e. suction and degree of saturation. Their model also considered the effects of hydraulic hysteresis on consolidation by means of the approach in Khalili et al. (2008). However, their model used the Eulerian system which neglects the layer deformation. The problem can be solved by using a coupled Lagrangian−convective coordinate system (Gibson et al. 1981). In this coupled system, the Lagrangian coordinate represents soil layer deformation and the convective coordinate captures water and air flow. There is a mechanism of communication between the two coordinates at each time step, thus enabling accurate consolidation settlement.

Lagrangian−convective coordinate approaches were adopted in Seneviratne et al. (1996) and Yao et al. (2002). Both studies analysed water and air flow in unsaturated conditions and effects of large strain on consolidation. The unsaturated conditions however were presumed to originate mainly from thermal evaporation. To eliminate the restriction, Qi et al. (2017) examined a general unsaturated condition and developed a numerical model for 1D large strain consolidation of unsaturated soils. The model has capabilities to integrate permeability function (i.e., Shuai 1996) and the compressibility constitutive surface (i.e., Vu and Fredlund 2006). The model was further improved by Qi et al. (2020) that coupled hydro- and mechanical behaviour and assessed the effect of hydraulic hysteresis on consolidation. The model gives excellent results for 1D self-weight consolidation, evaporation decantation, or their combination, but neglected the change in pore-air pressure and compressibility of pore-air. In addition the model in Qi et al. (2020) is limited to one-dimensional consolidation. Ho et al. (2015) proposed a model for 2D plane-strain problems. However, the model in their study is based on the simplified small strain conception and is not suitable for large strain consolidation. These studies are summarised

in Table 2-1. It is suggested that an alternative approach that enables the modelling of large strain consolidation of unsaturated soils in a plane-strain condition is required.

In this study, a 2D model for vertical drain-aided consolidation of unsaturated soils is proposed. This model was developed using a Lagrangian-convective coordinate system. The model considers multivariable functions for void ratio, permeability and compressibility, therefore enabling a greater diversity of soil nonlinearity. The model incorporates two concepts in earlier studies, namely, the large strain approach (Geng and Yu 2017; Gibson et al. 1981) and the constitutive relationships for unsaturated soils (Brooks and Corey 1966, Dakshanamurthy and Fredlund 1980). The developed governing equations are written in conventional diffusion equation forms and therefore are adaptable to most equation-solvers. A finite difference solver was presented, aiming to demonstrate model performance. The model was verified against an analytical solution and implemented to case studies. Some interesting simulation results with respect to the effects of large strain deformation on consolidation of unsaturated soils were presented.

Table 2-1. Comparison of unsaturated soil consolidation models

Coordinate system	Reference	Drained	Solution type	Space dimension	Varied permeability	Varied compressibility
Eulerian	Qin et al. (2010)	Yes	SAS	1D, A	Yes	No
	Zhou (2013)	Yes	NS	1D, A	No	No
	Ho and Fatahi (2015)	Yes	AS	2D, P	No	No
	Ho et al. (2015)	Yes	AS	2D, P	No	No
	Ho et al. (2016)	Yes	AS	2D, A	No	No
	Wang et al. (2018)	Yes	SAS	2D, P	No	No
	Tang et al. (2018)	Yes	NS	1D,2D, P	Yes	Yes
	Wang et al. (2020a)	Yes	SAS	2D, P	No	No
	Huang and Zhao (2021)	Yes	SAS	2D, P	No	No
	Jiang et al. (2022)	Yes	SAS	2D, A	No	No
	Liu et al. (2022)	Yes	AS	2D, P	No	No
Lagrangian-convective	Qi et al. (2017)	No	NS	1D	Yes	Yes
	Qi et al. (2020)	No	NS	1D	Yes	Yes
	This study	Yes	NS	2D, P	Yes	Yes

Note: AS = analytical solution; SAS = semi-analytical solution; NS = numerical solution; A = axisymmetric; P = plane strain.

2.2 Model development

2.2.1 Geometry

A soil layer with a depth of *H* is enclosed laterally by two drain wells installed at a spacing of *L* as shown in Figure 2-1(a). The layer is subjected to a surcharge load *p* on the top boundary. The bottom boundary is impermeable and referred to as the datum. As in Ho and Fatahi (2015), the following assumptions are made: (i) The soil consists of three phases, i.e., solid particles, pore water and pore air, and the soil layer is homogenous at the outset. (ii) Soil particles and water are incompressible. (iii) Flow of water and air leads to soil deformation separately and the deformation is superimposable. (iv) Quasi-steady flow of pore water and pore air occurs in a small time-step increment; the flow is governed by Darcy's and Fick's laws, respectively. (v) Environmental effects, such as temperature, evaporation, and air dissolution in water, are neglected. (vi) Well resistance and smear effect are not considered. (vii) Solely vertical deformation occurs.

The water flow rates in the horizontal and vertical directions are q_x^w and q_ξ^w respectively; the mass flow rates of air in the horizontal and vertical directions are m_x^a and m_ξ^a respectively. The differences between the inflow and outflow contribute to the vertical deformation of the element.

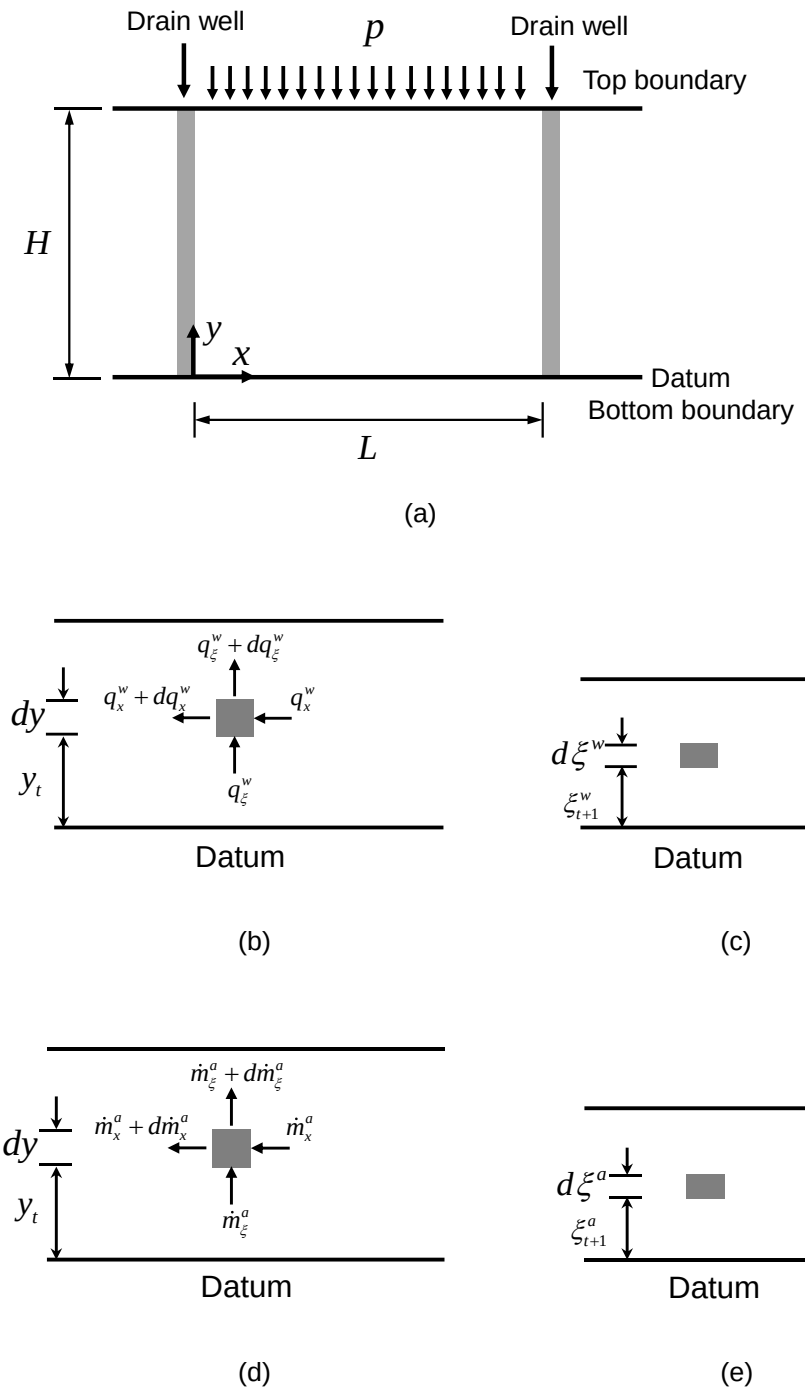

Figure 2-1. Model geometry: (a) soil layer in Lagrangian x–y coordinate system; (b) water flow model in Lagrangian coordinate; (c) water flow model in convective coordinate; (d) airflow in Lagrangian coordinate; and (e) airflow in convective coordinate.

The vertical deformation is calculated by the convective coordinate, ξ. At time step (t + 1), the thickness of element *dxdy* reduces to $\partial\xi^w$ due to water flow and $\partial\xi^a$ due to air flow, or a combination thereof. As a result, the element vertically relocates to ξ_{t+1}^w, ξ_{t+1}^a or a lower elevation due to the combination effect. The local deformation is then summarised and fed to the global coordinate *x*-*y*, updating the soil layer deformation. The coupled Lagrangian−convective coordinate system outperforms an Eulerian coordinate system by calculating the pressure dissipation in a deformable system, thus enabling the computation of accurate consolidation settlement (Geng and Yu 2017; Gibson et al. 1981).

The Lagrangian ordinate *y* and time *t* are independent variables. The convective coordinate ξ is a function of (*y*, *t*) and as per Gibson et al. (1981) and Geng and Yu (2017) is expressed as:

$$\frac{\partial\xi}{\partial y}=\frac{1+e}{1+e_0} \tag{2-1}$$

where e_0 is the initial soil void ratio, and e is the soil void ratio at time t. Break down e as:

$$e=e^a+e^w \tag{2-2}$$

where $e^a = (V^a/V^s)$ is the air void ratio, $e^w = (V^w/V^s)$ is the water void ratio, and V^a, V^w and V^s respectively are the volumes of the air, water and solids. Considering assumption (iii), Eqs. (2-1) and (2-2) are rewritten into:

$$\begin{cases}\dfrac{\partial\xi^w}{\partial y}=\dfrac{1+e^w}{1+e_0^w}\\[2ex]\dfrac{\partial\xi^a}{\partial y}=\dfrac{1+e^a}{1+e_0^a}\end{cases} \tag{2-3}$$

where e_0^w and e_0^a are the initial water and air void ratios, respectively.

2.2.2 Water flow equation

The governing equations for water flow are adapted from the radial consolidation model of saturated soil (Geng and Yu 2017). According to Darcy's law, the apparent velocities of water flow in the vertical and horizontal directions as in Figure 2-1(b), v_ξ^w and v_x^w, are expressed as:

$$\begin{cases} v_\xi^w = -k_\xi^w i_\xi^w \\ v_x^w = -k_x^w i_x^w \end{cases} \tag{2-4}$$

where k_ξ^w, k_x^w are vertical and horizontal permeability of water, respectively; i_ξ^w, i_x^w are the hydraulic gradient in the vertical and horizontal directions respectively and are given as:

$$\begin{cases} i_\xi^w = \dfrac{1}{\gamma^w}\dfrac{\partial u^w}{\partial \xi^w} \\ i_x^w = \dfrac{1}{\gamma^w}\dfrac{\partial u^w}{\partial x} \end{cases} \tag{2-5}$$

where γ^w is unit weight of water, u^w is the (excess) pore water pressure. Using soil phase relationships, the apparent velocities, v_ξ^w and v_x^w, can also be expressed as:

$$\begin{cases} v_\xi^w = \dfrac{e^w}{1+e^w}\left(v_\xi^{w,act} - v_\xi^{s,w}\right) \\ v_x^w = \dfrac{e^w}{1+e^w} v_x^{w,act} \end{cases} \tag{2-6}$$

where $v_\xi^{w,act}$ and $v_x^{w,act}$ are the actual velocity of water in the vertical and horizontal directions respectively, $v_\xi^{s,w}$ is the actual velocity of soil particles in the vertical direction due to water flow, i.e., the soil deformation per unit time, which is a small value.

For soil element *dxdy* in Figure 2-1(b), the water inflow consists of $q_{\xi}^{w} = v_{\xi}^{w} dx$ and $q_{x}^{w} = v_{x}^{w} d\xi$, and the outflow of $q_{\xi}^{w} + \left(\partial v_{\xi}^{w} / \partial \xi\right) d\xi dx$ and $q_{x}^{w} + \left(\partial v_{x}^{w} / \partial x\right) dx d\xi$. The change of flow, dq^{w}, is $\left(\partial v_{\xi}^{w} / \partial \xi\right) d\xi dx + \left(\partial v_{x}^{w} / \partial x\right) dx d\xi$. Substituting Eq. (6) to dq^{w} yields

$$dq^{w} = \left\{ \frac{\partial}{\partial \xi} \left[\frac{e^{w}}{1+e^{w}} \left(v_{\xi}^{w,act} - v_{\xi}^{s,w} \right) \right] d\xi \right\} dx + \left\{ \frac{\partial}{\partial x} \left[\frac{e^{w}}{1+e^{w}} v_{x}^{w,act} \right] dx \right\} d\xi \tag{2-7}$$

The change of flow is equal to the water flow induced change of soil volume, dV^{w}. Based on soil phase relationships, dV^{w} can be expressed as a function of water void ratio e^{w}:

$$dV^{w} = -\frac{1}{1+e^{w}} \frac{\partial e^{w}}{\partial t} d\xi dx \tag{2-8}$$

Combining Eqs. (2-7) and (2-8) gives

$$-\frac{1}{1+e^{w}} \frac{\partial e^{w}}{\partial t} = \frac{\partial}{\partial \xi} \left[\frac{e^{w}}{1+e^{w}} \left(v_{\xi}^{w,act} - v_{\xi}^{s,w} \right) \right] + \frac{\partial}{\partial x} \left(\frac{e^{w}}{1+e^{w}} v_{x}^{w,act} \right) \tag{2-9}$$

Substituting Eqs. (2-3)−(2-6) to Eq. (2-9) leads to:

$$\frac{\partial e^{w}}{\partial t} = \frac{k_{x}^{w} \left(1+e^{w}\right)}{\gamma^{w}} \frac{\partial^{2} u^{w}}{\partial x^{2}} + \frac{k_{\xi}^{w} \left(1+e^{w0}\right)^{2}}{\gamma^{w} \left(1+e^{w}\right)} \frac{\partial^{2} u^{w}}{\partial y^{2}} \tag{2-10}$$

Eq. (2-10) gives the water flow continuity relationship. The water void ratio e^{w} is expressed as a function of time *t*, location (*x*, *y*), and the pore water pressure u^{w}. The permeability coefficients, k_{x}^{w} and k_{ξ}^{w}, are determined experimentally.

2.2.3 Air flow equation

According to Fick's law, the air mass fluxes, m_{ξ}^{a} and m_{x}^{a}, are expressed as:

$$\begin{cases} m_{\xi}^{a} = -\dfrac{k_{\xi}^{a}}{g}\dfrac{\partial u^{a}}{\partial \xi} \\ m_{x}^{a} = -\dfrac{k_{x}^{a}}{g}\dfrac{\partial u^{a}}{\partial x} \end{cases} \tag{2-11}$$

where k_{ξ}^{a} and k_{x}^{a} respectively are the vertical and horizontal permeability of air (or air diffusivity) and determined experimentally, *g* is the gravitational acceleration and equals 9.81 m/s^2, and u^a is the (excess) pore air pressure.

Alternatively, the air mass fluxes m_{ξ}^{a} and m_{x}^{a} can be expressed as a relation of the air void ratio e^a:

$$\begin{cases} m_{\xi}^{a} = \rho^{a}\dfrac{e^{a}}{1+e^{a}}\left(v_{\xi}^{a,act} - v_{\xi}^{s,a}\right) \\ m_{x}^{a} = \rho^{a}\dfrac{e^{a}}{1+e^{a}}v_{x}^{a,act} \end{cases} \tag{2-12}$$

where $v_{\xi}^{a,act}$ and $v_{x}^{a,act}$ are the actual velocity of air in the vertical and horizontal directions respectively, $v_{\xi}^{s,a}$ is the velocity of soil particles in the vertical direction due to air flow, and ρ^{a} is the density of air and, using the ideal gas law, is expressed as:

$$\rho^{a} = \frac{\omega}{R\theta}u_{pore}^{a} \tag{2-13}$$

where ω is the molecular mass of air and equals 0.029 kg/mol, *R* is the universal constant and equals 8.314 J/mol/K, θ is the temperature in Kelvin scale, and u_{pore}^{a} is the absolute pore air pressure and equals $u^{a} + u_{atm}^{a}$ where u_{atm}^{a} is the standard atmosphere of 101,325 Pa.

Similar to the water flow, the air flow through soil element *dxdy* in Figure 2-1(c) leads to the difference of air flow mass, $d\dot{m}_{\xi}^{a}$ and $d\dot{m}_{x}^{a}$.

Based on Eq.(2-12), $d\dot{m}_{\xi}^{a}$ and $d\dot{m}_{x}^{a}$ are written as:

$$\begin{cases} d\dot{m}_{\xi}^{a} = \left\{ \dfrac{\partial}{\partial \xi} \left[\rho^{a} \dfrac{e^{a}}{1+e^{a}} \left(v_{\xi}^{a,act} - v_{\xi}^{s,a} \right) \right] d\xi \right\} dx \\ d\dot{m}_{x}^{a} = \left[\dfrac{\partial}{\partial x} \left(\rho^{a} \dfrac{e^{a}}{1+e^{a}} v_{x}^{a,act} \right) dx \right] d\xi \end{cases} \tag{2-14}$$

Therefore, the total air flow mass difference, $d\dot{m}^{a}$, is:

$$d\dot{m}^{a} = d\dot{m}_{\xi}^{a} + d\dot{m}_{x}^{a} \tag{2-15}$$

By density definition, the air mass change of the element, dM^{a}, is calculated as:

$$dM^{a} = \rho^{a} dV^{a} + V^{a} d\rho^{a} \tag{2-16}$$

where dV^{a} is the change of air volume and is expressed using the air void ratio, e^{a}, as:

$$dV^{a} = -\frac{1}{1+e^{a}} \frac{\partial e^{a}}{\partial t} d\xi dx \tag{2-17}$$

Using phase relationships, volume of air V^{a} can be written as:

$$V^{a} = \frac{e^{a}}{1+e} d\xi dx \tag{2-18}$$

Based on the law of continuity, i.e., $d\dot{m}^{a} = dM^{a}$, Eqs. (2-15) and (2-16) are combined into:

$$-\frac{1}{1+e^{a}} \frac{\partial e^{a}}{\partial t} + \frac{e^{a}}{1+e} \frac{\partial \rho^{a}}{\partial t} = \frac{\partial}{\partial \xi} \left[\rho^{a} \frac{e^{a}}{1+e^{a}} \left(v_{\xi}^{a,act} - v_{\xi}^{a,s} \right) \right] + \frac{\partial}{\partial x} \left[\rho^{a} \frac{e^{a}}{1+e^{a}} v_{x}^{a,act} \right] \tag{2-19}$$

Substituting Eqs. (2-11) and (2-13) to Eq. (2-19) and rearranging the equation, gives

$$\frac{\partial e^a}{\partial t} = -\frac{e^a(1+e^w)}{(1+e)\left(u^a+u^a_{atm}\right)}\frac{\partial u^a}{\partial t} + \frac{k^a_x\left(1+e^a\right)R\theta}{\omega g\left(u^a+u^a_{atm}\right)}\frac{\partial^2 u^a}{\partial x^2} + \frac{k^a_\xi\left(1+e^a_0\right)^2 R\theta}{\omega g\left(1+e^a\right)\left(u^a+u^a_{atm}\right)}\frac{\partial^2 u^a}{\partial y^2} \quad (2\text{-}20)$$

Eq. (2-20) is the air flow equation. This equation provides the air void ratio e^a as a function of time t, location (x, y), pore air pressure u^a, and void ratio e. Parameter e^w is determined from Eq. (2-10). Permeability coefficients k^a_x and k^a_ξ .are determined experimentally.

2.2.4 Consolidation equation

The volume change of element *dxdy* in Figure 2-1(a), *dV*, consists of the volume changes of water and air, dV^w and dV^a. The volume changes are proportional to the initial volumes of the soil element, V_0, as follows:

$$\frac{dV}{V_0} = \frac{dV^w}{V_0} + \frac{dV^a}{V_0} \quad (2\text{-}21)$$

The term dV/V_0 can be determined from the methods proposed in Fredlund and Morgenstern (1976) and Alonso et al. (1990). Alonso et al. (1990) offered an elastoplastic framework and the framework was extended for example by Wheeler et al. (2003) and Pedroso and Farias (2011) to assess cyclic behaviour of unsaturated soil. Qi et al. (2020) however suggested the state surface model in Vu and Fredlund (2006) offers relatively greater flexibility with constitutive relations and better determination of inter-element flow. Meanwhile the state surface approach enables modelling from saturated to unsaturated conditions more conveniently. As per Dakshanamurthy and Fredlund (1980), dV/V_0 is given as:

$$\frac{dV}{V_0} = m_1\left[d\left(\sigma_x - u^a_{pore}\right) + d\left(\sigma_y - u^a_{pore}\right)\right] + m_2 d\left(u^a_{pore} - u^w_{pore}\right) \quad (2\text{-}22)$$

where σ_x and σ_y are the soil total stresses in x and y directions respectively, *and* m_1 and m_2 are the coefficients of soil volume

compressibility with respect to the net stress, ($\sigma_x - u^a_{pore}$)+($\sigma_y - u^a_{pore}$), and the matric suction, ($u^a_{pore}-u^w_{pore}$), respectively. The u^w_{pore} is the absolute pore water pressure and equals ($u^w+u^w_{hydro}$), and u^w_{hydro} is the hydrostatic pore water pressure. Similarly, the terms dV^w/V_0 and dV^a/V_0 are written as:

$$\begin{cases} \dfrac{dV^w}{V_0} = m_1^w\left[d\left(\sigma_x - u^a_{pore}\right) + d\left(\sigma_y - u^a_{pore}\right)\right] + m_2^w d\left(u^a_{pore} - u^w_{pore}\right) \\ \dfrac{dV^a}{V_0} = m_1^a\left[d\left(\sigma_x - u^a_{pore}\right) + d\left(\sigma_y - u^a_{pore}\right)\right] + m_2^a d\left(u^a_{pore} - u^w_{pore}\right) \end{cases} \tag{2-23}$$

where m_1^w, m_2^w, m_1^a and m_2^a are the coefficients of water and air volume change per unit change of the net stress and matric suction, respectively.

Substituting Eq. (2-2) to Eq. (2-23) and taking derivative for time *t*, leads to:

$$\begin{cases} \dfrac{\partial e^w}{\partial t} = \left(1+e_0\right)\left[m_1^w \dfrac{\partial}{\partial t}\left(\sigma_x - u^a_{pore}\right) + m_1^w \dfrac{\partial}{\partial t}\left(\sigma_y - u^a_{pore}\right) + m_2^w \dfrac{\partial}{\partial t}\left(u^a_{pore} - u^w_{pore}\right)\right] \\ \dfrac{\partial e^a}{\partial t} = \left(1+e_0\right)\left[m_1^a \dfrac{\partial}{\partial t}\left(\sigma_x - u^a_{pore}\right) + m_1^a \dfrac{\partial}{\partial t}\left(\sigma_y - u^a_{pore}\right) + m_2^a \dfrac{\partial}{\partial t}\left(u^a_{pore} - u^w_{pore}\right)\right] \end{cases} \tag{2-24}$$

Considering a vertically deformed layer, Eq. (2-24) is written as

$$\begin{cases} \dfrac{\partial e^w}{\partial t} = \left(1+e_0\right)\left[2m_1^w \dfrac{\partial \sigma}{\partial t} + \left(m_2^w - 2m_1^w\right)\dfrac{\partial u^a_{pore}}{\partial t} - m_2^w \dfrac{\partial u^w_{pore}}{\partial t}\right] \\ \dfrac{\partial e^a}{\partial t} = \left(1+e_0\right)\left[2m_1^a \dfrac{\partial \sigma}{\partial t} + \left(m_2^a - 2m_1^a\right)\dfrac{\partial u^a_{pore}}{\partial t} - m_2^a \dfrac{\partial u^w_{pore}}{\partial t}\right] \end{cases} \tag{2-25}$$

The changes of total stress with respect to time, $\partial\sigma/\partial t$, for water and air respectively are expressed as:

$$\begin{cases} \dfrac{\partial \sigma}{\partial t} = \dfrac{\partial \sigma}{\partial \xi^w}\dfrac{\partial \xi^w}{\partial t} \\ \dfrac{\partial \sigma}{\partial t} = \dfrac{\partial \sigma}{\partial \xi^a}\dfrac{\partial \xi^a}{\partial t} \end{cases} \tag{2-26}$$

where, term $\partial\sigma / \partial\xi$ as per Fredlund et al. (2012) is:

$$\frac{\partial \sigma}{\partial \xi} = \rho g \tag{2-27}$$

and term $\partial\xi / \partial t$, the coordinate deformation with respect to time, is expressed in terms of void ratio as:

$$\begin{cases} \dfrac{\partial \xi^w}{\partial t} = -\triangle y \dfrac{1}{1+e_0}\dfrac{\partial e^w}{\partial t} \\ \dfrac{\partial \xi^a}{\partial t} = -\triangle y \dfrac{1}{1+e_0}\dfrac{\partial e^a}{\partial t} \end{cases} \tag{2-28}$$

where ρ is the density of the element and Δy is the initial height of the element. Similarly, the change of pore water pressure is associated with the change of element height, as:

$$\begin{cases} \dfrac{\partial u^w_{pore}}{\partial t} = \rho_w g \dfrac{\partial \xi^w}{\partial t} + \dfrac{\partial u^w}{\partial t} \\ \dfrac{\partial u^w_{pore}}{\partial t} = \rho_w g \dfrac{\partial \xi^a}{\partial t} + \dfrac{\partial u^w}{\partial t} \end{cases} \tag{2-29}$$

Substituting Eqs. (2-26) to (2-29) into Eq. (2-25), the change of water and air void ratios with respect to time are:

$$\begin{cases} \dfrac{\partial e^w}{\partial t} = \dfrac{\left(1+e_0\right)}{\left[1+g\triangle y\left(2m_1^w\rho - m_2^w\rho_w\right)\right]}\left[\left(m_2^w - 2m_1^w\right)\dfrac{\partial u^a_{pore}}{\partial t} - m_2^w\dfrac{\partial u^w}{\partial t}\right] \\ \dfrac{\partial e^a}{\partial t} = \dfrac{\left(1+e_0\right)}{\left[1+g\triangle y\left(2m_1^a\rho - m_2^a\rho_w\right)\right]}\left[\left(m_2^a - 2m_1^a\right)\dfrac{\partial u^a_{pore}}{\partial t} - m_2^a\dfrac{\partial u^w}{\partial t}\right] \end{cases} \tag{2-30}$$

The integration of Eq. (2-30) yields water and air void ratios, e^w and e^a, at time t, as:

$$\begin{cases} e_t^w = e_{t\text{-}1}^w + \dfrac{(1+e_0)}{\left[1+g_{\triangle y}\left(2m_1^w\rho - m_2^w\rho_w\right)\right]}\left[\left(m_2^w - 2m_1^w\right)\left(u_t^a - u_{t\text{-}1}^a\right) - m_2^w\left(u_t^w - u_{t\text{-}1}^w\right)\right] \\ e_t^a = e_{t\text{-}1}^a + \dfrac{(1+e_0)}{\left[1+g_{\triangle y}\left(2m_1^a\rho - m_2^a\rho_w\right)\right]}\left[\left(m_2^a - 2m_1^a\right)\left(u_t^a - u_{t\text{-}1}^a\right) - m_2^a\left(u_t^w - u_{t\text{-}1}^w\right)\right] \end{cases} \quad (2\text{-}31)$$

Note that the operation signs of m_1^w, m_2^w, m_1^a and m_2^a have accounted for the effects of the net stress and matric suction on the water and air void ratios.

Replacing terms $\partial e^w / \partial t$ and $\partial e^a / \partial t$ in Eq. (2-30) with Eqs. (2-10) and (2-20) respectively gives:

$$\frac{\partial u^w}{\partial t} = \frac{\left(m_2^w - 2m_1^w\right)}{m_2^w}\frac{\partial u^a}{\partial t} - \frac{k_x^w\left(1+e^w\right)\left[1+g_{\triangle y}\left(2m_1^w\rho - m_2^w\rho_w\right)\right]}{\gamma^w m_2^w\left(1+e_0\right)}\frac{\partial^2 u^w}{\partial x^2} - \frac{k_\xi^w\left(1+e^{w0}\right)^2\left[1+g_{\triangle y}\left(2m_1^w\rho - m_2^w\rho_w\right)\right]}{\gamma^w m_2^w\left(1+e^w\right)\left(1+e_0\right)}\frac{\partial^2 u^w}{\partial y^2} \quad (2\text{-}32)$$

$$\begin{aligned} \frac{\partial u^a}{\partial t} = {} & \frac{m_2^a\left(1+e_0\right)\left(1+e\right)\left(u^a + u_{atm}^a\right)}{\left(1+e_0\right)\left(1+e\right)\left(m_2^a - 2m_1^a\right)\left(u^a + u_{atm}^a\right) + e^a\left(1+e^w\right)\left[1+g_{\triangle y}\left(2m_1^a\rho - m_2^a\rho_w\right)\right]}\frac{\partial u^w}{\partial t} \\ & + \frac{k_x^a R\theta\left(1+e^a\right)\left(1+e\right)\left[1+g_{\triangle y}\left(2m_1^a\rho - m_2^a\rho_w\right)\right]}{\omega g\left\{\left(1+e_0\right)\left(1+e\right)\left(m_2^a - 2m_1^a\right)\left(u^a + u_{atm}^a\right) + e^a\left(1+e^w\right)\left[1+g_{\triangle y}\left(2m_1^a\rho - m_2^a\rho_w\right)\right]\right\}}\frac{\partial^2 u^a}{\partial x^2} \\ & + \frac{k_\xi^a R\theta\left(1+e\right)\left(1+e_0^a\right)^2\left[1+g_{\triangle y}\left(2m_1^a\rho - m_2^a\rho_w\right)\right]}{\omega g\left(1+e^a\right)\left\{\left(1+e_0\right)\left(1+e\right)\left(m_2^a - 2m_1^a\right)\left(u^a + u_{atm}^a\right) + e^a\left(1+e^w\right)\left[1+g_{\triangle y}\left(2m_1^a\rho - m_2^a\rho_w\right)\right]\right\}}\frac{\partial^2 u^a}{\partial y^2} \end{aligned} \quad (2\text{-}33)$$

Eqs. (2-32) and (2-33) are the equations coupling pore air and pore water pressure dissipation in soils. The water and air void ratios e^w and e^a are determined from Eq. (2-31). The permeability coefficients, k_x^w, k_ξ^w, k_x^a and k_ξ^a, and the compressibility coefficients, m_1^w, m_2^w, m_1^a and m_2^a, are variables and determined separately.

2.2.5 Determination of permeability and compressibility

Air and water permeability coefficients, k_x^w, k_ξ^w, k_x^a and k_ξ^a, are varied nonlinearly with soil hydro-mechanical properties (Fredlund and Morgenstern 1976, Ba-Te et al. 2005). As per Brooks and Corey (1964) and Fredlund et al. (2012), water and air permeability coefficients are expressed respectively as:

$$k^w = k_s^w \left(\frac{a_f}{\psi} \right)^{2+3^\lambda} \tag{2-34}$$

$$k^a = k_d^a \left[1 - \left(\frac{a_f}{\psi} \right)^\lambda \right]^2 \left[1 - \left(\frac{a_f}{\psi} \right)^{2+\lambda} \right] \tag{2-35}$$

where k_s^w is the water permeability measured in the saturated condition, k_d^a is the air permeability in the dry condition, a_f is the air-entry suction, matric suction $\psi = (u^a_{pore} - u^w_{pore})$, and λ is the pore-distribution parameter determined from the water retention curve.

Substituting Eq. (2-34) for the permeability coefficients in Eq. (2-32), the water pressure dissipation equation gives:

$$\frac{\partial u^w}{\partial t} = W_1 \frac{\partial u^a}{\partial t} + W_2 \frac{\partial^2 u^w}{\partial x^2} + W_3 \frac{\partial^2 u^w}{\partial y^2} \tag{2-36}$$

where coefficients of consolidations W_1, W_2 and W_3 are:

$$\begin{cases} W_1 = \dfrac{m_2^w - 2m_1^w}{m_2^w} \\ W_2 = -\dfrac{k_{s,x}^w \left(\dfrac{a_f}{\psi}\right)^{2+3^\lambda} \left(1+e^w\right)\left[1+g\triangle y\left(2m_1^w\rho - m_2^w\rho_w\right)\right]}{\gamma^w m_2^w \left(1+e_0\right)} \\ W_3 = -\dfrac{k_{s,\xi}^w \left(\dfrac{a_f}{\psi}\right)^{2+3^\lambda} \left(1+e^{w0}\right)^2\left[1+g\triangle y\left(2m_1^w\rho - m_2^w\rho_w\right)\right]}{\gamma^w m_2^w \left(1+e^w\right)\left(1+e_0\right)} \end{cases} \tag{2-37}$$

where $k_{s,x}^w$ and $k_{s,\xi}^w$ are the horizontal and vertical permeability coefficients of water in saturated conditions, respectively. Similarly, substituting Eq. (2-35) for the permeability coefficients in Eq. (2-33), the air pressure dissipation equation is written into:

$$\frac{\partial u^a}{\partial t} = A_1 \frac{\partial u^w}{\partial t} + A_2 \frac{\partial^2 u^a}{\partial x^2} + A_3 \frac{\partial^2 u^a}{\partial y^2} \tag{2-38}$$

where coefficients of consolidations A_1, A_2 and A_3 are:

$$\begin{cases} A_1 = \dfrac{m_2^a\left(1+e_0\right)\left(1+e\right)\left(u^a + u_{atm}^a\right)}{\left(1+e_0\right)\left(1+e\right)\left(m_2^a - 2m_1^a\right)\left(u^a + u_{atm}^a\right) + e^a\left(1+e^w\right)\left[1+g\triangle y\left(2m_1^a\rho - m_2^a\rho_w\right)\right]} \\ A_2 = \dfrac{k_{d,x}^a\left[1-\left(\dfrac{a_f}{\psi}\right)^\lambda\right]^2\left[1-\left(\dfrac{a_f}{\psi}\right)^{2+\lambda}\right] R\theta\left(1+e^a\right)\left(1+e\right)\left[1+g\triangle y\left(2m_1^a\rho - m_2^a\rho_w\right)\right]}{\omega g\left\{\left(1+e_0\right)\left(1+e\right)\left(m_2^a - 2m_1^a\right)\left(u^a + u_{atm}^a\right) + e^a\left(1+e^w\right)\left[1+g\triangle y\left(2m_1^a\rho - m_2^a\rho_w\right)\right]\right\}} \\ A_3 = \dfrac{k_{d,\xi}^a\left[1-\left(\dfrac{a_f}{\psi}\right)^\lambda\right]^2\left[1-\left(\dfrac{a_f}{\psi}\right)^{2+\lambda}\right] R\theta\left(1+e\right)\left(1+e_0^a\right)^2\left[1+g\triangle y\left(2m_1^a\rho - m_2^a\rho_w\right)\right]}{\omega g\left(1+e^a\right)\left\{\left(1+e_0\right)\left(1+e\right)\left(m_2^a - 2m_1^a\right)\left(u^a + u_{atm}^a\right) + e^a\left(1+e^w\right)\left[1+g\triangle y\left(2m_1^a\rho - m_2^a\rho_w\right)\right]\right\}} \end{cases} \tag{2-39}$$

where $k_{d,x}^a$ and $k_{d,\xi}^a$ are the horizontal and vertical permeability coefficients of air at dry conditions, respectively.

Similar nonlinearity occurs to the compressibility coefficients, m_1, m_2, m_1^w, m_2^w, m_1^a and m_2^a. The six coefficients are reduced to four using the

continuity relationships, i.e., $m_1^w + m_1^a = m_1$ and $m_2^w + m_2^a = m_2$. Fredlund et al. (2012) graphically represented the four compressibility coefficients, m_1, m_2, m_1^w and m_2^w, in a volume−stress space as given in Figure 2-2 and suggested to determine the coefficients using Eq. (2-40):

$$\begin{cases} m_1 = \dfrac{a_t}{1+e_0} \\ m_2 = \dfrac{a_m}{1+e_0} \\ m_1^w = \dfrac{b_t G_s}{1+e_0} \\ m_2^w = \dfrac{b_m G_s}{1+e_0} \end{cases} \tag{2-40}$$

where, a_t and a_m are the coefficients of soil void ratio change at constant suction and net stress respectively, b_t and b_m are the coefficients of water content change at constant suction and net stress respectively, and G_s is the specific gravity of solids. As per Fredlund et al. (2012) and Shuai (1996), coefficients a_t and b_m are determined experimentally, i.e., a_t from a compressibility curve of constant suction, b_m from a water retention curve of constant net stress. Coefficient a_m is determined from coefficient b_m through shrinkage curves; coefficient b_t can be computed as (a_t /G_s) in saturated conditions and a function of {a_t, ψ} in partially saturated conditions.

It is noteworthy that integrating varied permeability and compressibility to soil consolidation offers capabilities in capturing the hydro-mechanical behaviour of a broader spectrum of soils. The capabilities are in favour of examining relatively thicker, more compressible, or drier soils.

Widely accepted hydro-mechanical models (e.g. Fredlund and Xing 1994, Shuai 1996, Pham and Fredlund 2011, Sheng et al. 2008, Zhou et al. 2012, Zhou and Sheng 2015) are used or considered in this study to demonstrate the capabilities, whereas other hydro-mechanical models can also be used to solve for consolidation of unsaturated soils. The consolidation equations (i.e., Eqs. (36) and (38)) are coupled due to pore water−pore air interactions. In addition, the equations are non-linear, second-order partial differential equations, with major parameters (i.e., W_1, W_2, W_3, A_1, A_2 and A_3) related to nonlinear soil properties (i.e. k, e, m, u^a and u^w). This means the equations are preferably solved by means of numerical solutions.

2.3 Numerical solutions

Although the finite element method works satisfactorily on a material coordinate space, it suffers a degree of instability on the fluid flow phenomena. To this, the finite difference approach can capture pore water and air pressure dissipation and is favourable for large strain consolidation (Fox and Berles 1997; Zhou et al. 2013). The finite difference approach is also versatile to capture a range of material properties and geometry as a function of time and location and therefore is used to solve for the consolidation equations.

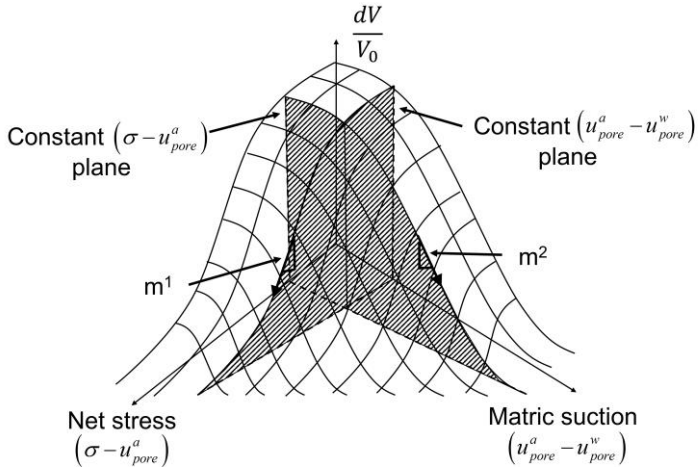

(a)

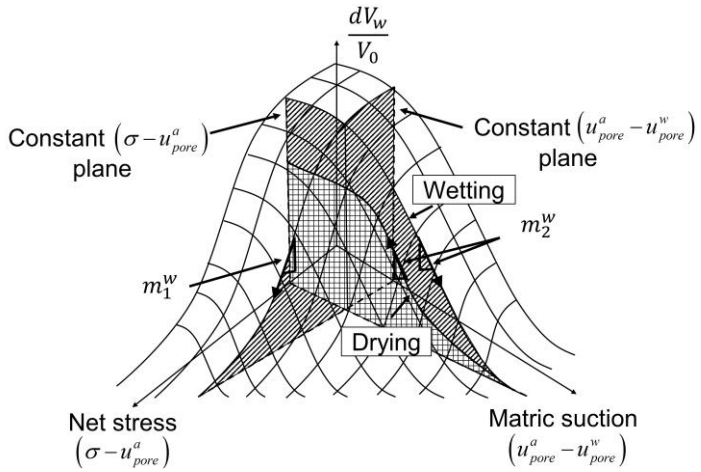

(b)

Figure 2-2. Compressibility constitutive surfaces of unsaturated soil in a volume–stress space for (a) volume of soil; and (b) volume of water. (Adapted from Fredlund et al. (2012))

An explicit forward time centred space (FTCS) method is used to couple the flow of water and air (Dakshanamurthy and Fredlund 1980, Wang et al. 2019). Despite the fact that the method is conditionally stabile, the stabilisation and accuracy of the model are determined by the selection of the time step and the mesh size, as illustrated in Eq.

(2-48). The coupling is illustrated in Figure 2-3. The soil layer of $L \times H$ is discretised into a $M \times N$ mesh, with each element of $\Delta x \times \Delta y$. Node (i, j), where $i = 1, 2, \ldots, M$, and $j = 1, 2, \ldots, N$, represents soil properties and consolidation characteristics at the locations of interest. The mesh develops in time domain t, at the time step increment Δt, until the time step $z\Delta t$, where the time step number $z = 0, 1, 2\ldots, \infty$. The mesh applies to water and air phases separately, while showing interactions between the meshes to solve for the coupled consolidation equations.

Nodes A and C, as well as the neighbour nodes, that are pre-set with initial conditions at $t = 0$ contribute to obtaining nodes B and D of the same locations at $t = \Delta t$ by means of differencing for Eqs. (2-36) and (2-38), which gives:

$$\begin{aligned}\frac{u^w_{t+1}(i,j)-u^w_t(i,j)}{\Delta t} &= W_1\frac{u^a_{t+1}(i,j)-u^a_t(i,j)}{\Delta t}\\ &+W_2\frac{u^w_t(i+1,j)-2u^w_t(i,j)+u^w_t(i-1,j)}{\Delta x^2}\\ &+W_3\frac{u^w_t(i,j+1)-2u^w_t(i,j)+u^w_t(i,j-1)}{\Delta y^2}\end{aligned} \tag{2-41}$$

and

$$\begin{aligned}\frac{u^a_{t+1}(i,j)-u^a_t(i,j)}{\Delta t} &= A_1\frac{u^w_{t+1}(i,j)-u^w_t(i,j)}{\Delta t}\\ &+A_2\frac{u^a_t(i+1,j)-2u^a_t(i,j)+u^a_t(i-1,j)}{\Delta x^2}\\ &+A_3\frac{u^a_t(i,j+1)-2u^a_t(j,i)+u^a_t(i,j-1)}{\Delta y^2}\end{aligned} \tag{2-42}$$

Combining for Eqs. (2-41) and (2-42), gives

$$
\begin{aligned}
u_{t+1}^{w}(i,j) = u_t^{w}(i,j) \\
&+ \frac{A_2 W_1}{1 - A_1 W_1} \frac{\Delta t}{\Delta x^2} \left[u_t^{a}(i+1,j) - 2u_t^{a}(i,j) + u_t^{a}(i-1,j) \right] \\
&+ \frac{A_3 W_1}{1 - A_1 W_1} \frac{\Delta t}{\Delta y^2} \left[u_t^{a}(i,j+1) - 2u_t^{a}(i,j) + u_t^{a}(i,j-1) \right] \\
&+ \frac{W_2}{1 - A_1 W_1} \frac{\Delta t}{\Delta x^2} \left[u_t^{w}(i+1,j) - 2u_t^{w}(i,j) + u_t^{w}(i-1,j) \right] \\
&+ \frac{W_3}{1 - A_1 W_1} \frac{\Delta t}{\Delta y^2} \left[u_t^{w}(i,j+1) - 2u_t^{w}(i,j) + u_t^{w}(i,j-1) \right]
\end{aligned}
\tag{2-43}
$$

and

$$
\begin{aligned}
u_{t+1}^{a}(i,j) = u_t^{a}(i,j) \\
&+ \frac{A_1 W_2}{1 - A_1 W_1} \frac{\Delta t}{\Delta x^2} \left[u_t^{w}(i+1,j) - 2u_t^{w}(i,j) + u_t^{w}(i-1,j) \right] \\
&+ \frac{A_1 W_3}{1 - A_1 W_1} \frac{\Delta t}{\Delta y^2} \left[u_t^{w}(i,j+1) - 2u_t^{w}(i,j) + u_t^{w}(i,j-1) \right] \\
&+ \frac{A_2}{1 - A_1 W_1} \frac{\Delta t}{\Delta x^2} \left[u_t^{a}(i+1,j) - 2u_t^{a}(i,j) + u_t^{a}(i-1,j) \right] \\
&+ \frac{A_3}{1 - A_1 W_1} \frac{\Delta t}{\Delta y^2} \left[u_t^{a}(i,j+1) - 2u_t^{a}(i,j) + u_t^{a}(i,j-1) \right]
\end{aligned}
\tag{2-44}
$$

If the upper boundary is permeable, $u_t^{w}\big|_{j=N} = 0$ and $u_t^{a}\big|_{j=N} = 0$; otherwise, $\partial u_t^{a} / \partial y\big|_{j=N}$ = 0 and $\partial u_t^{w} / \partial y\big|_{j=N}$ = 0. The drain wells are permeable, i.e., $u_t^{w}\big|_{i=1,M} = 0$ and $u_t^{a}\big|_{i=1,M} = 0$. At *t* = 0, the initial pore water and pore air pressures, u_0^{w} and u_0^{a}, that arise from the surcharge load *p* are determined from the approach in Fredlund et al. (2012). The details are given in Appendix A.

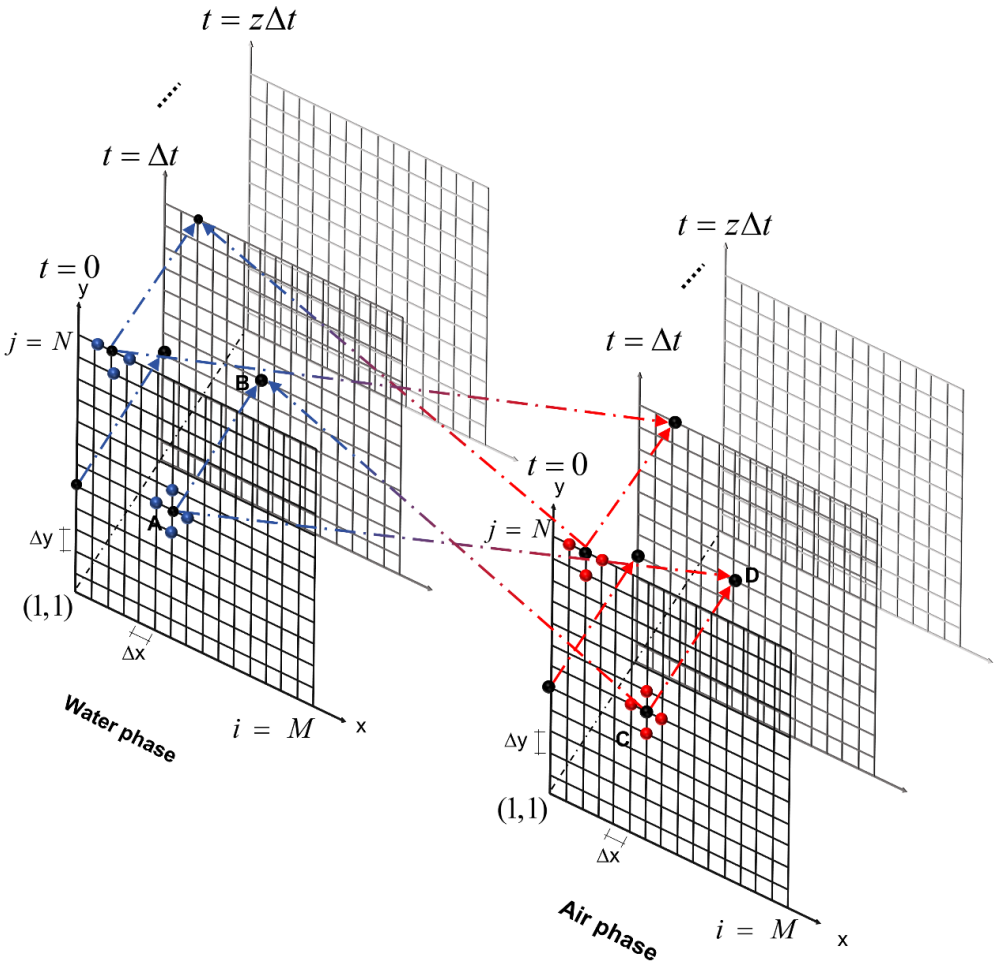

Figure 2-3. Diagram of coupled water–air finite-difference model.

As per Ho et al. (2015), the average pore water and pore air pressures at time *t*, $\bar{u}_t^w$ and $\bar{u}_t^a$, can be obtained as:

$$\begin{cases} \bar{u}_t^w = \dfrac{1}{MN}\sum_{j=1}^{M}\sum_{i=1}^{N} u_t^w(i,j) \\ \bar{u}_t^a = \dfrac{1}{MN}\sum_{j=1}^{M}\sum_{i=1}^{N} u_t^a(i,j) \end{cases} \tag{2-45}$$

Integrating Eq. (2-22) in time domain, the volumetric strain of the layer at time *t*, ε_t, is:

$$\varepsilon_t = \varepsilon_{t-1} + (m_2^s - 2m_1^s)[\bar{u}_t^a - \bar{u}_{t-1}^a] - m_2^s[\bar{u}_t^w - \bar{u}_{t-1}^w] \quad (2\text{-}46)$$

Using the volumetric strain, the average degree of consolidation, U_{avg}, is:

$$U_{avg} = \frac{\varepsilon_t}{\varepsilon_f} \quad (2\text{-}47)$$

where ε_f is the final volumetric strain.

The time step increment, Δt, is determined from the criteria for the FTCS method (Noye and Tan 1989), which is given as:

$$\Delta t = \alpha \frac{(\Delta x)^2 (\Delta y)^2}{8 c_v} \quad (2\text{-}48)$$

where α is a parameter (of 0.4) (Fox and Berles 1997), and consolidation coefficient c_v is determined as:

$$c_v = \max\{W_2, W_3, A_2, A_3\} \quad (2\text{-}49)$$

Figure 2-4 shows the algorithm of the numerical computation. The input data consist of the model geometry, initial void ratio (e_0), initial degree of saturation (S_0), initial permeabilities (k_0^a, k_0^w), curve fitting parameters for water retention, permeability, compressibility and shrinkage, and boundaries and termination criteria. After the computation program reads the initial data, the program locates the level of matric suction (ψ) on the water retention curve and determines the initial pore pressures (u_0^a, u_0^w). After the program applies the boundary conditions, the computation loop starts using the time step increment (Δt). At each time step, the program determines the permeability and compressibility coefficients using soil properties obtained in the previous time step. Then, the program feeds the obtained data to the coupled FTCS solver, updating the pore pressures, as well as the void ratios, matric suction, and the volumetric strain. The program uses the updated data for termination analysis, running a new loop or ending the loop. Finally, the program calculates

the final volumetric strain ε_f and the average degree of consolidation U_{avg}.

2.4 Model verification

The proposed model was verified against the analytical solution proposed by Ho et al. (2015). The analytical solution applies to the plane-strain consolidation of unsaturated soils. Ho's solution considered small strain theory and hence used constant coefficients for compressibility and permeability. The assumption is suboptimal, as water or air permeability cannot change in consolidation. However, Ho's solution considers coupled water−air flow and is recognised as an effective toolbox for verification. In a small strain condition, the permeability as in Eqs. (2-34) and (2-35) and compressibility in Eq. (2-40) use constant values.

The soil layer is given in Figure 2-1(a). The soil layer is compressed under the surcharge load p = 100 kPa. As per Ho et al. (2015), the surcharge load cause an initial pore water pressure u_0^w = 40 kPa and air pressure u_0^a = 20 kPa in the soil layer. Water and air in the soil layer discharge through the upper boundary and drain wells. The lower boundary is relatively impermeable to air and water. The model parameters, as given in Ho et al. (2015) and Wang et al. (2018), are provided in Table 2-2. The permeability coefficients in the vertical and horizontal directions are the same. As in Ho et al. (2015), three air to water permeability ratios k^a / k^w, i.e., 0.1, 1 and 10, are examined.

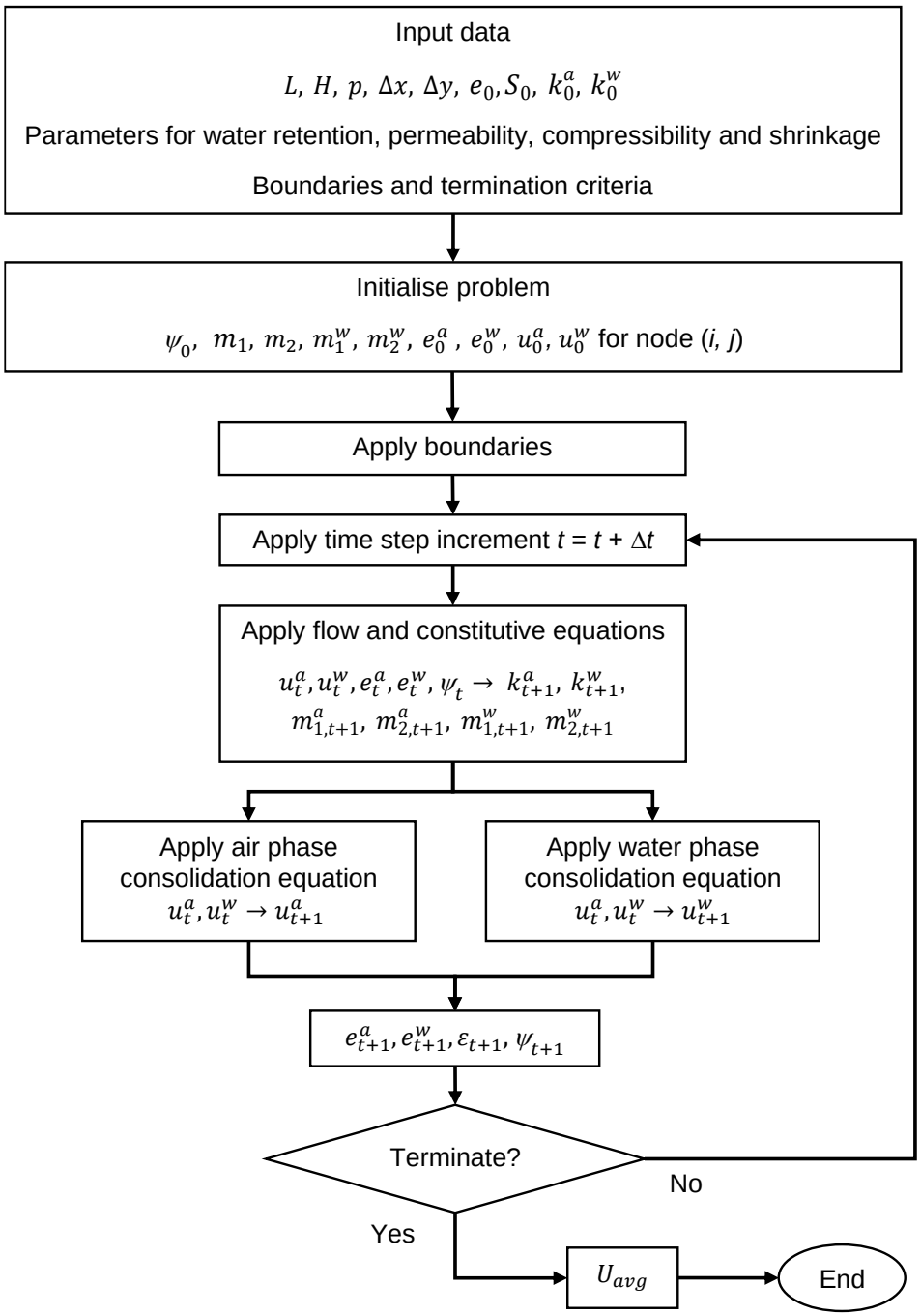

Figure 2-4. Numerical program flow chart.

The mesh sizes, Δx and Δy, are determined through iterations. A series of sizes that progressively decrease are attempted until the obtained degree of consolidation curves approach its asymptote. The sizes attempted were 0.4, 0.2, 0.1, 0.05 and 0.025 m. As per Wang et al. (2018), set $\Delta x = \Delta y$, therefore enabling a square mesh.

Figure 2-5 shows the pore air pressure at the location of x/L = 0.5 and y/H = 0.8 for the case of $k^a = k^w$. In the figure, the elapse times t = 10^5, 10^6, 10^7 seconds correspond to 1.2, 12 and 120 days, respectively. The curves cluster when the mesh sizes are 0.2 m or less. The zoom-in indicates the plots approach its asymptote when the size becomes 0.05 m, and hence a 0.05 m mesh size is used.

The consolidation results obtained from the proposed model and Ho et al. (2015) are given in Figure 2-6. This figure consists of the normalised pore water and pore air pressures, u^a / u_0^a and u^w / u_0^w, and the average degree of consolidation, U_{avg}, versus time t. Excellent agreement between the proposed model and the analytical solution for the consolidation results is obtained. Minor discrepancies in the air pressure dissipation exist. The discrepancies are marginal since the coefficients of consolidation A_2 and A_3 are deformation dependent. That is, with the decrease in the air phase void ratio, the coefficients of consolidation are reduced and thus the pore air pressure dissipation rate decreases. The model is capable to capture the effects of k^a / k^w on the dissipation of air and water pressures. When k^a / k^w increases from 0.1 to 10, the dissipation of the pore air pressure is completed increasingly earlier than the pore water pressure. As a result, the pore water dissipation prevails at the late stage of consolidation. The overall agreement suggests that the proposed model and numerical approach together can model the coupled water−air flow in the soil layer.

Table 2-2. Soil properties used for model verification.

Soil property	Value
Initial soil void ratio, e_0	1
Initial degree of saturation, S_0	80%
Permeability of water, k^w (m/s)	1×10^{-10}
Permeability of air, k^a (m/s)	$0.1\,k_0^w$, k_0^w or $10\,k_0^w$
Coefficient of water volume change per unit change of net normal stress, m_1^w (kPa^{-1})	-5×10^{-5}
Coefficient of water volume change per unit change of matric suction, m_2^w (kPa^{-1})	-2×10^{-4}
Coefficient of air volume change per unit change of net normal stress, m_1^a (kPa^{-1})	-2×10^{-4}
Coefficient of air volume change per unit change of matric suction, m_2^a (kPa^{-1})	1×10^{-4}
Length of soil layer, L (m)	2
Height of soil layer, H (m)	5
Surcharge load, p (kPa)	100
Standard atmosphere, u_{atm}^a (kPa)	101.3
Unit weight of water, γ^w (kN/m^3)	9.81
Acceleration of gravity, g (m/s^2)	9.81
Molecular mass of air, ω (kg/mol)	0.029
Universal gas constant, R (J/mol/K)	8.314
Absolute temperature, θ (K)	293.16

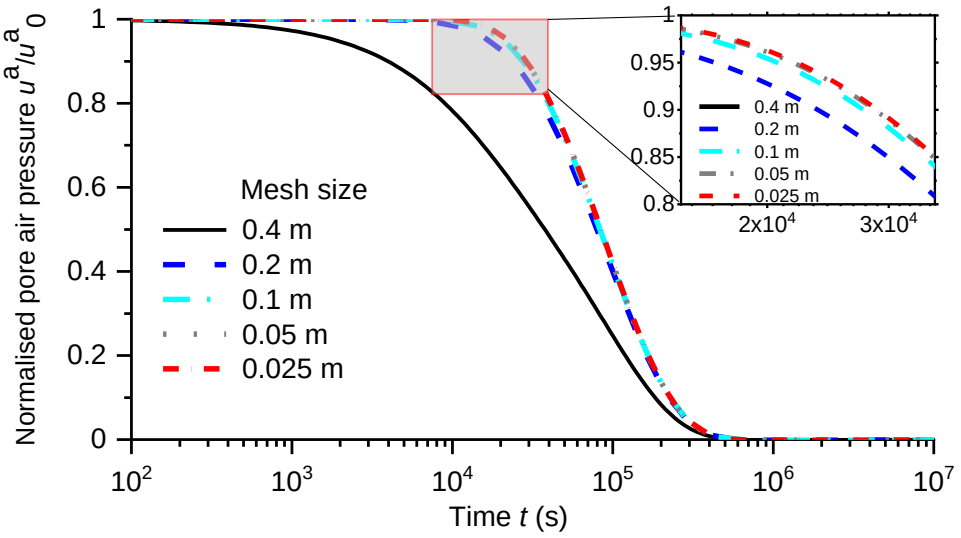

Figure 2-5. Normalized pore air pressure versus time for mesh sizes from 0.025 to 0.4 m.

2.5 Numerical simulations

The verified model was used to conduct numerical simulations to gain an insight into effects of soil properties on consolidation of unsaturated soils. The simulations considered soil hydro-mechanical characteristics and used the water retention curve and constitutive relations given in Fredlund and Xing (1994), Shuai (1996) and Fredlund et al. (2002). The details of the hydro-mechanical characteristics are given in Appendix B. The water retention curve and constitutive relations were sourced from SoilVision Database (The Bentley System Team 2020) with the fitting parameters given in Table 2-3. The other soil properties remain the same as for the verification study. The soil layer is isotropic, i.e., $k^w_{s,x} = k^w_{s,\xi}$ and $k^a_{d,x} = k^a_{d,\xi}$.

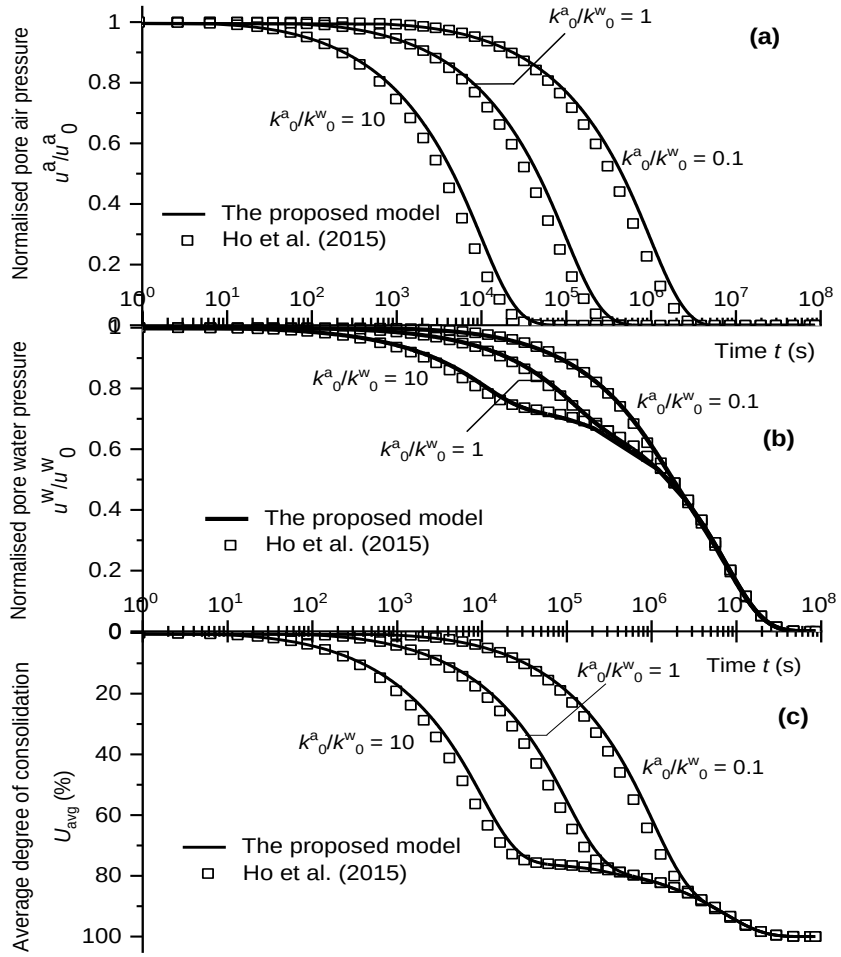

Figure 2-6. Comparison between the proposed model and existing solution with respect to consolidation results: (a) normalized pore air pressures; and (b) normalized pore water pressures, and (c) average degree of consolidation for the soil layer $L \times H$ under surcharge load p.

Five cases, *A* to *E*, were simulated. The cases have different initial degrees of saturation S_0 of from 70% to 90%, therefore examining the effects of volumetric water ratio on consolidation. Each of the cases falls on a location of zero net stress at the water retention curve as given in Table 2-4. Table 2-4 also gives the excess pore pressures

caused by the surcharge load p = 100 kPa which were calculated using the approach in Appendix A.

The simulation results are provided in Figure 2-7. The results consist of the normalised pore pressures and the average degree of consolidation versus time for Cases *A* to *E* and the small strain case. Note the small strain case uses the constant values for permeability and compressibility. It is shown that the small strain method yields relatively fast dissipation of pore air and pore water pressures than the proposed model. Interestingly, the discrepancies are relatively small when S_0 = 70% or 75% and grow when S_0 = 85% or 90%.

Table 2-3. Model parameters for permeability and compressibility of the soil layer.

Parameter	Value
Saturated water content, w_s	0.84
Residual soil suction, h_r (kPa)	714.41
Coefficient of compression, C_c	0.33
Water retention curve parameter, a_f	9.96
Water retention curve parameter, n_f	0.62
Water retention curve parameter, m_f	0.81
Minimum void ratio, a_{sh}	0.44
Slop of the line of tangency, b_{sh}	0.16
Curvature of the shrinkage curve, c_{sh}	3.04
Matric suction adjustment factor, C_{a1}	86.9
Matric suction adjustment factor, C_{a2}	3.45
Matric suction index, C_e	0.28
Parameter for permeability function, λ	0.12
Saturated permeability of water, k_s^w (m/s)	1.25×10^{-8}
Dry permeability of air, k_d^a (m/s)	1.25×10^{-7}

Table 2-4. Initial conditions for Cases A to E

Property	Case A	Case B	Case C	Case D	Case E
S_0 (%)	90	85	80	75	70
e_0	1.4	1.4	1.4	1.4	1.4
u_0^a(kPa)	23.25	14.59	9.87	7.06	5.25
u_0^w(kPa)	29.87	19.80	13.88	10.14	7.63

The values of the initial saturation degree or wet degree affect the consolidation results. The pore air pressure in a less-wet layer dissipates faster than in a wet layer, and vice versa. Similar trend occurs to the pore water pressure dissipation when accompanying the pore air dissipation. The pore air dissipation is completed at approximately 0.1 day when 50% to 65% of pore water pressure has dissipated. The dissipation rates however change among the five cases. The pore water pressure dissipates relatively faster in the less-wet layers when air and water are dissipating and faster in the wet layers at the late consolidation stage when only pore water is left to dissipate. These findings agree with Tang et al. (2018). One reason is air permeability increases with suction as shown in Eq. (2-35), whereas water permeability drops when suction goes up (Eq.(2-34)). Therefore pore air and pore water dissipate differently. Consolidation also progresses differently between pore air and pore water. Although the two phases start to dissipate simultaneously, pore air consolidates noticeably faster than pore water. Similar results were reported in Rahardjo (1990), Conte (2004) and Qin et al. (2010). One may argue air permeates faster than water. This hypothesis however does not stand, as the permeability coefficients of air and water fall on the same magnitude of 10^{-10} m/s when S_0 = 90%, where pore air still dissipates noticeably faster. The dissipation rate can be related to the volume change coefficient with respect to the net stress. For case S_0 = 90%, the volume change coefficient of air with respect to the net stress (10^{-4}

kPa^{-1}) is approximately ten times higher than the coefficient of water (10^{-5} kPa^{-1}). The difference in the volume change coefficients possibly result in the earlier completion of the pore air pressure dissipation.

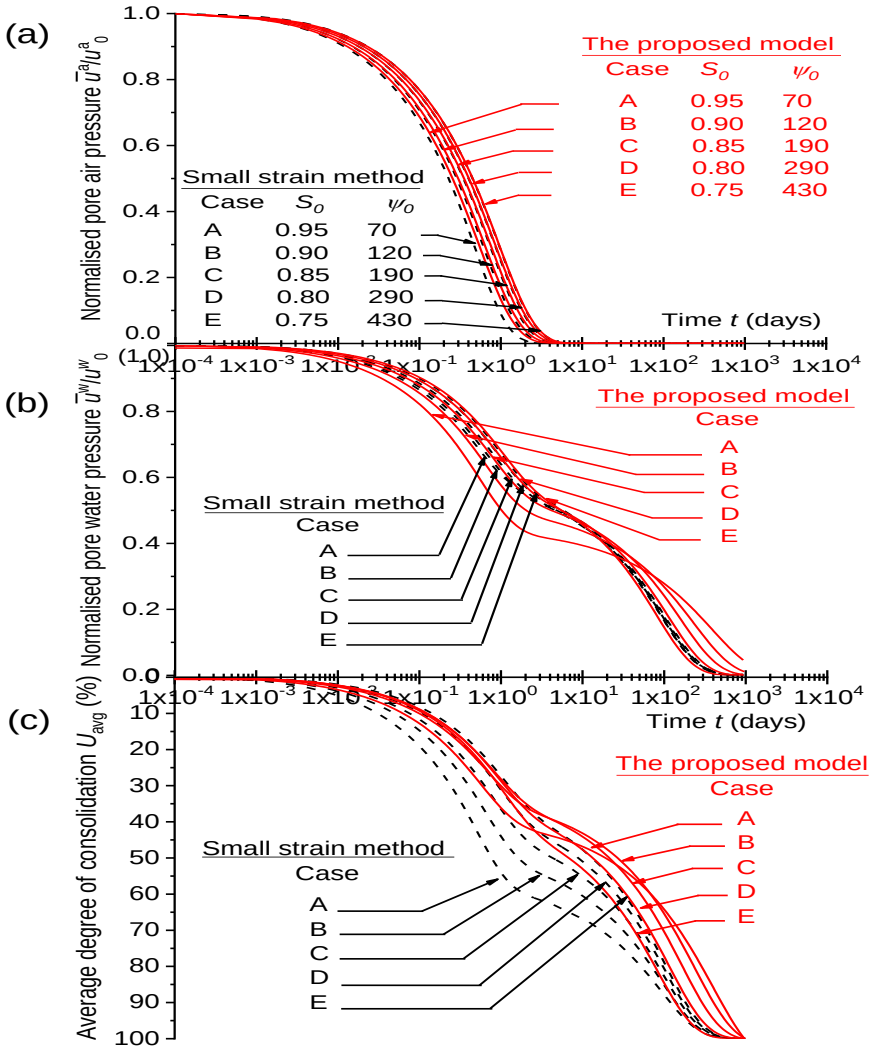

Figure 2-7. Comparison between the proposed model and the small strain method with respect to (a) average normalized pore air pressures; (b) average normalized pore water pressures; and (c) average degree of consolidation obtained for cases A to E of different initial degrees of saturation and matric suction pressures.

The initial wet degree also affects the degree of consolidation. As shown in Figure 2-7(c), the consolidation curves of Cases *A* to *E* are consistent when U_{avg} < 80% (Stage 1). The curves move into Stage 2 of U_{avg} > 80% when the pore air has dissipated completely. The air–water consolidation transits into the solo water consolidation. In this stage, the wet layers attain a higher consolidation degree than the less-wet soils. The wet degree affects the final settlement of soil layer. The wet soil layers deform more than the less-wet soil layers. The final settlements of Cases *A* to *E* range from 107 to 20 mm.

2.6 Model limitation

The proposed model offers to use most soil constitutive relationships and shows favourable agreement with analytical or simulation results. However, the verification against experimental studies has yet been conducted and therefore warrants further studies in vertical drain aided consolidation.

The proposed model used an idealised Dirichlet boundary conditions which is not the case in some instances. Alternatively sophisticated boundary conditions are worth consideration. The model also neglected the environmental effects (i.e., evaporation and infiltration). The effects were reported affecting the consolidation rate (Qi et al. 2017b; a, 2020). A solution is to improve the model to take account of multiple hydro-mechanical processes including drying, wetting, compressing and swelling, thus enabling full-scale modelling.

2.7 Conclusions

The coupled water−air flow equations in unsaturated soils were developed. The equations use a Lagrangian−convective coordinate system to model two-phase flow and soil settlement. The equations integrate water retention capacity, compressibility, shrinkage and permeability constitutive relations. The constitutive relations can be nonlinear and are expressed as explicit functions of stress and suction, enabling large strain consolidation analysis. The proposed equation can determine pore water and pore air pressures at a location in a soil layer at any time, consolidation degree of water and air, and layer settlement at any time.

The coupled equations were solved numerically using the finite difference method. The solutions were verified and the equations were implemented to assess the effects of the initial saturation degree of soil on consolidation. The assessment arrived at the following results:

- Under surcharge preloading, a wet layer takes longer time than a less-wet layer to reach the same consolidation degree at early consolidation stage when pore air and pore water are dissipating; when pore air dissipation is completed and only pore water is left to dissipate, the wet layer consolidate relatively faster. The time effects are more noticeable when using the large strain analysis.
- For the cases examined, the pore air dissipation is completed earlier than the pore water dissipation. The pore air dissipation is completed at approximately 0.1 day when the consolidation degree is about 80%.

- It is necessary to use large strain consolidation analysis for unsaturated soils of relatively high saturation degree and compressibility.

2.8 Notation

The following symbols are used in this paper:

Roman

A_1, A_2, A_3	Coefficients of consolidation for air flow
a_f	Water retention curve fitting parameter
a_{sh}	Minimum void ratio
b_{sh}	Slope of line of tangency
C_{a1}	Matric suction adjustment factor
C_{a2}	Matric suction adjustment factor
C_s	Swelling index
C^{aw}	Compressibility of water−air mixture, kPa^{-1}
C^w	Compressibility of water, kPa^{-1}
c_{sh}	Curvature of shrinkage curve
c_v	Coefficient of consolidation, m^2/s
e	Soil void ratio
e_0	Initial soil void ratio
e^a	Air void ratio
e_0^a	Initial air void ratio
e^w	Water void ratio
e_0^w	Initial water void ratio
g	Gravitational acceleration, m/s^2
H	Height of soil layer, m
h_r	Residual matric suction
i	The i^{th} node in horizontal direction
i_x^w	Hydraulic gradient in horizontal direction, m/m

i_{ξ}^{w}	Hydraulic gradient in vertical direction, m/m
j	The *j*th node in vertical direction
k	Coefficient of permeability
k_{d}^{a}	Permeability of air in dry condition, m/s
k_{x}^{a}	Horizontal permeability of air, m/s
$k_{d,x}^{a}$	Horizontal permeability of air in dry condition, m/s
k_{ξ}^{a}	Vertical permeability of air, m/s
$k_{d,\xi}^{a}$	Initial permeability of air in dry condition, m/s
k_{s}^{w}	Permeability of water in the fully saturated condition, m/s
k_{x}^{w}	Horizontal permeability of water, m/s
$k_{s,x}^{w}$	Horizontal permeability of water in the fully saturated condition, m/s
k_{ξ}^{w}	Vertical permeability of water, m/s
$k_{s,\xi}^{w}$	Vertical permeability of water in the fully saturated condition, m/s
L	Spacing of vertical drains, m
M	Mesh node count in vertical direction
dM^{a}	Air mass per time, kg/s
m_{1}^{a}	Coefficient of air volume change with respect to net stress, kPa^{-1}
m_{2}^{a}	Coefficient of air volume change with respect to matric suction, kPa^{-1}
m^{a}	Air mass flux through the element, $kg/m^2/s$
m_{x}^{a}	Air mass flux in horizontal direction, $kg/m^2/s$
$\dot{m}_{x}^{a}$	Air mass flow rate in horizontal direction, kg/s
m_{ξ}^{a}	Air mass flux in vertical direction, $kg/m^2/s$
$\dot{m}_{\xi}^{a}$	Air mass flow rate in vertical direction, kg/s

m_1	Coefficient of soil volume change with respect to net stress, kPa^{-1}
m_1^w	Coefficient of water volume change with respect to net stress, kPa^{-1}
m_2	Coefficient of soil volume change with respect to matric suction, kPa^{-1}
m_2^w	Coefficient of water volume change with respect to matric suction, kPa^{-1}
m_f	Water retention curve fitting parameter
N	Mesh node count in horizontal direction
n	Porosity
n_f	Water retention curve fitting parameter
p	Surcharge load, kPa
q_x^w	Flow rate of water in horizontal direction, m^2/s per m run
q_ξ^w	Flow rate of water in vertical direction, m^2/s per m run
R	Universal gas constant, J/mol/K
S	Degree of saturation
t	Elapsed time, s
Δt	Time step increment, s
U_{avg}	Average degree of consolidation
u^a	Excess pore air pressure, kPa
u_0^a	Initial excess pore air pressure, kPa
u_{pore}^a	Absolute pore air pressure, kPa
u_{atm}^a	Standard atmosphere, kPa
u^w	Excess pore water pressure, kPa
u_{pore}^w	Pore water pressure, kPa
u_{hydro}^w	Hydrostatic pore water pressure, kPa
$u_t^w(i, j)$	Excess pore water pressure of node (i, j) at time t, kPa

$u_t^a(i, j)$	Excess pore air pressure of node (*i*, *j*) at time *t*, kPa
u_0^w	Initial pore water pressure, kPa
$\overline{u}_t^a$	Average pore air pressure at time *t*, kPa
$\overline{u}_t^w$	Average pore water pressure at time *t*, kPa
V_0	Initial volume of soil, m^3
V^a	Volume of pore air, m^3
V^s	Volume of solids, m^3
V^v	Volume of void, m^3
V^w	Volume of pore water, m^3
v_x^a	Actual velocity of air flow in horizontal direction, m/s
v_ξ^a	Actual velocity of air flow in vertical direction, m/s
$v_x^{a,act}$	Actual velocity of air flow in horizontal direction, m/s
$v_\xi^{a,act}$	Actual velocity of air flow in vertical direction, m/s
$v_\xi^{s,a}$	Velocity of soil particles in vertical direction due to air flow, m/s
v_x^w	Apparent velocity of water flow in horizontal direction, m/s
v_ξ^w	Apparent velocity of water flow in vertical direction, m/s
$v_\xi^{s,w}$	Velocity of soil particles in vertical direction due to water flow, m/s
v_x^w	Actual velocity of water in horizontal direction, m/s
v_ξ^w	Actual velocity of water in vertical direction, m/s
$v_x^{w,act}$	Actual velocity of water in horizontal direction, m/s
$v_\xi^{w,act}$	Actual velocity of water in vertical direction, m/s
W_1, W_2, W_3	Coefficients of consolidation for water flow
w_s	Saturated gravimetric water content
x	Abscissa in Lagrangian coordinate
Δx	Mesh size in horizontal direction, m

y	Ordinate in Lagrangian coordinate
Δy	Mesh size in vertical direction, m
z	Time step number

Greek

Δ	Differential change
α	Parameter for time step increment
ε_t	Volumetric strain of the layer at time t
ε_f	Final volumetric strain of the layer
ξ^a_{t+1}	Elevation of element (x_t, y_t) due to air flow
ξ^w_{t+1}	Elevation of element (x_t, y_t) due to water flow
θ	Temperature in Kelvin scale, K
λ	Parameter for permeability function
ρ^a	Density of air, kg/m^3
ρ	Density of element, kg/m^3
σ_x	Horizontal total stress, kPa
σ_y	Vertical total stress, kPa
γ^w	Unit weight of water, kN/m^3
ψ	Matric suction
ω	Molecular mass of air, kg/mol

Superscripts

a	Pore air
s	Soil soild particles
w	Pore water

Subscripts

t	Time
x	Horizontal direction in Lagrangian coordinate system
y	Veridical direction in Lagrangian coordinate system
ξ	Veridical direction in convective system

$_0$	Initial condition
$_1$	With respect to net stress
$_2$	With respect to matric suction

Coordinates

x	Horizontal axis in Lagrangian coordinate system
y	Veridical axis in Lagrangian coordinate system
ξ	Veridical axis in convective system

Chapter 3 Vertical drain aided consolidation and solute transport

Zhihao Huangfu[1], An Deng[1,*]

[1] School of Architecture and Civil Engineering, The University of Adelaide, Adelaide, SA5005, Australia;

[*] Corresponding Author
E-mail address: an.deng@adelaide.edu.au

Statement of Authorship

Title of Paper	Vertical drain aided consolidation and solute transport
Publication Status	☐ Published ☐ Accepted for Publication ☑ Submitted for Publication ☐ Unpublished and Unsubmitted work written in manuscript style
Publication Details	Huangfu, Z., and Deng, A., 2023. Vertical drain aided consolidation and solute transport. Computers and Geotechnics, under review.

Principal Author

Name of Principal Author (Candidate)	Zhihao Huangfu		
Contribution to the Paper	Conception; Acquiring data; Knowledge; Analysis; Drafting		
Overall percentage (%)	85%		
Certification:	This paper reports on original research I conducted during the period of my Higher Degree by Research candidature and is not subject to any obligations or contractual agreements with a third party that would constrain its inclusion in this thesis. I am the primary author of this paper.		
Signature		Date	05 July 2023

Co-Author Contributions

By signing the Statement of Authorship, each author certifies that:

i. the candidate's stated contribution to the publication is accurate (as detailed above);
ii. permission is granted for the candidate in include the publication in the thesis; and
iii. the sum of all co-author contributions is equal to 100% less the candidate's stated contribution.

Name of Co-Author	An Deng		
Contribution to the Paper	Conception; Knowledge; Analysis; Review		
Signature		Date	6/07/23

Name of Co-Author			
Contribution to the Paper			
Signature		Date	

Please cut and paste additional co-author panels here as required.

Abstract

Land and groundwater pollution is increasingly threatening public health and ecological safety. Vacuum aided vertical drain is recognised as an effective solution to clean up contaminated lands. Clean-ups often involve complicated hydro-chemical transport processes and are difficult to manage. This study presents a consolidation–solute transport model to assist with clean-up management. The model can predict coupled consolidation and chemical transport in diverse ground conditions, e.g., fully or partially saturated, less to highly deformable, or permeable to impermeable layers. To factor in the varied ground conditions, the model integrates the unsaturated flow characteristics, finite deformation theory and finite difference method into a set of governing equations and numerical solutions. The model was experimentally verified and then applied to examine effects of soil saturation conditions, solute transport conditions, and consolidation efforts on solute transport. The results show that the dispersion process contributes to the chemical clean-up, whereas the contribution becomes less noticeable in unsaturated conditions. The solute sorption process counteracts the solute transport and delays the clean-up. The consolidation accelerates the transport of reactive chemicals but shows limited effects on transport of non-reactive chemicals.

Keywords: Unsaturated soil, solute transport, large strain consolidation, finite difference method, Lagrangian−convective.

3.1. Introduction

Illegal dumps from industry operations and municipal activities have caused serious threats to land and groundwater systems. Clean-ups and site management are applied to remediate polluted soil and groundwater. *Pump and treat* is the most common technology for site remediation, but is restricted to relatively permeable ground such as sandy strata. To suit broader ground conditions, vacuum aided vertical drain is recognised as a technique that can effectively transport water and solutes in strata and meanwhile consolidate the strata. Notably, consolidation and solute transport interact each other, mostly in the form of consolidation aided solute transport (Lee and Fox 2009; Peters and Smith 2002; Wu et al. 2020). The interaction of the two processes is complex and therefore remains intriguing.

Analytical and numerical models were developed to depict consolidation induced solute transports. Potter et al. (1994) coupled the advection–dispersion equation with the Terzaghi consolidation theory in a one-dimensional space. Their study was extended to a two dimensional space considering the effects of lateral seepage (Loroy et al. 1996), sorption (Peters and Smith 1998), and boundary conditions (Alshawabkeh et al. 2005). However, these models are suitable for none to small strain deformation conditions where consolidation and transport parameters are assumed constant. However, many studies (such as Fox and Berles 1997; Fox and Lee 2008; Gibson et al. 1981) showed that large strain deformation occurs to thick, compressible strata when consolidated. As a result, the consolidation and transport parameters are changing with the soil porosity and stresses applied. Consolidation results are not accurate if using the small strain

assumption. Advanced modelling that takes account of changing consolidation characteristics is required.

Gibson et al. (1981) developed the finite deformation consolidation model using a Lagrangian–convective deformable coordinate system. The model used void ratio as a variable and considered non-linear changes of compressibility and permeability during consolidation. Smith (2000) used a similarly deformable coordinate system and solved for contaminate transport through porous media. Using the same coordinate system Peters and Smith (2002) examined solute breakthrough and found less time required for solutes to breakthrough in a compressible layer than in a non-compressible layer. These studies were extended to the assessing of two-dimensional transport (Fox 2007a; b), nonlinear sorption (Fox and Lee 2008), and constant rate of strain (Pu and Fox 2015). The finite deformation models were also applied to predict preloading consolidation induced solute transport in layered soil (Pu and Fox 2016; Yu et al. 2018), self-weight consolidation induced solute transport (Pu et al. 2020), electro-osmosis induced solute transport (Deng and Wang 2014), and landfill leaches through geomembrane (Lewis et al. 2009). These studies are only suitable for fully saturated soil layers. In partially saturated layers, presence of air complicates consolidation and solute transport, therefore warranting development of more robust approaches.

Consolidation induced solute transport in an unsaturated layer is solved by using a pore fluid compressibility factor. The factor accounts for pore air compression induced layer deformation and can be integrated to general consolidation equations (Fredlund et al. 2012). Zhang et al. (2012, 2013) and Wu et al. (2020) applied this conception to model consolidation induced solute transport in partially saturated layers. Their models can consider saturation degrees but are

unsatisfactory in capturing coupled water–air pressure dissipation. The coupled dissipation is a non-linear process and is affected by water retention capacity and constitutive relationships e.g., shrinkage curve and compressibility curve (Fredlund and Zhang 2013; Huangfu and Deng 2023; Qi et al. 2017b, 2020; Shuai 1996b; Tang et al. 2018). Due to difficulty to measure pore air pressures, previous models considered the pore fluid only, and did not take account of the coupled dissipation when predicting consolidation induced solute transport. Failing to capture the liquid and gas combined dissipation likely results in errors in predicting seepage velocity and solute transport.

This study presents a model for consolidation induced solute transport. As a further step to the consolidation model in Huangfu and Deng (2023), the current model considers four phases, i.e. pore air, pore water, solids and pore solute, and develops the governing questions for consolidation and solute transport in unsaturated soil layers. The model is solved numerically using unconditionally stable alternative direction implicit finite difference time domain algorithm. The performance of the model was verified against the analytical and experimental studies. Some interesting example problems were solved, showing site clean-up results in relation to soil saturation conditions, solute transport characteristics, and consolidation boundaries.

3.2. Model development

3.2.1 Coordinate system

A layer with vertical drains installed at spacing of L and depth of H is assumed, as shown in Figure 3-1 (a). A Lagrangian-convective coordinate system consists of two coordinates, i.e. spatial coordinate

(*x*, *y*) in Figure 3-1 (b) and temporal coordinate (*x*, ξ) in Figure 3-1 (c and d). The coordinate system enables a real-time update of the element location and element state and hence enables the finite deformation analysis. Vertically, spatial coordinate (*x*, *y*) has height *y* fixed at the datum, capturing the soil layer deformation; temporal coordinate (*x*, ξ) has height ξ fixed in the soil layer, determining the element deformation. Superscripts *w* and *a* represent the water and air phases respectively, and *dy*, $d\xi$ are the element height in spatial and temporal coordinates respectively.

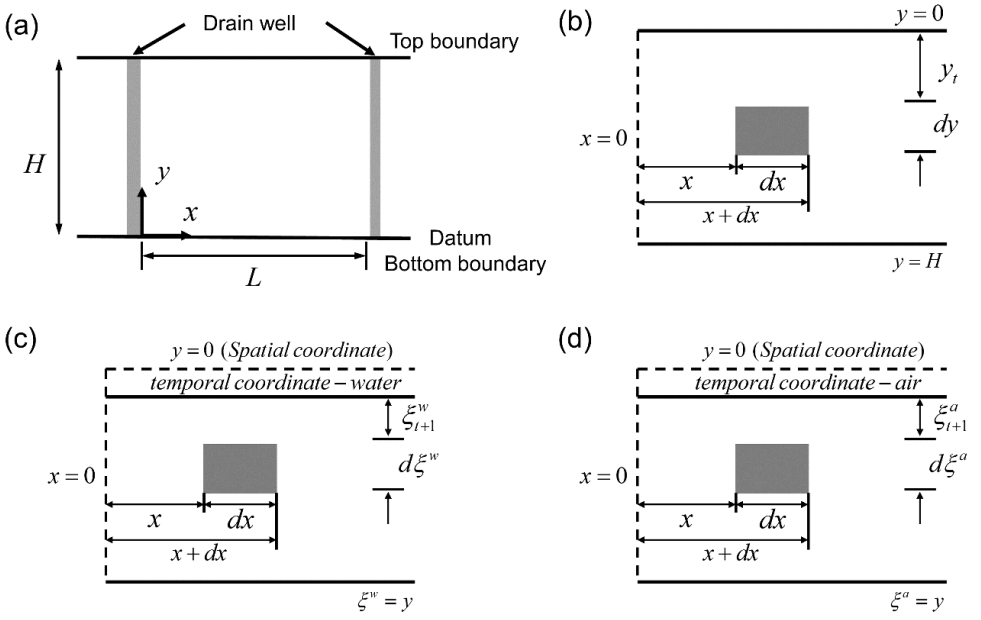

Figure 3-1. Lagrangian–convective coordinate system: (a) datum plane, (b) soil element, (c) water phase, and (d) air phase.

In coordinate (*x*, ξ), and over a time step increment Δt, the thickness of element *dxdy* reduces to $\partial\xi^w$ due to water volume change, $\partial\xi^a$ due to air volume change, or a combination thereof. Correspondingly, the element relocates to ξ^w_{t+1}, ξ^a_{t+1}, or a lower elevation due to the combination effect. The results obtained in coordinate (x, ξ) are used

to calculate element location in coordinate (*x, y*). The calculations follow the relationships as:

$$\begin{cases} \dfrac{\partial \xi^w}{\partial y} = \dfrac{1+e^w}{1+e_0^w} \\ \dfrac{\partial \xi^a}{\partial y} = \dfrac{1+e^a}{1+e_0^a} \end{cases} \quad (3\text{-}1)$$

where, e^w and e^a are water and air void ratios respectively, and subscript $_0$ is the initial condition.

3.2.2 Consolidation equation

Huangfu and Deng (2023) developed a mass conservation equation based on Darcy's and Fick's laws. Their method adopted the following assumptions: 1) Soil particle and water phase are incompressible; 2) Flow of water and air leads to soil deformation separately and the deformation is superimposable; 3) Environmental effect such as evaporation, temperature and air dissolving in water are neglected; 4) Smear effect and well resistance are neglected; and 5) Deformation occurs in vertical direction only, the radial deformation is neglected. The equation governs the volume change of water and air in term of the pore stresses is adopted from Huangfu and Deng (2023) and is expressed as:

$$\begin{cases} \dfrac{\partial e^w}{\partial t} = \dfrac{k_x^w\left(1+e^w\right)}{\gamma^w}\dfrac{\partial}{\partial x}\left(\dfrac{\partial u'^w}{\partial x}\right) + \dfrac{k_\xi^w\left(1+e_0^w\right)^2}{\gamma^w\left(1+e^w\right)}\dfrac{\partial}{\partial y}\left(\dfrac{\partial u'^w}{\partial y}\right) \\ \dfrac{\partial e^a}{\partial t} = -\dfrac{e^a(1+e^w)}{\left(1+e\right)\left(u'^a+u_{atm}^a\right)}\dfrac{\partial u'^a}{\partial t} + \dfrac{k_x^a\left(1+e^a\right)R\theta_k}{\omega g\left(u'^a+u_{atm}^a\right)}\dfrac{\partial}{\partial x}\left(\dfrac{\partial u'^a}{\partial x}\right) \\ \qquad + \dfrac{k_\xi^a\left(1+e_0^a\right)^2 R\theta}{\omega g\left(1+e^a\right)\left(u'^a+u_{atm}^a\right)}\dfrac{\partial}{\partial y}\left(\dfrac{\partial u'^a}{\partial y}\right) \end{cases} \quad (3\text{-}2)$$

where, k_x and k_ξ are permeabilities in horizontal and vertical directions respectively, γ^w is the specific gravity of water, u' is the excess pore pressure, ω, R, θ_k, and u_{atm}^a are the molecular mass of air, universal constant, temperature in Kelvin, and the standard atmosphere pressure respectively. As per Dakshanamurthy and Fredlund (1980), the volume changes of water and air are related to the soil compressibility as:

$$\begin{cases} \dfrac{\partial e^w}{\partial t} = \left(1+e_0\right)\left[m_1^w\dfrac{\partial}{\partial t}\left(\sigma_x-u^a\right) + m_1^w\dfrac{\partial}{\partial t}\left(\sigma_y-u^a\right) + m_2^w\dfrac{\partial}{\partial t}\left(u^a-u^w\right)\right] \\ \dfrac{\partial e^a}{\partial t} = \left(1+e_0\right)\left[m_1^a\dfrac{\partial}{\partial t}\left(\sigma_x-u^a\right) + m_1^a\dfrac{\partial}{\partial t}\left(\sigma_y-u^a\right) + m_2^a\dfrac{\partial}{\partial t}\left(u^a-u^w\right)\right] \end{cases} \quad (3\text{-}3)$$

where u^a and u^w are the pore water and pore air pressures respectively, m_1 and m_2 are the soil volume change coefficients with respect to net stress, and matric suction respectively, and are determined from soil retention, compressibility and shrinkage curves respectively.

Combining Eq. (3-2) and (3-3), the dissipation of excess pore pressures are written as:

$$\begin{cases} \dfrac{\partial u'^{w}}{\partial t} = \dfrac{\left(m_2^w - 2m_1^w\right)}{m_2^w}\dfrac{\partial u'^{a}}{\partial t} - \dfrac{k_x^w\left(1+e^w\right)\left(1+2m_1^w\rho g\triangle y\right)}{\gamma^w m_2^w\left(1+e_0\right)}\dfrac{\partial^2 u'^{w}}{\partial x^2} \\ \qquad - \dfrac{k_\xi^w\left(1+e^{w0}\right)^2\left(1+2m_1^w\rho g\triangle y\right)}{\gamma^w m_2^w\left(1+e^w\right)\left(1+e_0\right)}\dfrac{\partial^2 u'^{w}}{\partial y^2} \\ \dfrac{\partial u'^{a}}{\partial t} = \dfrac{m_2^a\left(1+e_0\right)\left(1+e\right)\left(u'^{a}+u_{atm}^a\right)}{\left(1+e_0\right)\left(1+e\right)\left(m_2^a-2m_1^a\right)\left(u'^{a}+u_{atm}^a\right)+e^a\left(1+e^w\right)\left(1+2m_1^a\rho g\triangle y\right)}\dfrac{\partial u'^{w}}{\partial t} \\ \qquad + \dfrac{k_x^a R\theta\left(1+e^a\right)\left(1+e\right)\left(1+2m_1^a\rho g\triangle y\right)}{\omega g\left[\left(1+e_0\right)\left(1+e\right)\left(m_2^a-2m_1^a\right)\left(u'^{a}+u_{atm}^a\right)+e^a\left(1+e^w\right)\left(1+2m_1^a\rho g\triangle y\right)\right]}\dfrac{\partial^2 u'^{a}}{\partial x^2} \\ \qquad + \dfrac{k_\xi^a R\theta\left(1+e\right)\left(1+e_0^a\right)^2\left(1+2m_1^a\rho g\triangle y\right)}{\omega g\left(1+e^a\right)\left[\left(1+e_0\right)\left(1+e\right)\left(m_2^a-2m_1^a\right)\left(u'^{a}+u_{atm}^a\right)+e^a\left(1+e^w\right)\left(1+2m_1^a\rho g\triangle y\right)\right]}\dfrac{\partial^2 u'^{a}}{\partial y^2} \end{cases} \tag{3-4}$$

or in a matrix form as:

$$\alpha_1 u'_t = \alpha_2 u'_{xx} + \alpha_3 u'_{yy} \tag{3-5}$$

where,

$$\alpha_1 = \begin{pmatrix} 1 & -W_1 \\ -A_1 & 1 \end{pmatrix} \quad \alpha_2 = \begin{pmatrix} W_2 & 0 \\ 0 & A_2 \end{pmatrix} \quad \alpha_3 = \begin{pmatrix} W_3 & 0 \\ 0 & A_3 \end{pmatrix}$$

$$u'_t = \begin{pmatrix} \dfrac{\partial u'^{w}}{\partial t} \\ \dfrac{\partial u'^{a}}{\partial t} \end{pmatrix} \quad u'_{xx} = \begin{pmatrix} \dfrac{\partial^2 u'^{w}}{\partial x^2} \\ \dfrac{\partial^2 u'^{a}}{\partial x^2} \end{pmatrix} \quad u'_{yy} = \begin{pmatrix} \dfrac{\partial^2 u'^{w}}{\partial y^2} \\ \dfrac{\partial^2 u'^{a}}{\partial y^2} \end{pmatrix}$$

$$A_1 = \frac{m_2^a\left(1+e_0\right)\left(1+e\right)\left(u'^{a}+u_{atm}^a\right)}{\left(1+e_0\right)\left(1+e\right)\left(m_2^a-2m_1^a\right)\left(u'^{a}+u_{atm}^a\right)+e^a\left(1+e^w\right)\left(1+2m_1^a\rho g\triangle y\right)}$$

$$A_2 = \frac{k_x^a R\theta_k\left(1+e^a\right)\left(1+e\right)\left(1+2m_1^a\rho g\triangle y\right)}{\omega g\left[\left(1+e_0\right)\left(1+e\right)\left(m_2^a-2m_1^a\right)\left(u'^{a}+u_{atm}^a\right)+e^a\left(1+e^w\right)\left(1+2m_1^a\rho g\triangle y\right)\right]} \tag{3-6}$$

$$A_3 = \frac{k_\xi^a R\theta_k\left(1+e\right)\left(1+e_0^a\right)^2\left(1+2m_1^a\rho g\triangle y\right)}{\omega g\left(1+e^a\right)\left[\left(1+e_0\right)\left(1+e\right)\left(m_2^a-2m_1^a\right)\left(u'^{a}+u_{atm}^a\right)+e^a\left(1+e^w\right)\left(1+2m_1^a\rho g\triangle y\right)\right]}$$

$$W_1 = \frac{\left(m_2^w - 2m_1^w\right)}{m_2^w}$$

$$W_2 = -\frac{k_x^w\left(1+e^w\right)\left(1+2m_1^w\rho g\triangle y\right)}{\gamma^w m_2^w\left(1+e_0\right)}$$

$$W_3 = -\frac{k_\xi^w\left(1+e_0^w\right)^2\left(1+2m_1^w\rho g\triangle y\right)}{\gamma^w m_2^w\left(1+e^w\right)\left(1+e_0\right)}$$

It is noteworthy that the volume change coefficients of solid, m_1^s, m_2^s, and volume change coefficients of water, m_1^w, m_2^w, become the coefficient of volume change, m_V, when the soil layer is fully saturated (Fredlund et al. 2012). Meanwhile the volume change coefficients of air, m_1^a, m_2^a, become zero. Therefore Eq. (3-4) is simplified into the two-dimensional large strain consolidation equation of fully saturated soil. The processes are given in Appendix C. The simplified consolidation equation is written as:

$$\frac{\partial u'^w}{\partial t} = -\frac{k_\xi^w\left(1+e^{w0}\right)\left(1+m_v\Delta y\left(\rho^s-\rho^w\right)g\right)}{\gamma^w m_v\left(1+e^w\right)}\frac{\partial^2 u'^w}{\partial y^2} - \frac{k_x^w\left(1+e^w\right)\left(1+m_v\Delta y\left(\rho^s-\rho^w\right)g\right)}{\gamma^w m_v\left(1+e^{w0}\right)}\frac{\partial^2 u'^w}{\partial x^2} \quad (3\text{-}7)$$

3.2.3 Solute transport equation

For consolidation induced solute transport, the fluid is less likely to be vaporised due to the relatively low seepage rate, and hence the solute infiltration into the air phase can be neglected (Wu 2019). Assuming the solute is carried out by water phase only, solutes in porous media generally transport in four processes, i.e. advection, diffusion, dispersion and adsorption (Fox 2007b; Zhang et al. 2013). These processes obey the mass conservation law. Applying the law to soil solids, Zhang et al. (2013) suggested the following relationship:

$$\frac{\partial}{\partial t}\left[\left(1-n\right)\rho^s S\frac{\partial \xi}{\partial y}\right] = f'_{a\to s} \quad (3\text{-}8)$$

where ρ^s is the density of solids, n is the porosity, $f'_{a\to s}$ is the solid adsorption induced solute loss in pore water, and S is the mass ratio of solute adsorbed to solids, also known as Freundlich adsorption isotherm. The isotherm is determined as $S = K^d c_f$ (Peters and Smith 2002), where K^d is the partitioning of the contaminant and determined

experimentally, and c_f is the pore solute concentration. For pore fluid, Zhang et al. (2013) proposed the mass conservation relationship as:

$$\frac{\partial}{\partial t}\left[nS_r c_f \frac{\partial \xi}{\partial y} \right] = -\nabla J_f - f'_{a\to s} \tag{3-9}$$

where S_r is the degree of saturation, and J_f is the fluid flux in Cartesian coordinate. The divergence of J_f, ∇J_f, in two-dimensional space has following form:

$$\nabla J_f = \frac{\partial}{\partial y}\left[nS_r c_f \left(v_\xi^w - v^s \right) \right] + \frac{\partial}{\partial x}\left[nS_r c_f v_x^w \right] - \frac{\partial}{\partial y}\left[\frac{nS^r D_\xi}{M} \frac{\partial c_f}{\partial y} \right] - \frac{\partial}{\partial x}\left[nS_r D_x \frac{\partial c_f}{\partial x} \right] \tag{3-10}$$

where, v_ξ^w, v_x^w are the water flow velocity in vertical and horizontal directions respectively, v^s is the solids settling speed, M is the ratio between temporal and spatial coordinate, i.e. $M = \partial\xi / \partial y$, and D is the hydrodynamic dispersion coefficient. Note $\left(v_\xi^w - v^s \right)$ in Eq. (3-10) represents the true velocity of water in the vertical direction. In terms of Darcy's law, the water flow velocities in relation to the coordinates have the following relationships:

$$\begin{cases} \left(v_\xi^w - v_\xi^s \right) = -\dfrac{1+e^w}{e^w} \dfrac{k_\xi^w}{\gamma^w} \dfrac{\partial u'^w}{\partial \xi} \\ v_x^w = -\dfrac{1+e^w}{e^w} \dfrac{k_x^w}{\gamma^w} \dfrac{\partial u'^w}{\partial x} \end{cases} \tag{3-11}$$

Combining Eqs. (3-8) to (3-11) leads to the solute transport equation as:

$$\begin{aligned} \left(M \frac{\rho^s K^d + e^w}{1+e} \right) \frac{\partial c_f}{\partial t} = & \left(\frac{e^w D_\xi}{(1+e)M} \right) \frac{\partial^2 c_f}{\partial y^2} + \left(\frac{e^w D_x}{1+e} \right) \frac{\partial^2 c_f}{\partial x^2} \\ & + \left(\frac{1+e_0^w}{1+e} \frac{k_\xi^w}{\gamma^w} \right) \frac{\partial c_f}{\partial y} \frac{\partial u'^w}{\partial y} + \left(\frac{1+e^w}{1+e} \frac{k_x^w}{\gamma^w} \right) \frac{\partial c_f}{\partial x} \frac{\partial u'^w}{\partial x} \end{aligned} \tag{3-12}$$

The hydrodynamic dispersion coefficient D takes account of mechanical dispersion and effective diffusion (Peters and Smith 2002). For unsaturated soil, Li and Liu (2006) and Zhang et al. (2013)

suggested to determine the coefficients in vertical and horizontal directions respectively as:

$$D_\xi = \alpha_\xi^l \left(v_\xi^w - v^{s,w}\right) + \beta_\xi$$
$$D_x = \alpha_x^t v_x^w + \beta_x \quad (3\text{-}13)$$

where α_ξ^l and α_x^t are the longitudinal and transverse dispersion, and β_ξ and β_ξ are the longitudinal and transverse mechanical dispersion respectively. In unsaturated soil, the mechanical dispersion coefficients are written as:

$$\beta_\xi = 1.1 D_\xi^f \frac{e^w}{1+e}\left(\frac{e^w}{1+e} - \theta_T\right)$$
$$\beta_x = 1.1 D_x^f \frac{e^w}{1+e}\left(\frac{e^w}{1+e} - \theta_T\right) \quad (3\text{-}14)$$

where θ_t is the residual water content, and D_ξ^f and D_x^f are the free diffusion coefficients in vertical and horizontal directions, and are written as

$$D_\xi^f = D_{\xi,0}^f \left(\frac{e}{1+e}\right)^{M_d}$$
$$D_x^f = D_{x,0}^f \left(\frac{e}{1+e}\right)^{M_d} \quad (3\text{-}15)$$

where $D_{\xi,0}^f$ and $D_{x,0}^f$ are the free diffusion coefficients in vertical and horizontal directions, and M_d is the diffusion constant. Note the β_ξ and β_x are equal to D_ξ^f and D_x^f in fully saturated conditions.

Substituting Eq. (3-13) into Eq. (3-12), the solution equation is written as:

$$\frac{\partial c_f}{\partial t} = C_1 \frac{\partial^2 c_f}{\partial x^2} + C_2 \frac{\partial^2 c_f}{\partial y^2} + C_3 \frac{\partial c_f}{\partial x} + C_4 \frac{\partial c_f}{\partial y} \quad (3\text{-}16)$$

where,

$$C_1 = \frac{\left[e^w \beta_x - \left(\frac{\alpha_x^t k_x^w \left(1+e^w\right)}{\gamma^w} \frac{\partial u'^w}{\partial x} \right) \right]}{M\left(\rho^s K^d + e^w\right)}$$

$$C_2 = \frac{\left[e^w \beta_\xi - \left(\frac{\alpha_\xi^l k_\xi^w \left(1+e_0^w\right)}{\gamma^w} \frac{\partial u'^w}{\partial y} \right) \right]}{M^2\left(\rho^s K^d + e^w\right)} \qquad (3\text{-}17)$$

$$C_3 = \frac{k_\xi^w \left(1+e_0^w\right)}{M\gamma^w\left(\rho^s K^d + e^w\right)} \frac{\partial u'^w}{\partial y}$$

$$C_4 = \frac{k_x^w \left(1+e^w\right)}{M\gamma^w\left(\rho^s K^d + e^w\right)} \frac{\partial u'^w}{\partial x}$$

where the excess pore water pressure differences are solved using the centre difference method as follows:

$$\frac{\partial u'^w}{\partial x} = \frac{u'^w{}_{i+1,j} - u'^w{}_{i-1,j}}{2\Delta x}$$
$$\frac{\partial u'^w}{\partial y} = \frac{u'^w{}_{i+1,j} - u'^w{}_{i,j-1}}{2\Delta y} \qquad (3\text{-}18)$$

Eq. (3-16) governs the solute concentration at locations (x, y). The solute equation is coupled with the consolidation equation (Eq. (3-5)). The parameters in the consolidation equation including e, e^w, k_ξ^w, k_x^w and u'^w are solved and fed in the counterparts in the solute transport equation. The remaining parameters such as D^f, α_ξ^l and α_x^t are determined experimentally.

3.3. Numerical simulations

The consolidation and solution equations can be solved numerically using the finite difference method. The $L \times H$ soil layer (in Figure 2) is discretised into a $Q \times N$ mesh, with each element of $\Delta x \times \Delta y$, as shown in Figure 2. The soil properties of an element is represented by node (i,

j), where $i = 1, 2, \ldots, Q$, and $j = 1, 2, \ldots, N$. The mesh extends in time domain until $z\Delta t$, where the time step number $z = 0, 1, 2, 3, \infty$ (or a number large enough for numerical termination).

Differential equations are often solved using the explicit finite difference approach. The approach is suitable to solve most uncoupled governing equations, but as per Purnaditya et al. (2019) suffers computation instability when solving coupled governing equations such as Eqs. (3-5) and (3-16). Applying the implicit finite difference method to a two-dimensional problem less likely gives results in first-order accuracy in time (Hoffman and Frankel 2018). Alternative direction implicit finite difference time domain (ADI-FDTD) method outperforms the explicit and implicit finite difference by achieving unconditional stability (Douglas and Rachford 1956) and second order accuracy in time and space. This approach was applied successfully to solve coupled consolidation equations such as Hu et al. (2014) and solute transport equations (Purnaditya et al. 2019). ADI-FDTD approach breaks one time step into two and discretises the governing equation into a tridiagonal matrix form (Chen et al. 2021; Thomas 1949). Figure 3-2 shows the splitting of the time step increment Δt. Time step t to ($t + \Delta t$) consists of two sub-steps, i.e. t to ($t + 0.5\Delta t$) and ($t + 0.5\Delta t$) to ($t + \Delta t$). In the first sub-step, discretise the soil layer domain implicitly in *x*-axis and explicitly in *y*-axis; then in the second sub-step, swap the axes, discretising the domain explicitly in *x*-axis and implicitly in *y*-axis. The combination of two sub-steps eliminates explicit discretisation, therefore achieving unconditionally stable computation.

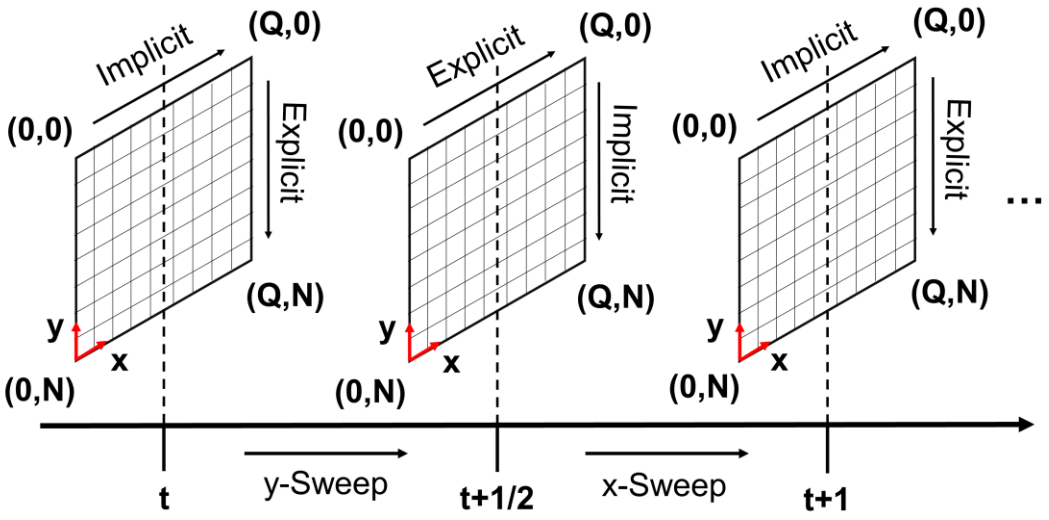

Figure 3-2. Explicit–implicit finite difference schematic diagram.

3.3.1. Consolidation equation solution

The discretisation of the consolidation equation uses Taylor series expansion. In the first time sub-step, the consolidation equation (Eq. (3-5)) is written as:

$$\alpha_1\left(\frac{u_{i,j}^{t+1/2}-u_{i,j}^{t}}{\Delta t/2}\right)=\alpha_2\left(\frac{u_{i+1,j}^{t}-2u_{i,j}^{t}+u_{i-1,j}^{t}}{2\Delta x^2}\right)+\alpha_3\left(\frac{u_{i,j+1}^{t+1/2}-2u_{i,j}^{t+1/2}+u_{i,j-1}^{t+1/2}}{2\Delta y^2}\right) \quad (3\text{-}19)$$

Eq. (3-19) can be simplified as

$$-\frac{\alpha_3\Delta t}{4\alpha_1\Delta y^2}u_{i,j+1}^{t+1/2}+\left(1+\frac{\alpha_3\Delta t}{2\alpha_1\Delta y^2}\right)u_{i,j}^{t+1/2}-\frac{\alpha_3\Delta t}{4\alpha_1\Delta y^2}u_{i,j-1}^{t+1/2}=b_{i,j}^{t} \quad (3\text{-}20)$$

where

$$b_{i,j}^{t}=\frac{\alpha_2\Delta t}{4\alpha_1\Delta x^2}u_{i+1,j}^{t}+\left(1-\frac{\alpha_2\Delta t}{2\alpha_1\Delta x^2}\right)u_{i,j}^{t}+\frac{\alpha_2\Delta t}{4\alpha_1\Delta x^2}u_{i-1,j}^{t} \quad (3\text{-}21)$$

Let $\beta_1=\frac{\alpha_3\Delta t}{4\alpha_1\Delta y^2}$, $\beta_2=\left(1+\frac{\alpha_3\Delta t}{2\alpha_1\Delta y^2}\right)$ and P_0 = excess pore pressure at the open boundaries. Considering the boundary conditions in Figure 1,

i.e. $u'^{t}_{i,1} = P_0$, $u'^{t}_{1,j} = P_0$, $u'^{t}_{Q,j} = P_0$, and $\frac{\partial u'^{t}_{i,N}}{\partial t} = 0$, Eq. (3-20) is written into a matrix form as:

$$\begin{pmatrix} I & 0 & & & \\ -\beta_{1i,2} & \beta_{2i,2} & -\beta_{1i,2} & & \\ & & \cdots & & \\ & & -\beta_{1i,N-1} & \beta_{2i,N-1} & -\beta_{1i,N-1} \\ & & & -2\beta_{1i,N} & \beta_{2i,N} \end{pmatrix} \begin{pmatrix} u'^{t+1/2}_{i,1} \\ u'^{t+1/2}_{i,2} \\ \vdots \\ u'^{t+1/2}_{i,N-1} \\ u'^{t+1/2}_{i,N} \end{pmatrix} = \begin{pmatrix} P_0 \\ b^{t}_{i,2} \\ \vdots \\ b^{t}_{i,N-1} \\ b^{t}_{i,N} \end{pmatrix} \tag{3-22}$$

where *I* is the 2D identity matrix, and as per Chen et al. (2021) the lower diagonal at the boundary layer is $-2\beta_{1i,N}$. Eq. (3-22) is solved using the Tridiagonal Matrix Algorithm (TDMA) (Chen et al. 2021; Thomas 1949). Specifically, the resulting excess pore pressures at the bottom boundary ($u'^{t+1/2}_{i,N}$) are replaced with $u'^{t+1/2}_{i,N-1}$, denoting the impervious base. Iterate through the domain mesh by columns from *i* = 1 to (*Q*–1) to solve for the pore pressures $u'^{t+1/2}_{i,j}$. Use the pore pressures as the initial conditions for the calculations in the second time sub-step. The consolidation equation in the second sub-step is then written as:

$$-\frac{\alpha_2 \Delta t}{4\alpha_1 \Delta x^2} u'^{t+1}_{i+1,j} + \left(1 + \frac{\alpha_2 \Delta t}{2\alpha_1 \Delta x^2}\right) u'^{t+1}_{i,j} - \frac{\alpha_2 \Delta t}{4\alpha_1 \Delta x^2} u'^{t+1}_{i-1,j} = b^{t+1/2}_{i,j} \tag{3-23}$$

where

$$b^{t+1/2}_{i,j} = \frac{\alpha_3 \Delta t}{4\alpha_1 \Delta y^2} u'^{t+1/2}_{i,j+1} + \left(1 - \frac{\alpha_3 \Delta t}{2\alpha_1 \Delta y^2}\right) u'^{t+1/2}_{i,j} + \frac{\alpha_3 \Delta t}{4\alpha_1 \Delta y^2} u'^{t+1/2}_{i,j-1} \tag{3-24}$$

Similarly, let $\beta_3 = \frac{\alpha_2 \Delta t}{4\alpha_1 \Delta x^2}$ and $\beta_4 = \left(1 + \frac{\alpha_2 \Delta t}{2\alpha_1 \Delta x^2}\right)$. Applying the boundary conditions, Eq. (3-20) for the domain mesh by rows is:

$$\begin{pmatrix} I & 0 & & & \\ -\beta_{3\,2,j} & \beta_{4\,2,j} & -\beta_{3\,2,j} & & \\ & & \cdots & & \\ & & -\beta_{3\,Q-1,j} & \beta_{4\,Q-1,j} & -\beta_{3\,Q-1,j} \\ & & & 0 & I \end{pmatrix} \begin{pmatrix} u'^{t+1}_{1,j} \\ u'^{t+1}_{2,j} \\ \vdots \\ u'^{t+1}_{Q-1,j} \\ u'^{t+1}_{Q,j} \end{pmatrix} = \begin{pmatrix} P_0 \\ b^{t+1/2}_{2,j} \\ \vdots \\ b^{t+1/2}_{Q-1,j} \\ P_0 \end{pmatrix} \tag{3-25}$$

Eq. (3-25) is solved using the algorithm as for solving Eq. (3-22). The combination of Eqs. (3-22) and (3-25) is applied to the mesh towards the desired length of time e.g., the computation termination. Note that the time-dependent consolidation parameters, i.e. void ratio and permeability, are obtained from the respective constitutive relations. Alternatively, extract the parameters from the respective constitutive surfaces that are determined experimentally.

3.3.2. Solute transport equation

The solute transport equation (Eq. (3-16)) is solved similar in process to solving the consolidation equation. Defining the solute concentration at the appropriate boundaries as c_0, the matrix for calculations in the first sub-step, t to (t + 0.5Δt), is:

$$\begin{bmatrix} 1 & 0 & & & \\ \chi^{l}_{1i,2} & \chi^{m}_{1i,2} & \chi^{u}_{1i,2} & & \\ & & \cdots & & \\ & & \chi^{l}_{1i,N-1} & \chi^{m}_{1i,N-1} & \chi^{u}_{1i,N-1} \\ & & 0 & 2\chi^{m}_{1i,N} & \chi^{u}_{1i,N} \end{bmatrix} \begin{Bmatrix} cf^{t+1/2}_{i,1} \\ cf^{t+1/2}_{i,2} \\ \vdots \\ cf^{t+1/2}_{i,N-1} \\ cf^{t+1/2}_{i,N} \end{Bmatrix} = \begin{Bmatrix} c_0 \\ c^{t}_{i,2} \\ \vdots \\ c^{t}_{i,N-1} \\ c^{t}_{i,N} \end{Bmatrix} \tag{3-26}$$

and in the 2nd sub-step as:

$$\begin{bmatrix} 1 & 0 & & & \\ \chi^{l}_{22,j} & \chi^{m}_{22,j} & \chi^{u}_{22,j} & & \\ & & \cdots & & \\ & & \chi^{l}_{2Q-1,j} & \chi^{m}_{2Q-1,j} & \chi^{u}_{2Q-1,j} \\ & & & 0 & 1 \end{bmatrix} \begin{Bmatrix} cf^{t+1}_{1,j} \\ cf^{t+1}_{2,j} \\ \vdots \\ cf^{t+1}_{Q-1,j} \\ cf^{t+1}_{Q,j} \end{Bmatrix} = \begin{Bmatrix} c_0 \\ c^{t+1/2}_{2,j} \\ \vdots \\ c^{t+1/2}_{Q-1,j} \\ c_0 \end{Bmatrix} \tag{3-27}$$

where

$$\begin{aligned} \chi^{l}_{1} &= -\left[\frac{C_2\Delta t}{2\Delta y^2} + \frac{C_4\Delta t}{4\Delta y}\right],\ \chi^{m}_{1} = \left[1 + \frac{C_2\Delta t}{\Delta y^2}\right],\ \chi^{u}_{1} = -\left[\frac{C_2\Delta t}{2\Delta y^2} - \frac{C_4\Delta t}{4\Delta y}\right] \\ c^{t} &= \left[\frac{C_1\Delta t}{2\Delta x^2} + \frac{C_3\Delta t}{4\Delta x}\right] cf^{t}_{i+1,j} + \left[1 - \frac{C_1\Delta t}{\Delta x^2}\right] cf^{t}_{i,j} + \left[\frac{C_1\Delta t}{2\Delta x^2} - \frac{C_3\Delta t}{4\Delta x}\right] cf^{t}_{i-1,j} \\ \chi^{l}_{2} &= -\left[\frac{C_1\Delta t}{2\Delta x^2} - \frac{C_3\Delta t}{4\Delta x}\right],\ \chi^{m}_{2} = \left[1 + \frac{C_1\Delta t}{\Delta x^2}\right],\ \chi^{u}_{2} = -\left[\frac{C_1\Delta t}{2\Delta x^2} + \frac{C_3\Delta t}{4\Delta x}\right] \\ c^{t+1/2}_{i,j} &= \left[\frac{C_2\Delta t}{2\Delta y^2} - \frac{C_4\Delta t}{4\Delta y}\right] cf^{t+1/2}_{i,j-1} + \left[1 - \frac{C_2\Delta t}{\Delta y^2}\right] cf^{t+1/2}_{i,j} + \left[\frac{C_2\Delta t}{2\Delta y^2} + \frac{C_4\Delta t}{4\Delta y}\right] cf^{t+1/2}_{i,j+1} \end{aligned} \tag{3-28}$$

To enhance the computation efficiency, χ matrix in Eqs. (3-26) and (3-27) are written in a sparse matrix form in *MATLAB* and solved using matrix operation.

3.4. Model verification

The proposed model was verified against two results. The solute transport model was verified against the analytical results proposed by Bear (1972). The consolidation–solute coupling model was then verified against the experimental results in Lee and Fox (2009). The analytical and experimental verifications collectively can prove the validity of the proposed model.

3.4.1. Solute transport in rigid porous media

Bear (1972) presented a point-source pollution example. The solute originates from the point source pollution and, under uniform steady flow conditions, transports in a fully saturated layer. The transport involves advection and dispersion processes. The layer, 0.5 (*W*) × 1 (*H*) m, is assumed non-deformable and open at the boundaries. Bear (1972) determined the solute concentration as:

$$cf_{i,j}^{t} = \frac{M_s}{4\pi nt\sqrt{D_\zeta D_x}} \exp\left(-\frac{\left(x - x_0 - v_x^w t\right)^2}{4D_x t} - \frac{\left(y_0 - y - \left(v_\xi^w - v_\xi^{s,w}\right)t\right)^2}{4D_\zeta t} \right) \quad (3\text{-}29)$$

where M_s is the solute mass injected at location (x_0, y_0), and n is the porosity of the porous media. This equation shows solute concentration c_f at location (x, y) and time t.

The point source pollution involves injecting a mass of M_s = 10 g solute into the layer at location x_0 = 0.25 m and y_0 = 0.5 m. The proposed model used a 0.01 m square mesh for the layer. The modelling adopted the soil properties in Fox (2007b), which include the transverse dispersity of $\alpha_x^t = 0.01$, longitudinal dispersity $\alpha_\zeta^l = 0.1$, transverse seepage velocity $v_x^w = 5\times10^{-8}$ m/s, and the longitudinal seepage velocity $\left(v_\zeta^w - v^w\right) = 5\times10^{-9}$ m/s.

The analytical and numerical results are given in Figure 3-3. The results consist of the solute concentration isochrones drawn in vertical and horizontal directions at t = 1 × 10^6 seconds (i.e. 11.6 days). Excellent agreement between the numerical and analytical results is obtained. This means the numerical solutions for the point-source pollution induced solute transport are verified.

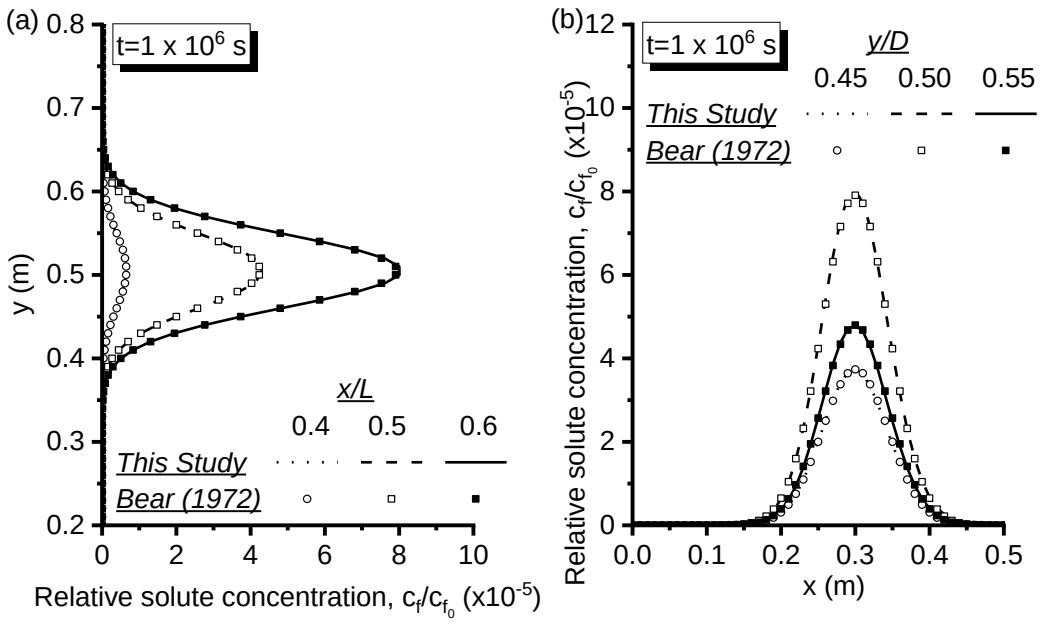

Figure 3-3. Solute concentration isochrones in porous medium: a) vertical profiles, and b) horizontal profiles.

3.4.2. Solute transport in compressible porous media

The solute transport in compressible porous media was verified against the experiment conducted by Lee and Fox (2009). The experiment setup as shown in Figure 3-4 mimics an oedometer consolidation cell. The kaolinite clay slurry is enclosed in a cylinder compartment. The slurry sample consists of the 21.1 mm uncontaminated layer and 50.6 mm contaminated layer, separated with the layer of filter paper. The porous disk at the top allows an open, equal-strain boundary. The vertical loads were applied in stages of 3.1, 5.6, 10.4 20.1 kPa, each load applied for 3 days. The effluent discharged at the top and bottom was collected to maintain the zero head boundary conditions.

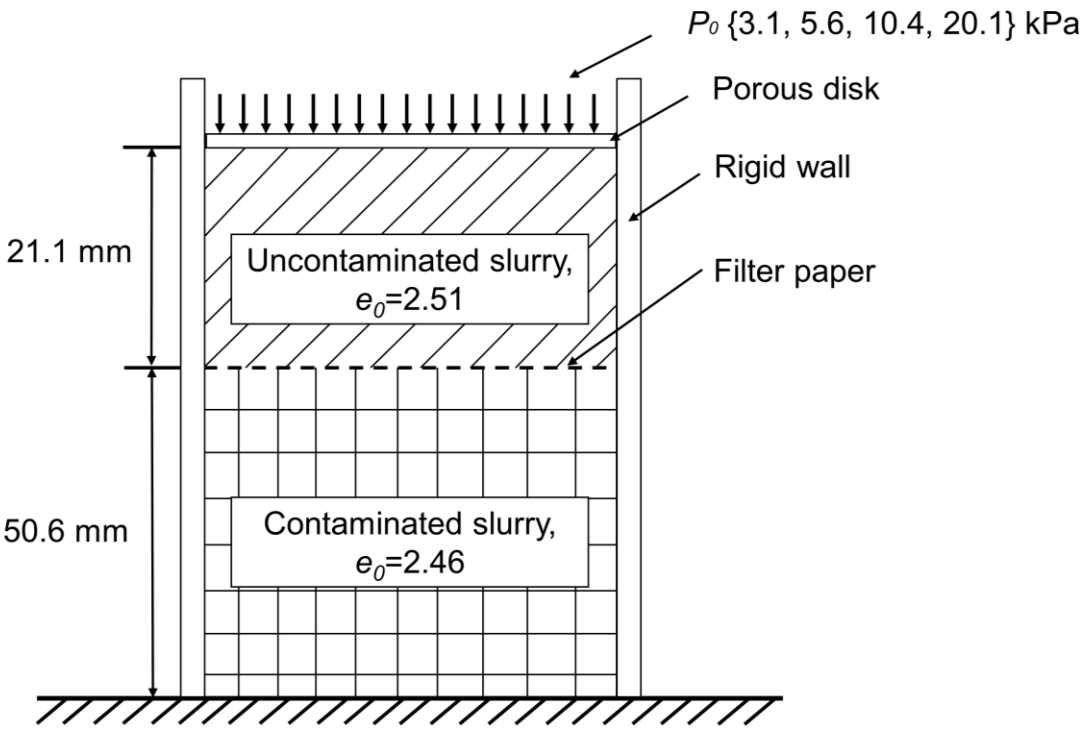

Figure 3-4. Diagram of one-dimensional consolidation induced solute transport.

Lee and Fox (2009) generated a volume of potassium bromide solution and used this solution to prepare the contaminated layer. The initial concentration was 270.4 mg/L. The other soil characteristics were: α_{ξ}^{l} = 20 mm, $D_{\xi,0}$ = 19.6 x 10^{-10} m^2/s, M_d = 1.82. They proposed to use the following compressibility and permeability relationships:

$$e = e_0 - C_c \log\left(\frac{\sigma'}{\sigma'_{ovb}}\right) \tag{3-30}$$

$$k_{\xi}^{w} = 10^{\frac{(e-\varepsilon)}{C_k}} \tag{3-31}$$

where $e = e^w$ when the soil is fully saturated, e_0 is the weighted initial void ratio and equals 2.47, ε is the permeability fitting parameter and equals 8.16, C_c and C_k are the compressibility and permeability coefficient and are 0.65 and 0.765 respectively, σ' is the effective

stress and equals $\left(\sigma_y - u^w\right)$, and σ'_{ovb} is the initial overburden stress. Using the method in Lee and Fox (2009) σ'_{ovb} was determined as 0.771 kPa. These parameters and relationships were adopted for the numerical simulations.

The solute breakthrough and layer settlement data are shown in Figure 3-5. The simulation results are in good agreement with the experimental results throughout. Notably, the simulations replicate the soil settlement and solute concentration induced by the staggered loading. The consolidation–solute coupled model is verified.

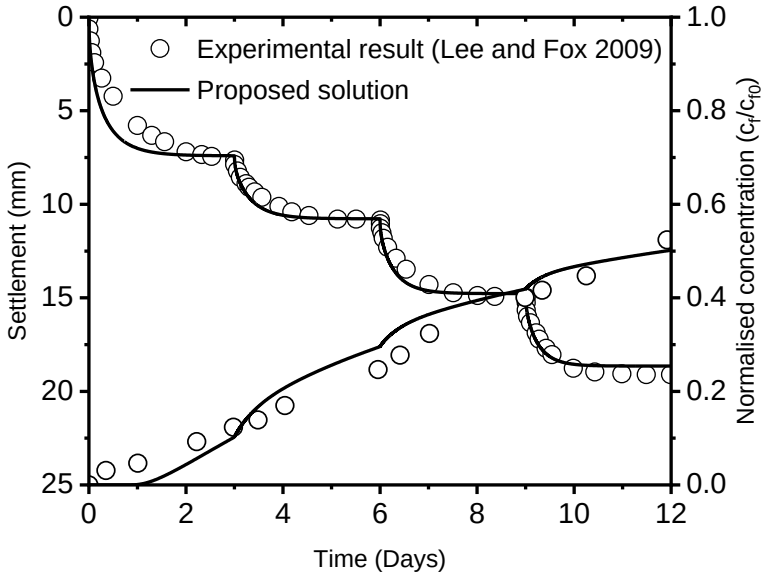

Figure 3-5. Consolidation settlement and solute breakthrough data from one-dimensional consolidation test.

3.5. Numerical simulations

The verified model was used to conduct numerical simulations, aiming to gain insights on effects of soil characteristics on consolidation induced solute transport. A soil layer, 2 (L) × 10 (H) m, is laterally enclosed by two vertical drains, as in Figure 3-1 (a). The soil layer is uniformly contaminated with a solute concentration C_0 = 100 mg/mL, and is consolidated by means of vacuum pressure or surcharge preloading, so to compare clean-up effectiveness of the two consolidation means. The simulation cases, including the consolidation methods and boundary conditions, are summarised in Table 3-1. Case A involves the conventional preloading consolidation applied to a fully saturated layer with open top and closed bottom boundaries. Case B also uses preloading consolidation, but the layer is partially saturated, with open lateral boundaries and closed top and bottom boundaries. Cases C and D apply vacuum pressures to fully saturated layers. Case C is aided with a drained top boundary, and Case D is not. Each of the four cases applies a vertical load of Δq = 100 kPa at the top boundary. Note the 100 kPa load in Cases C and D arises from the 100 kPa vacuum pressure, assuming no vacuum pressure drop.

Solutes in Cases A to D can transport in different processes depending on the solute nature. Four transport models are considered as given in Table 3-2. Model 1 combines advection and diffusion processes and suits less reactive, less adsorptive solutes. Model 2 considers relatively reactive but less adsorptive solutes, and Model 3 for relatively reactive, adsorbable solutes.

Table 3-1. Consolidation methods and soil conditions

Case	Consolidation method	Soil layer	Lateral boundary	Top boundary	Bottom boundary
A	Preloading without vertical drain	Fully saturated	Closed	Open	Closed
B	Preloading with vertical drain	Partially saturated	Open	Closed	Closed
C	Vacuum-aided vertical drain	Fully saturated	Open	Open	Closed
D	Vacuum-aided vertical drain	Fully saturated	Open	Closed	Closed

Table 3-2. Solute transport processes considered (Pu and Fox (2015))

Solute transport model	Advection	Diffusion	Dispersion	Sorption
1	✓	✓	×	×
2	✓	✓	✓	×
3	✓	✓	✓	✓

3.5.1. Solute transport in fully saturated layer

Cases A, C and D involve solute transport in a fully saturated layer under the different boundaries. The case examples are solved by applying the constitutive relations of saturated soils i.e., Eqs. (3-30) and (3-31) to the consolidation–solute transport governing equations (Eqs. (3-5) and (3-16)). The soil properties are sourced from Lee and Fox (2009), as shown in Table 3-3. A small initial preconsolidation

stress of 0.5 kPa was used to determine the parameters. Note the soil layer is isotropic during the simulation.

Table 3-3. Soil parameters and initial conditions for saturated soil layer.

Parameter	Value
Initial diffusion coefficient, $D_{x,0}$, $D_{\xi,0}$	19.6×10^{-10} m^2/s
Initial void ratio, e_0^w	2.47
Compression index, C_c	0.65
Hydraulic conductivity index, C_k	0.765
Diffusion constant, M_d	1.82
Dispersion constant, α_x^t, α_ξ^l	0 for solute transport Model 1 and 0.2 m for Models 2 and 3,
Freundlich's isothermal constant, K^d	0 for solute transport Models 1 and 2 and 1.96 mg/L for Model 3
Permeability fitting parameter, ε	8.16
Specific gravity, G_s	2.61

The simulation results are given in Figure 3-6. The figure shows the consolidation settlement and solute transport towards t = 1,000 days for Cases A, C and D where solute transport Models 1 to 3 are considered. In the figure, the solute concentration is defined as the layer averaged normalised concentration (LANC), $LANC = \sum_{i=1}^{N}\sum_{j=1}^{M} c_f{}^t \,/\, \sum_{i=1}^{N}\sum_{j=1}^{M} c_f{}^0$. The results suggest that the solute concentration is related to the consolidation methods and solute transport processes considered. For example, the non-adsorbed reactive chemicals are cleaned up faster in solute transport Model 2 than in the other models. This finding agrees with the results in Fox (2007b). The sorption effect, i.e. solute transport Model 3. significantly reduces the solute transport due to the chemicals adsorption to the

solid particles. Similar effects were also reported by Fox (2007b) and Zhang et al. (2013).

For reactive chemicals, the fluid flow affects the solute transport process. For example, Case C yields relatively higher settlement, and hence facilitates the reactive chemical discharge. In contrast, Case A shows the lowest settlement and hence the chemicals trend to dissipate relatively slower. The non-reactive chemical (as of solute transport Model 1) is independent to the solute discharge where the solute discharge curves from different consolidation cases overlap.

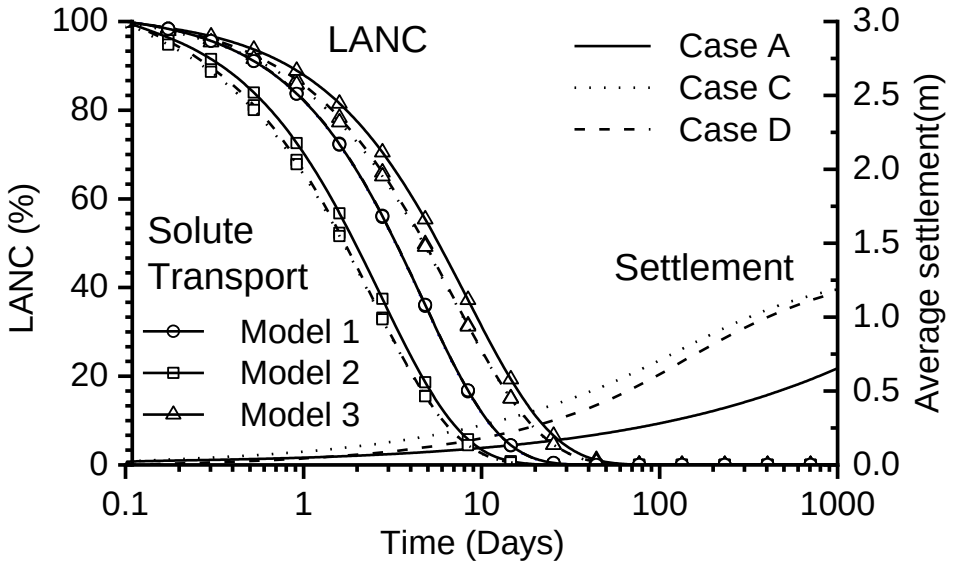

Figure 3-6. Settlement and concentration profile for Cases A, C and D.

To gain further insights into the solute concentrations at a location, the proposed model calculates the normalised solute concentration, i.e., $\left(c_f{}^t / c_f{}^0\right)\times 100\%$, in the soil layers of Cases A, C and D. The solute concentrations are presented in contours as shown in Figure 3-7 to Figure 3-9. Each example case examines the three solute transport scenarios Models 1 to 3 for the soil layer at three time points, i.e., t = 1,

2.5, and 5 days, when major changes to solute concentration occur. The results of after 5 days gradually move towards full clean-ups.

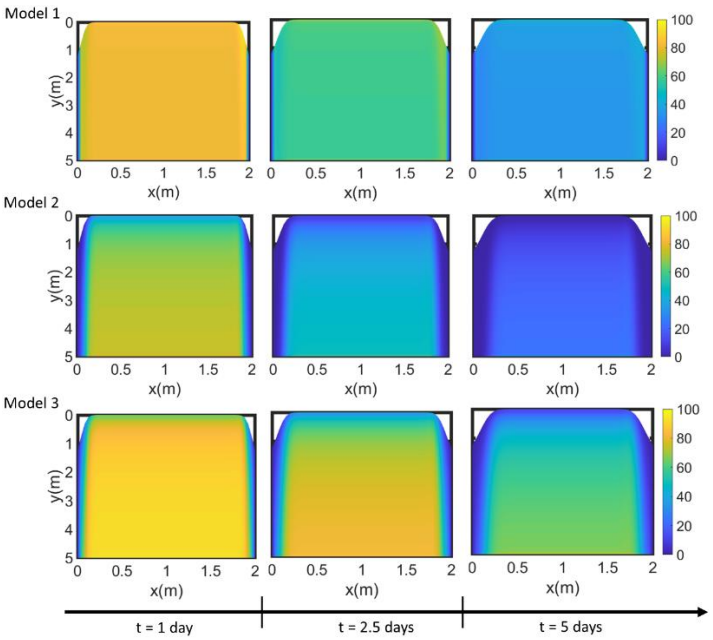

Figure 3-7. Solute concentrations at t = 1, 2.5 and 5 days for consolidation Case A considering solute transport Models 1, 2 and 3.

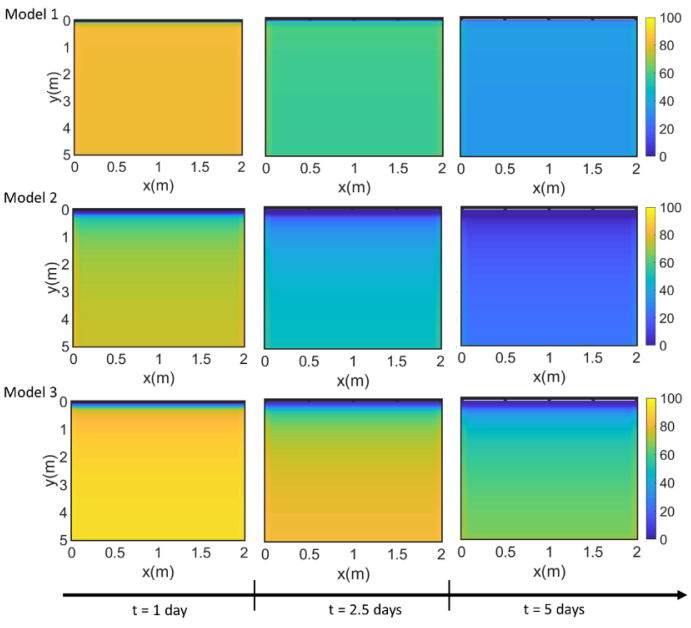

Figure 3-8. Solute concentrations at t = 1, 2.5 and 5 days for consolidation Case C considering solute transport Models 1, 2 and 3.

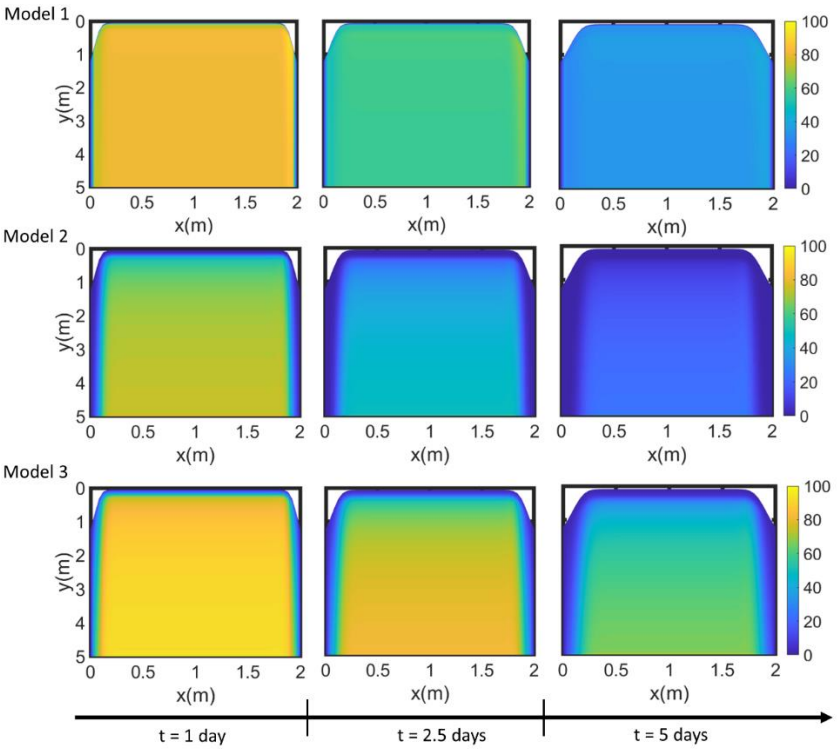

Figure 3-9. Solute concentrations at t = 1, 2.5 and 5 days for consolidation Case D considering solute transport Models 1, 2 and 3.

When the solutes are non-reactive and Model 1 governs the solute transport, the solute distributes uniformly across the layer as shown in Figure 3-7 (a) to Figure 3-9 (a). The even solute distribution results suggest that the solute is cleaned up at same rate in the layer, regardless of the different boundary conditions applied. This is because the transport of non-reactive chemicals is solely related to the advection and diffusion coefficient which is determined by the soil matrix. Despite the consolidation method, the concentration at the boundary layer is drained instantaneously, followed by concentration within the layer moving toward the boundaries. The solute concentration gradually decreases when the location moves from the

domain centre towards the boundaries, which agrees with the analytical results of Bear (1972).

For reactive, non-adsorptive chemicals, i.e., solute transport Model 2, the use of the vertical drain path (Case C) does not affect the solute transport significantly, whereas fluid is discharged significantly faster. One reason is that the porosity at the top boundary is reduced significantly, which in turn further reduces the solute transport parameter at the top boundary. The top boundary becomes less permeable to the solute, hence reducing the solute breakthrough. The reactive chemicals transport at a lower rate than the non-adsorptive chemicals due to the mass of chemicals adsorbed on solid particles.

Overall, the solute transport is clearly related to the consolidation method and the solute reactivity. For non-reactive chemicals, the choices of consolidation methods do not change the solute transport. For reactive chemicals, the greater the settlement and settlement rate are, the faster the solute will transport. Therefore, it is suggested to consider the use of both horizontal and vertical drainage to effectively remediate a land that is polluted with reactive chemicals.

3.5.2 Solute transport in partially saturated layer

Simulation Case B mimics solute transport in a partially saturated layer caused by the 100 kPa surcharge load. The load causes an initial excess pore water and pore air pressure as determined from Dakshanamurthy and Fredlund (1980) and Huangfu and Deng (2023). The soil profile is sourced from sample 12442 of Basaltic clay from SoilVision database (The Bentley System Team 2020). In addition to the solute transport characteristics in Table 3-3, the soil has the following assumed values, i.e., the residual volumetric water content of

θ_t = 0.05, the initial degree of saturation of S_r = 90%, and the initial suction pressure of ψ = 74 kPa. Note that the definition of the Hydraulic conductivity index, C_k, remains the same as in the fully saturated state, i.e., $C_k = 0.5e_0$. However, it's important to clarify that the initial void ratio, represented as e_0 in above expression refers to the initial soil void ratio during the laboratory test. In the context of soil consolidation problems, the term 'initial void ratio' specifically denotes the void ratio of the in-situ overburden soil conditions. The initial void ratio is obtained by fitting the saturation degree and suction into the water retention curve. The hydro-mechanical characteristics of the unsaturated soil, i.e., the soil shrinkage curve, soil-water characteristic curve and compression curve, and permeability curve are the same as in Huangfu and Deng (2023). Other soil properties are given in Table 3-4.

Table 3-4. Unsaturated soil properties.

Parameter	Value
Saturated water content, w_s	0.84
Residual soil suction, h_r (kPa)	714.41
Hydraulic conductivity index, C_k	0.765
Permeability fitting parameter, ε	8.16
Coefficient of compression, C_c	0.33
Water retention curve parameter, a_f	9.96
Water retention curve parameter, n_f	0.62
Water retention curve parameter, m_f	0.81
Minimum void ratio, a_{sh}	0.44
Slop of the line of tangency, b_{sh}	0.16
Curvature of the shrinkage curve, c_{sh}	3.04
Matric suction adjustment factor, C_{a1}	86.9
Matric suction adjustment factor, C_{a2}	3.45
Matric suction empirical index, C_e	0.28
Parameter for permeability function, λ	0.12
Dry permeability of air, k_d^a (m/s)	1.25×10^{-7}

The simulation results for Case B are given in Figure 3-10. The results consist of the normalised pore water and pore air pressure over time and the normalised solute concentrations for solute transport Models 1 to 3. The pore water pressure exhibits a two-stage dissipation process. The first stage of towards t = 0.2 day is coupled with the air dissipation. In this stage, the pore air pressure dissipates at a fast rate, providing immediately accessible space for pore water pressure to dissipate at a similarly fast rate. The dissipation coupling process at stage 1 leads to the completion of pore air dissipation and approximately 70% dissipation of pore water pressure. Moving into t > 0.2 day, i.e. the second stage of consolidation, solo pore water dissipation occurs and the process is noticeably slower, attaining 5% pore water dissipation towards t = 1,000 days. This means approximately 25% pore water pressure remains at t = 1,000 days. The two stage dissipation of pore pressures agree with the studies conducted by Qin et al. (2010), Ho et al. (2016) and Huangfu and Deng (2023).

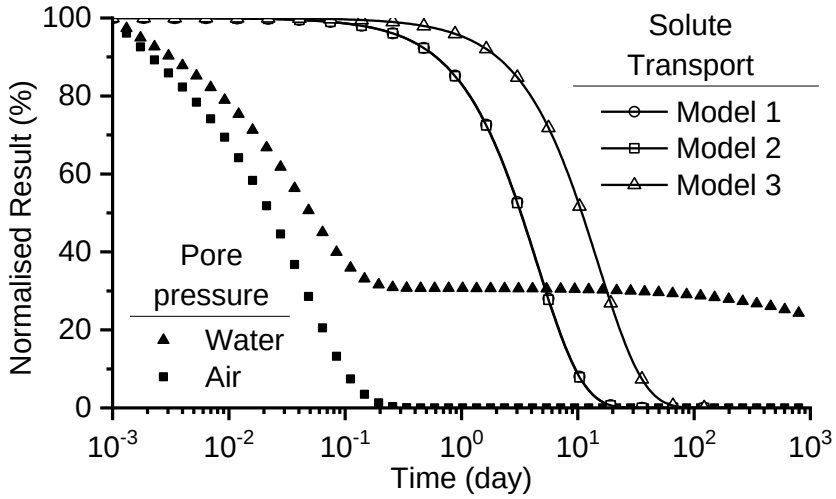

Figure 3-10. Pore pressures and solute concentrations versus time for Case B.

The two stage dissipation processes affect the solute concentration profiles. No significant changes of the solute concentration occur in the first stage. Noticeable clean-ups occur in the period of t = 0.2 to 10 days where transport Models 1 and 2 are considered, and to up to 100 days for Model 3. Interestingly, the solute profiles for Models 1 and 2 overlap, suggesting neglectable effects of dispersion (of relatively reactive chemicals) on solute clean-up. Sorption, the additional process in Model 3, is time-consuming, therefore the longer period for chemicals to clean up. Note similar solute profile differences occur to the saturated layers (Figure 3-6). For example, the profiles for Model 3 are approximately 40 days delay in relation to Models 1 and 2. The comparison results indicates the marginal effects of the soil saturation condition on the chemical sorption process.

3.6. Discussion

The proposed model can simulate consolidation induced solute transport in two-dimensional conditions of from fully to partially saturated soils. The model uses the finite strain theory and deformable coordinate system. As a result, the simulations are more reliable and open to most hydro-mechanical constitutive models. The solver algorithm ADI-FDTD features unconditional stability and computation efficiency, outperforming the traditional finite difference and finite element methods. It took less than 2 minutes to execute the simulations for the 4,000 mesh domain towards elapsed time 1,000 days.

Albeit computationally stable and efficient, the proposed model has limitations. The first limitation is related to the assumptions made to develop the model. The dispersion relationship calculates the dispersion coefficient using merely the gravimetric water content.

Effects of soil suction, net stress and void ratio are ignored. Similarly, the adsorption relationship neglects effect of soil suction on adsorption capacity. A further investigation is needed to correlate suction, net stress, void ratio and degree of saturation to dispersion and sorption relationships. The model can also be improved by simulating more complex while practical situations. One situation is a soil layer containing a volume of air bubble which identifies the layer nearly saturated but complicates consolidation and solute transport processes. Additional research lies in examining environmental effects, i.e., evaporation and infiltration on consolidation and solute transport. A solution is to determine the access to air, water, and solute at the boundaries and to use a decision model to formulate the top boundary conditions.

3.7. Conclusions

A consolidation-induced solute transport model was developed. The model considers the finite deformation consolidation in fully and partially saturated soil layers and determines the consolidation induced solute transport in two-dimensional space. The model integrates non-linear soil and solute transport characteristics and is solved using an unconditionally stabilised ADI-FDTD algorithm. The model was applied to predict the transport of reactive and non-reactive chemicals in fully and partially saturated soil layers and arrived at the following results.

The lateral flow path enhances the consolidation efficiency and accelerates the chemical clean-up. The effects of consolidation on chemical clean-up are significant for fully reactive chemicals, moderate for reactive, non-adsorptive chemical, and marginal for non-reactive chemicals. For non-reactive chemicals, the dispersion effect facilitates

the solute discharge, and the combined sorption and dispersion effects significantly reduce the discharge rate.

The excess pore water pressure in unsaturated soil dissipates in two stages. Stage 1 involves water–air coupled flow, completion of pore air pressure, and fast dissipation of pore water. Stage 2 is a solo process of pore water dissipation, and the process is relatively slow. Stage 2 significantly reduces the chemical dispersion process. Similar chemical sorption effects are in fully and partially saturated soils.

3.8. Nomenclature

Roman

A_1, A_2, A_3	Coefficients of consolidation for air flow
ℓ	Parameter for permeability function
a_f	Water retention curve fitting parameter
a_{sh}	Minimum void ratio
b_{sh}	Slope of line of tangency
C_1, C_2, C_3, C_4	Coefficients of solute transport
C_{a1}	Matric suction adjustment factor
C_{a2}	Matric suction adjustment factor
C_c	Coefficient of soil compressibility
C_e	Matric suction empirical index
C_k	Coefficient of soil permeability
C^{aw}	Compressibility of water−air mixture, kPa^{-1}
C^w	Compressibility of water, kPa^{-1}
c_0	Solute concentration at boundary
c_f	Solute concentration
c_{sh}	Curvature of shrinkage curve
D	Hydrodynamic dispersion coefficient

D^f	Free diffusion coefficient
D^*	Effective dispersion coefficient
e	Soil void ratio
e_0	Initial soil void ratio
e^a	Air void ratio
e_0^a	Initial air void ratio
e^w	Water void ratio
e_0^w	Initial water void ratio
$f'_{a\to s}$	Sorption induced solute loss
Gs	Specific gravity of soil
g	Gravitational acceleration, m/s^2
H	Height of soil layer, m
h_r	Residual matric suction
i	The i^{th} node in horizontal direction
J_f	Fluid flux in Cartesian coordinate
j	The j^{th} node in vertical direction
K^d	Freundlich linear isothermal constant
k	Coefficient of permeability
L	Spacing of vertical drains, m
M	Ratio between temporal and spatial coordinate
M_d	Diffusion constant
M_s	Solute mass
m	Coefficient of unsaturated soil volume change
m_f	Water retention curve fitting parameter
m_v	Coefficient of saturated soil volume change
N	Number of meshes in vertical direction
n	Porosity

n_f	Water retention curve fitting parameter
P_0	Pressure at boundary
Q	Number of meshes in horizontal direction
R	Universal gas constant, J/mol/K
S	Sorption ratio
S^r	Degree of saturation
t	Elapsed time, s
Δt	Time step increment, s
u'	Excess pore pressure vector
u	Pore pressure, kPa
$u^{'a}$	Excess pore air pressure, kPa
u^a_{atm}	Absolute pore air pressure, kPa
u^a_{atm}	Standard atmosphere, kPa
$u^{'w}$	Excess pore water pressure, kPa
$u'_t(i, j)$	Excess pore pressure vector of node (i, j) at time t, kPa
$u^{'w}_t(i, j)$	Excess pore water pressure of node (i, j) at time t, kPa
v^s_ξ	Velocity of soil particles in vertical direction due to water flow, m/s
v^w_x	Actual velocity of water in horizontal direction, m/s
v^w_ξ	Actual velocity of water in vertical direction, m/s
w_1, w_2, w_3	Coefficients of consolidation for water flow
w_s	Saturated gravimetric water content
χ	Abscissa in Lagrangian coordinate
y	Ordinate in Lagrangian coordinate

Greek

Δ	Differential change
α^l_ξ	Longitudinal dispersity

α_x^t	Transverse dispersity
β_ξ, β_x	Longitudinal and transverse mechanical dispersion parameter
ε	Permeability fitting parameter
ζ_{t+1}^a	Elevation of element (x_t, y_t) due to air flow
ζ_{t+1}^w	Elevation of element (x_t, y_t) due to water flow
θ	Volumetric water content
θ_k	Temperature in Kelvin scale, K
θ_t	Residual volumetric water content
ρ^a	Density of air, kg/m^3
ρ^s	Density of soil element, kg/m^3
σ'	Effective stress
σ'_{ovb}	Initial overburden stress
σ_x	Horizontal total stress, kPa
σ_y	Vertical total stress, kPa
γ^w	Unit weight of water, kN/m^3
ψ	Matric suction
ω	Molecular mass of air, kg/mol

Superscripts

a	Pore air
b	Parameter for permeability function
c	Parameter for permeability function
F	Parameter for nonlinear Freundlich isotherm
M	Parameter for saturated soil dispersion coefficients
s	Soil solid particles
w	Pore water

Subscripts

0	Initial condition

$_1$	With respect to net stress
$_2$	With respect to matric suction
$_t$	Time
$_x$	Horizontal direction in Spatial coordinate system
$_y$	Veridical direction in Spatial coordinate system
$_\xi$	Veridical direction in Temporal coordinate system

Coordinates

x	Horizontal axis in Spatial coordinate system
y	Veridical axis in Spatial coordinate system
ξ	Veridical axis in Temporal coordinate system

Chapter 4 Large strain consolidation model of vacuum and air-booster combined dewatering

Zhihao Huangfu[1], An Deng[1,*]

[1] School of Architecture and Civil Engineering, The University of Adelaide, Adelaide, SA5005, Australia;

[*] Corresponding Author
E-mail address: an.deng@adelaide.edu.au

Statement of Authorship

Title of Paper	Large strain consolidation model of vacuum and air-booster combined dewatering
Publication Status	☐ Published ☐ Accepted for Publication ☑ Submitted for Publication ☐ Unpublished and Unsubmitted work written in manuscript style
Publication Details	Huangfu, Z., and Deng, A., 2023, Large strain consolidation model of vacuum and air-booster combined dewatering. Computers and Geotechnics, under review.

Principal Author

Name of Principal Author (Candidate)	Zhihao Huangfu		
Contribution to the Paper	Conception; Acquiring data; Knowledge; Analysis; Drafting		
Overall percentage (%)	85%		
Certification:	This paper reports on original research I conducted during the period of my Higher Degree by Research candidature and is not subject to any obligations or contractual agreements with a third party that would constrain its inclusion in this thesis. I am the primary author of this paper.		
Signature		Date	05 July 2023

Co-Author Contributions

By signing the Statement of Authorship, each author certifies that:

i. the candidate's stated contribution to the publication is accurate (as detailed above);

ii. permission is granted for the candidate in include the publication in the thesis; and

iii. the sum of all co-author contributions is equal to 100% less the candidate's stated contribution.

Name of Co-Author	An Deng		
Contribution to the Paper	Conception; Knowledge; Analysis; Review		
Signature		Date	6/07/23

Name of Co-Author			
Contribution to the Paper			
Signature		Date	

Please cut and paste additional co-author panels here as required.

Abstract

Vacuum aided prefabricated vertical drain (PVD) is an established ground improvement method. Mimicking drinking straws, PVDs are installed to convey vacuum pressure in the ground and lift groundwater. The dewatering performance are suboptimal in consolidating fine-grained layers. Practical applications have shown that better dewatering performance is achieved through aiding the vacuum dewatering with an air-booster. Air boosters are installed in an alternate pattern adjoining PVDs, adding to pore pressures and unclogging pores. This study presented a numerical model for this vacuum and air-booster combined dewatering solution. Taking account of the large strain deformation, this model used the Lagrangian-convective coordinate to track the global and local deformation of the soil layer separately, thus enabling accurate determination of consolidation. This model also considered air booster induced unsaturated conditions and the associated effects on water flow. The numerical model was verified against the field test results and laboratory measurement.

Keywords: Vacuum consolidation; air booster; unsaturated soil; vertical drain; tensile fracture; shear fracture

4.1. Introduction

Soil consolidation can upscale field conditions but is time consuming. Earlier attempts (such as Barron 1948) were to install vertical drain to facilitate consolidation, which however is costly in haulage and earthwork. Kjellman (1952) replaced embankment preloading with vacuum aided preloading, which proves cost effective in applications (such as Gao and Zhang 2020; Indraratna et al. 2011; Rujikiatkamjorn et al. 2007). Albeit promising, the dewatering performance of the vacuum preloading diminishes with time mainly due to clogging (Shi et al. 2018; Yang et al. 2014). One solution is to flush soil and unclog pores using pressurised air and meanwhile to raise effective stresses (Shen et al. 2015). Field tests demonstrated that the proposed method can effectively unclog pores and accelerate consolidation (Cai et al., 2019; Feng & Zhou, 2022; Wang et al., 2016).

Research was conducted to assess vacuum and air-booster combined consolidation. Lu and Sun (2022) modelled the combined consolidation in an axisymmetric condition. Their model was based on conventional sand drain consolidation theory, with the air booster treated as an impulse load. Their model was further improved by Sun and Lu (2023) who considered the drain clogging effect. Their studies assumed saturated conditions of soils. However, in dewatering practice, the subsoils are not always fully saturated and may not be governed by conventional fully saturated soil formulations. The unsaturated conditions are sourced from the pressurised air. Once the applied pressure exceeds the tensile or shear failure threshold of soil, the soil becomes unsaturated (Hu et al. 2021). The air booster can decrease the degree of saturation by up to 10% (Yao et al. 2023). To these ends,

it is required to consider soil unsaturation when assessing the vacuum and air-booster combined consolidation.

The vacuum and air-booster combined dewatering also leads to large deformation, typically exceeding 25% strain (Anda et al., 2020; Wang et al., 2016). The large strain deformation causes changes to soil compressibility and permeability (Geng & Yu, 2017; Huangfu & Deng, 2023; Wang et al., 2020). Conventional small strain modelling in an Eulerian coordinate system (such as Lu & Sun, 2022; Sun & Lu, 2023) is not adequately accurate as it neglects the non-linear changes in soil parameters. Large strain modelling approach is needed.

In this paper, a two-dimensional numerical model governing the vacuum–air booster consolidation was proposed. The model incorporated the large strain deformation, the deformable coordinate system, and the unsaturated soil conditions induced by the air booster. The governing equation was solved numerically. To validate the proposed model, a comparison between the model result and the field measurement was conducted.

4.2. Model development

4.2.1. Coordinate system

A soil layer with a width of *L* and a depth of *H* is laterally enclosed with two vertical drain wells, as in Figure 4-1a. The tips of the drains are connected to the vacuum pump and air pump respectively, providing the lateral boundaries for water lift and air injection. The upper boundary is the airproof membrane sealing the soil layer, and the lower the impermeable stratum as the datum.

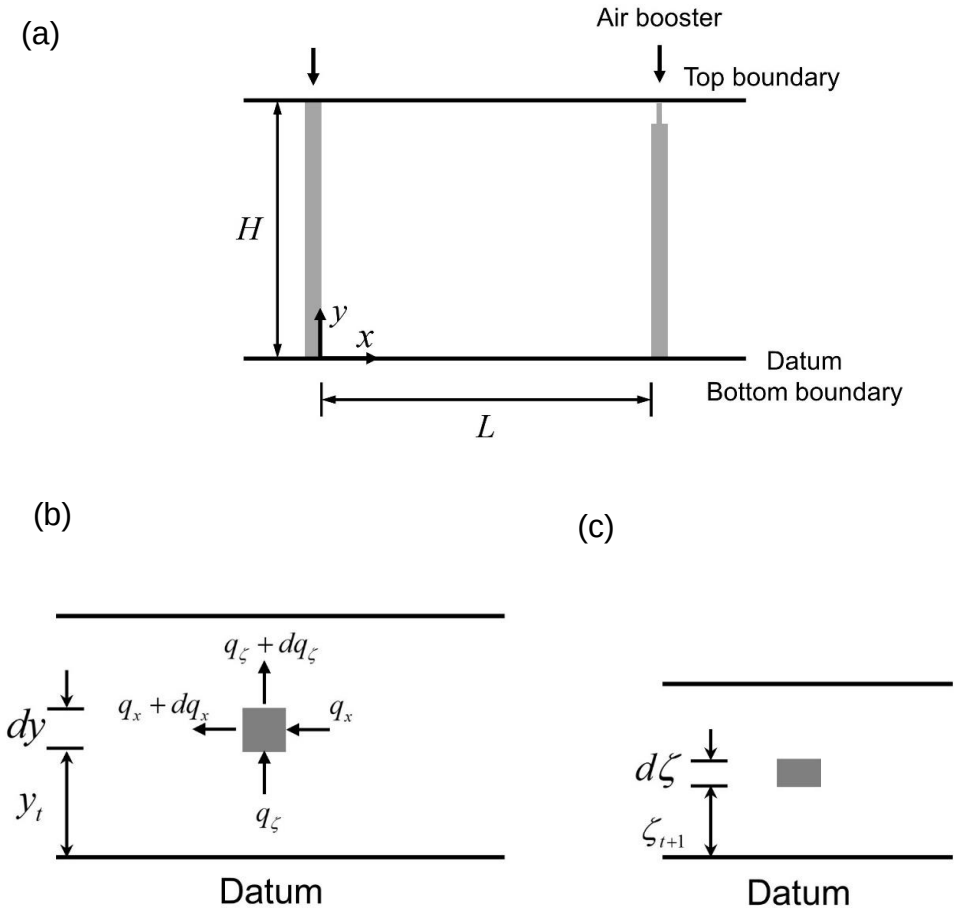

Figure 4-1. Model geometry of soil layer (a) elevation in x–y plane; (b) example element in Lagrangian (global) coordinate; and (c) example element in convective (local) coordinate

The soil layer sits on the Lagrangian-convective coordinate, as shown in Figure 4-1(b and c). The Lagrangian-convective coordinate consists of two coordinates, i.e., the Lagrangian (called *global* thereafter) coordinate and the convective (called *local* thereafter) coordinate. The global coordinate (x, y) uses the vertical axis y (against the datum) to capture the total deformation of the soil layer; the local coordinate ζ which is fixed in the soil layer captures soil element deformation. The

example soil element has *dx*, *dy* and *dζ* for the width and the height in global coordinate, and the height in local coordinate respectively.

The global and local heights are correlated. In global coordinate (*x*, *y*), due to the water discharge, the element height, d*y*, reduces to *dζ*, over a time step increment. Meanwhile, the location of the element in the local coordinate is updated to (x, ζ_{t+1}). The updated location can also be explicitly substituted into the global coordinate, feeding the next computation loop. As per Gibson et al. (1981) the transformation between the global and local coordinate systems is written as

$$\frac{\partial \zeta}{\partial y} = \frac{1+e}{1+e_0} \tag{4-1}$$

where *e* is the void ratio and subscribe $_0$ is the initial condition.

4.2.2. Consolidation equation

As in Zhang et al. (2013), the fluid phase continuity is governed by:

$$\frac{\partial}{\partial t}\left(nS\rho_w \frac{\partial \zeta}{\partial z} \right) = -\nabla\left(\rho_w q\right) \tag{4-2}$$

where *t* is the time of consolidation, *n* is the porosity and is written as *e*/(1+*e*), *S* is the degree of saturation, ρ_w is the fluid density, and *q* is the flow rate and as shown in Figure 4-1 comprises q_x *and* q_y in horizontal and vertical directions respectively. Geng and Yu (2017) suggested to express the flow rate as:

$$\begin{cases} q_x = \dfrac{k_x}{\rho_w g}\dfrac{\partial u'}{\partial x} \\ q_y = \dfrac{k_\zeta}{\rho_w g}\dfrac{\partial u'}{\partial \zeta} \end{cases} \tag{4-3}$$

where k_x and k_z are horizontal and vertical permeability respectively, *g* is the gravitational acceleration, and *u*' is the excess pore water

pressure. Assuming the fluid phase is a barotropic phase, Fredlund et al. (2012) proposed the following relationship:

$$\frac{\partial \rho_w}{\partial u} = \beta \rho_w \tag{4-4}$$

where u is the pore water pressure, and β is the pore compressibility parameter and falls in the range of $2\text{x}10^{-6}$ – $2\text{x}10^{-7}$ for saturation degree of 80% to 100% (Zhang et al. 2012). Substituting Eqs. (4-1), (4-3) and (4-4) into Eq. (4-2), gives:

$$Sn\beta \frac{\partial u'}{\partial t}\frac{\partial \zeta}{\partial y} + \frac{\partial S}{\partial t}\frac{\partial \zeta}{\partial y} = \frac{1}{\rho_w g}\frac{\partial}{\partial x}\left(k_x \frac{\partial u'}{\partial x}\right) + \frac{1}{\rho_w g}\frac{\partial}{\partial y}\left(k_\zeta \frac{\partial u'}{\partial \zeta}\frac{\partial \zeta}{\partial y}\right) \tag{4-5}$$

The self-weight of the soil changes during the consolidation. As per Fredlund et al. (2012), the vertical total stress satisfies the relationship:

$$\frac{\partial \sigma}{\partial \zeta} = \rho_b g \tag{4-6}$$

where ρ_b is the bulk density of the soil. Similarly, the hydrostatic pressure satisfies the relationship:

$$\frac{\partial u}{\partial \zeta} = \rho_w g \tag{4-7}$$

Substituting the effective stress concept, i.e., $\sigma' = \sigma - u - u'$, the soil compressibility coefficient, i.e., $a_v = -\partial e / \partial \sigma'$, and Eq. (4-6) to Eq. (4-7), the changes of the excess pore water pressure in horizontal and vertical direction are written as:

$$\begin{cases} \dfrac{\partial u'}{\partial x} = \dfrac{1}{a_v}\dfrac{\partial e}{\partial x} \\ \dfrac{\partial u'}{\partial \zeta} = \left(\rho_b - \rho_w\right) g + \dfrac{1}{a_v}\dfrac{\partial e}{\partial \zeta} \end{cases} \tag{4-8}$$

Differentiating each side of the effective stress equation, $\sigma' = \sigma - u - u'$, the change of the excess pore water pressure with respect to time, $\partial u' / \partial t$, is expressed as:

$$\frac{\partial u'}{\partial t}=\frac{\partial \sigma}{\partial \zeta}\frac{\partial \zeta}{\partial t}-\frac{\partial u}{\partial \zeta}\frac{\partial \zeta}{\partial t}-\frac{\partial \sigma'}{\partial \zeta}\frac{\partial \zeta}{\partial t} \tag{4-9}$$

Substituting Eqs. (4-6) and (4-7), and the change in booster pressure, $\partial Q/\partial t$, to Eq. (4-9), givens:

$$\frac{\partial u'}{\partial t}=\frac{\left(\rho_b-\rho_w\right)g\triangle z}{1+e_0}\frac{\partial e}{\partial t}+\frac{\partial Q}{\partial t}+\frac{1}{a_v}\frac{\partial e}{\partial t} \tag{4-10}$$

Substituting Eqs. (4-8) and (4-10) to Eq. (4-5), the consolidation of the nearly saturated soil in the global coordinate is governed by:

$$\begin{aligned}&\frac{\partial e}{\partial t}\left[\frac{Sn\beta\left(\rho_b-\rho_w\right)g\triangle z}{\left(1+e_0\right)}+\frac{Sn\beta}{a_v}+\frac{\partial S}{\partial e}\right]+Sn\beta\frac{\partial Q}{\partial t}=\\&\frac{1+e_0}{\rho_w g}\frac{\partial}{\partial x}\left(\frac{k_x}{a_v\left(1+e\right)}\frac{\partial e}{\partial x}\right)+\frac{1+e_0}{\rho_w g}\frac{\partial}{\partial y}\left(\frac{k_\zeta}{a_v\left(1+e\right)}\frac{\partial e}{\partial y}\right)\end{aligned} \tag{4-11}$$

where $\partial S/\partial e$ can be obtained through the soil shrinkage curve.

4.2.3 Tensile and shear failure

Soil becomes unsaturated when the pressurised air penetrates the soil–drain interface and causes cracks (Anda et al. 2020). The cracking involves two soil failure types, i.e., tensile failure and shear failure (Zhang et al., 2008). The occurrence of tensile and shear cracks leads to soil unsaturation, consequently impacting the degree of saturation in Eq. (4-11). The tensile failure applies when the minor principal stress become negative, equal to, or greater than the soil tensile fracture strength. Anda et al. (2020) suggested to determine the tensile fracture threshold, $P_{f,t}$, as:

$$P_{f,t}=3\sigma_3-\sigma_2+\sigma_t \tag{4-12}$$

where σ_2 and σ_3 are middle and minor principal stresses respectively, and σ_t is the tensile strength of the soil.

The shear fracture occurs when the applied booster pressure crosses the Mohr-Coulomb strength envelope. Based on this concept, Anda et al. (2020) determined the shear fracture threshold, $P_{f,s}$, as:

$$P_{f,s} = \frac{1}{2}(3\sigma_3 - \sigma_2)(1+\sin\phi) + c\cos\phi + \frac{\sigma_t}{2}(1+\sin\phi) \quad (4\text{-}13)$$

where ϕ is the internal angle of friction and c is the undrained shear strength of the soil and is estimated as:

$$c = \frac{1}{(I_L - 0.21)^2} \quad (4\text{-}14)$$

where I_L is the liquidity index.

It should be noted that the friction angle ϕ and tensile strength σ_t are assumed to be zero under undrained conditions. A lateral pressure coefficient at rest of $K_0 = 0.6$ is assumed (Anda et al. 2020).

4.3. Numerical solutions

The proposed consolidation governing equation, i.e., Eq. (4-11), was solved numerically using the finite difference method. The *alternative direction implicit finite different time domain method* (ADI-FDTD) offers unconditional stability (Douglas and Rachford 1956; Staker et al. 2003) and outperforms the conventional explicit scheme in reducing time step restrictions and achieving computational efficiency. Therefore, ADI-FDTD was used to solve the governing equation.

The finite difference mesh is shown in Figure 4-2. The mesh, which coincides the soil layer in x–y plane, comprises M x N elements, each element in $\Delta x \times \Delta y$ dimensions. The soil properties of each element are represented by node (i, j), where i = 1, 2, …, M, and j = 1, 2, …, N. The computation runs over time, $z\Delta t$, where Δt represents the time

increment and *z* is the time step number, i.e., ***z = 0, 1, 2, …, ∞.*** Note that the ADI-FDTD scheme splits the single time step into two sub-steps, i.e., 0 to 0.5Δt and 0.5Δt to Δt. In the first sub-step, the soil layer *(L* x *H)* is discretised implicitly along the y-direction and discretised explicitly along the x-direction, namely *y*-sweep. Similarly, *x*-sweep comprises an implicit discretisation along the *x*-direction and an explicit discretisation along the *y*-direction, as shown in Figure 2.

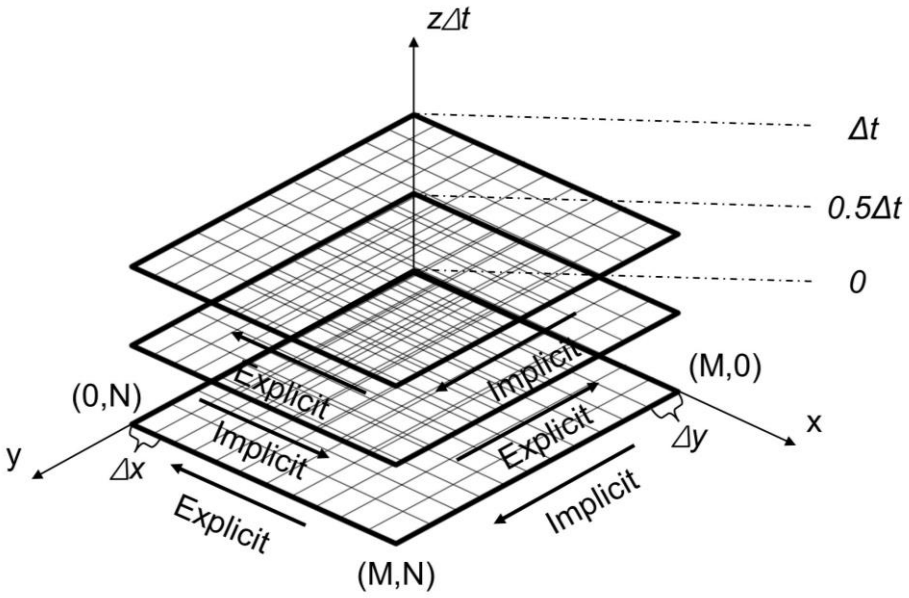

Figure 4-2. Explicit–implicit difference model

As specified in the consolidation model on Figure 4-1, the soil layer has the following boundaries: a closed top, $\partial e_{i,1}^{t} / \partial t = 0$, a closed bottom, $\partial e_{i,N}^{t} / \partial t = 0$, and an open PVD, $e_{1,j}^{t} = e_{r(1,j)}$, where e_f is the final void ratio and is determined from the compression line as:

$$e_{r(1,j)} = e_{0(1,j)} - \frac{a_v \left(\sigma'_{0(1,j)} + Q(t) - p(t) \right)}{0.435} \log_{10} \left[\frac{\left(\sigma'_{0(1,j)} + Q(t) - p(t) \right)}{\sigma'_{0(1,j)}} \right] \quad (4\text{-}15)$$

where $Q(t)$ is the booster pressure and $p(t)$ is the vacuum pressure. Note that the compression index, C_c, in Eq. (4-15) was expressed in term of the coefficient of compressibility, a_v, i.e., $a_v = 0.435C_c/\sigma_{av}$ as per (Lambe and Whitman 1979), where σ_{av} is the average effective stress. Assumes the time increment is relatively small, the ultimate effective stress can be adapted to represent the residual consolidation state. The air booster boundary can be open when the air booster is on and closed when switched off, and accordingly is written as:

$$\begin{cases} \dfrac{\partial e^t_{M,j}}{\partial t} = 0, \text{ if } Q(t) = 0 \\ e^t_{M,j} = e_{0(M,j)} - \dfrac{a_v\left(\sigma'_{0(M,j)} + Q(t) - p(t)\right)}{0.87}\log_{10}\left[\dfrac{\left(\sigma'_{0(M,j)} + Q(t) - p(t)\right)}{\sigma'_{0(M,j)}}\right], \text{ if } Q(t) > 0 \end{cases} \quad (4\text{-}16)$$

Using the boundary conditions, Eq. (4-11) is solved, giving the void ratio of each of the elements at any time. The void ratio is used to determine column i settlement, ε_i^t, as:

$$\varepsilon_i^t = H - \sum_{j=1}^{N} \Delta y \frac{1 + e_{i,j}^j}{1 + e_{i,j}^0} \quad (4\text{-}17)$$

Using the settlement, the average degree of consolidation, U_{avg}, is:

$$U_{avg} = \sum_{i=1}^{M} \varepsilon_i^t \Big/ \sum_{i=1}^{M} \varepsilon_i^{z\Delta t} \quad (4\text{-}18)$$

Figure 4-3 illustrates the program flow chart. The input data comprises the model geometry, time step increment, vacuum load, booster load, and soil parameters including permeability, degree of saturation, coefficient of lateral pressure, compressibility, friction angle, liquid limit, tensile strength, non-linear permeability curve and soil shrinkage curve. After the program reads the input data, the program initialises the problem, including the setup of the soil matrices and calculations for the initial void ratio, effective stress, and principal stresses. Following the problem initialisation, the program applies the time step increment and meanwhile switch on (or off) the air booster as scheduled. When

the booster is off, the program feeds the obtained data to the ADI-FDTD solver, updating the soil settlement and the void ratio. Note the degree of saturation remains unchanged when the booster is off. When booster is on, the ADI-FDTD solver runs the algorithms. Upon completion of each iteration, the applied booster pressure is compared with the soil principal stresses on the soil–booster interface, determining the soil fracture type. The degree of saturation of each soil element is updated based on the fracture type. Then the algorithms update the void ratio and soil settlement. Upon termination of the computation, the program calculates the degree of saturation, U_{avg}.

4.4. Model validation

The proposed model was validated against the field test results in Wang et al. (2016). The field test comprised the dewatering of the soft clay in Wenzhou, China, using the air booster aided vacuum consolidation method. The field layout coincides with the model in Figure 4-1. The 0.4m (L) x 4m (H) soil layer was laterally enclosed by two vertical drains. The PVD was connected to the vacuum pump with a vacuum pressure of 80 kPa, and the air booster conduit to the air pump with a booster pressure of 20 kPa. The booster was switched on 98 days following the start of the vacuum dewatering and ran 2 hours per day for 15 days in parallel aiding the vacuum dewatering. The soil properties are shown in **Table 4-1**. Besides, a typical value of pore compressibility parameter, $\beta = 1 \times 10^{-7}$ as suggested by Zhang et al. (2013) was adopted. The threshold values of saturation were 95% in the tensile failure condition and 90% in the shear failure condition. A hydraulic conductivity correlation, i.e., $k=k_0 x 10^{(e-e0)/Ck}$, from Geng and Yu (2017) was adopted to model the non-linear hydraulic conductivity change, where C_k is the hydraulic conductivity coefficient and is

typically taken as $0.5e_0$. As the soil shrinkage behaviour was not tested in the referenced field test, three assumed linear shrinkage values were adapted, i.e., 0.15, 0.2 and 0.25. Note the actual shrinkage curve is non-linear and requires the combination of water retention and compression curve to determine the gradient. Tensile strength and internal angel of friction were assumed zero in the undrained condition, and as per Anda et al. (2020) the lateral pressure coefficient used K_0 = 0.6.

Table 4-1. Soil parameters from dewatering site

Soil Property	**Value**
Initial soil void ratio, e_0	1.4
Initial degree of saturation, S_0	100%
Horizontal permeability, k_x	5.6 x 10^{-8} m/s
Vertical permeability, k_ζ	2.9 x 10^{-8} m/s
Compressibility coefficient, c_c	0.8
Liquid limit, I_L	50%
Bulk unit weight, γ_b	16.5 kN/m^3

The numerical results, versus the field results, are provided in **Figure 4-4**. The results are the settlement accumulated over the 113 days dewatering time. Three scenarios were tested, and the results suggested that the soil unsaturation properties predominate the consolidation process. The $\partial S/\partial e = 0.15$ was most suitable for the referenced field test. Albeit the minor discrepancies at the initial stage, good overall agreement between the proposed model and the field measurement was achieved. There are no direct reasons for the discrepancies, but soil variability can be a potential cause as reported in similar observations from Lu and Sun (2022) and Peng et al. (2022). The validation suggests that the proposed model can predict the consolidation induced by vacuum and air booster combined method.

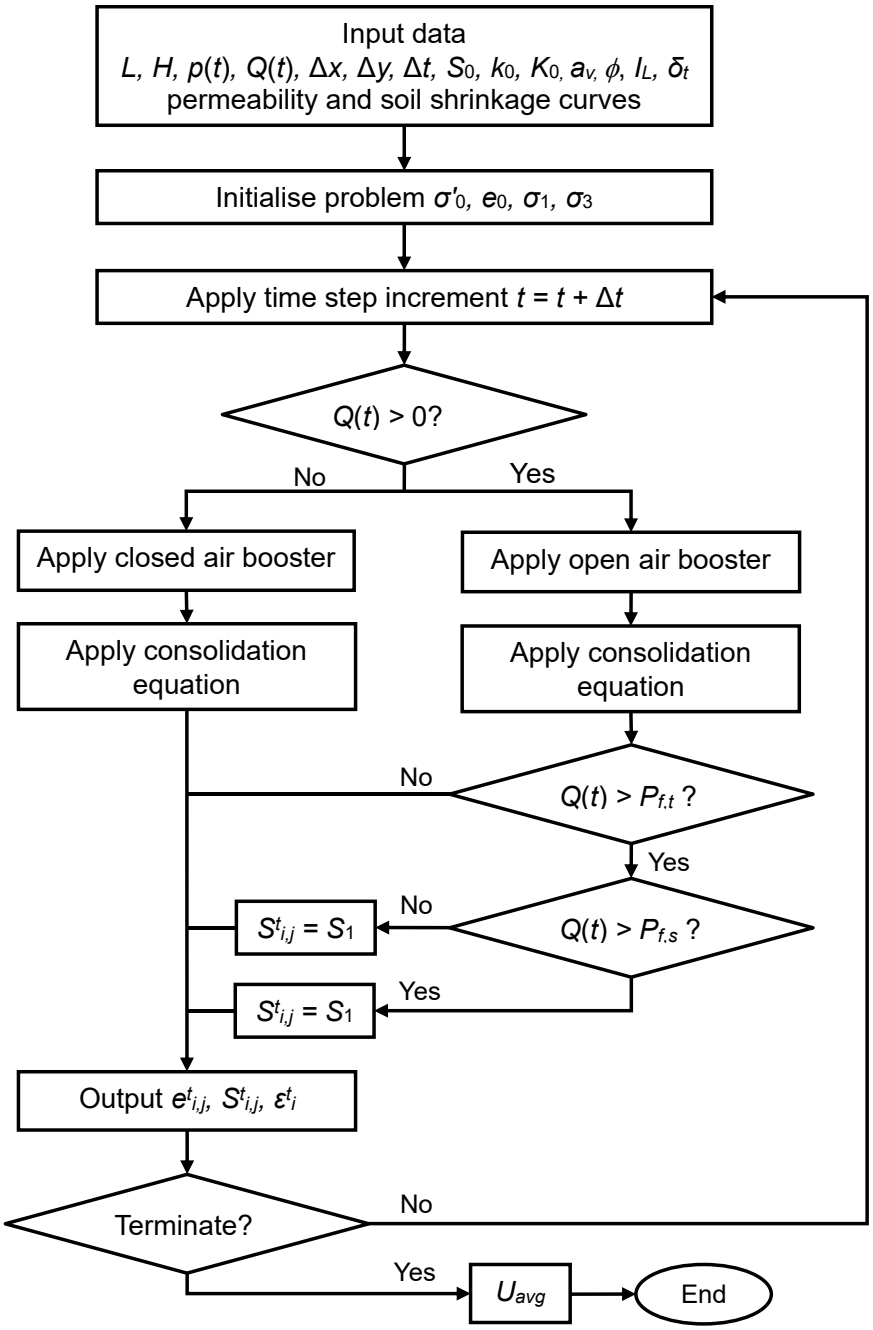

Figure 4-3. Program flow chart

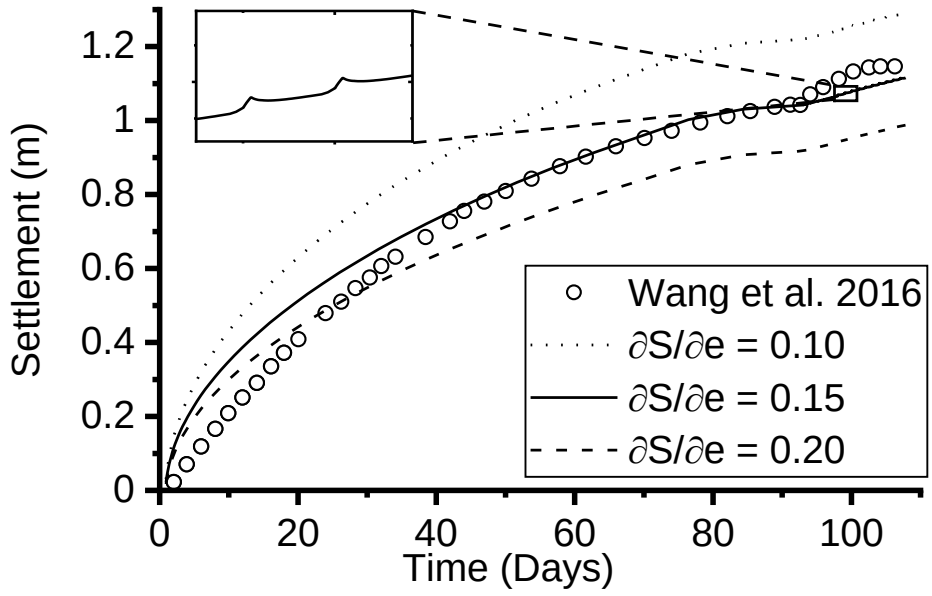

Figure 4-4. Model validation against field test results

Additional model verification was conducted against experimental results in Anda et al. (2020). The meso-scale laboratory test involved a model cylinder with a diameter of 560 mm and a height of 1200 mm. PVD drains were installed at intervals of 400 mm, and a booster tube was placed between the drains. A layer of clayey silt/ silty clay, measuring 1100mm in thickness, was added to the cylinder. Various standard soil parameters, such as particle size distribution and Atterberg limits, were determined. Empirical models, including those proposed by Bilardi et al. (2020) and Azzouz et al. (1976) were employed to estimate the soil's hydro-mechanical properties. The soil properties are shown in **Table 4-2**. The unsaturated soi properties, shrinkage, and tensile/shear fracture parameters are assumed identical to the field verification.

A vacuum pressure of 90 kPa was maintained throughout the experiment via the PVD, while a booster pressure of 20 kPa was

applied through the booster tube for 2 hours each day, commencing 12 days after the application of the vacuum pressure. **Figure 4-5** shows the comparison between the laboratory test and the proposed model. Good agreement was achieved when $\partial S/\partial e = 0.15$. Some discrepancies were observed, which may be attributed to the absence of laboratory measurements for certain soil parameters, especially the unsaturated soil properties and soil consolidation behaviours, including compressibility and permeability.

Table 4-2. Soil parameters from the laboratory test

Soil Property	**Value**
Initial soil void ratio, e_0	2.7
Initial degree of saturation, S_0	100%
Horizontal permeability, k_x	1 x 10^{-8} m/s
Vertical permeability, k_ζ	1 x 10^{-8} m/s
Compressibility coefficient, c_c	0.8
Liquid limit, I_L	50%
Specific gravity, G_s	2.72

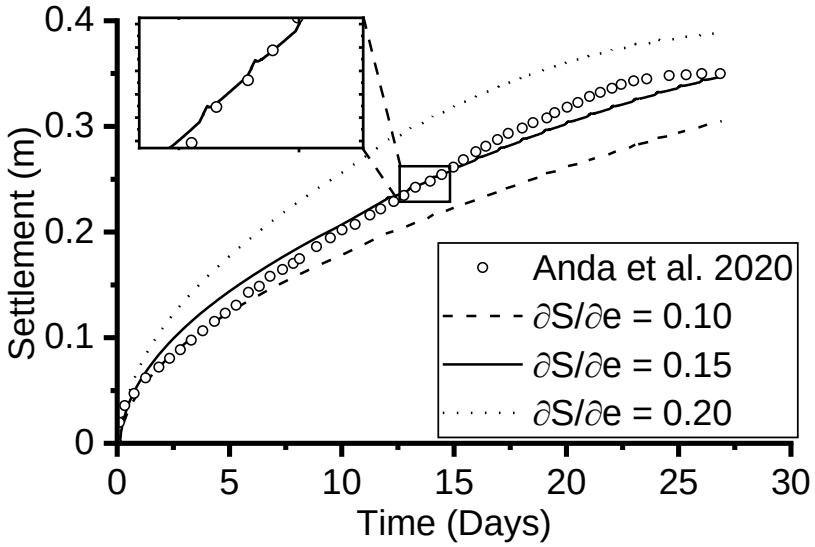

Figure 4-5. Model validation against laboratory test

Figures 4-4 and 4-5 also depict soil settlement when the booster tube is activated. It can be observed that the soil experiences a rapid increase in settlement when the booster tube is activated, followed by a gradual decrease when the booster pressure is removed, thereby indicating the effectiveness of the air-booster.

4.5. Conclusion

This paper developed a new model for the hybrid vacuum–air booster consolidation. The proposed governing equation used the two-dimensional Lagrangian-convective coordinate system to model the dewatering processes and the soil settlement. This equation integrates the air-booster induced soil unsaturation and non-linear soil parameters. The equation can determine the soil void ratio, consolidation degree, and settlement in a soil layer at any time. The proposed equation was solved numerically using the alternative direction implicit finite difference time domain method. The solution was verified against the field measurement and laboratory test. The proposed model can depict the settlement induced by the air-booster, and hence highlights the effectiveness of the air-booster

Chapter 5 Modelling air-water flow in vertical drain

Zhihao Huangfu[1], An Deng[1]*, Zhao Tian[2]

[1] School of Architecture and Civil Engineering, The University of Adelaide, Adelaide, SA5005, Australia;

[2] School of Electrical and Mechanical Engineering, The University of Adelaide, Adelaide, SA 5005, Australia.

* Corresponding Author
E-mail address: an.deng@adelaide.edu.au

Abstract

Vacuum-aided vertical drain is an established method for dewatering. The pressure difference exerts a force inside the drain, lifting the groundwater and lowering the groundwater table. Along with the inflowing groundwater, a volume of air often gathers towards the drain and forms an air–water mixture transporting in the drainpipe. The presence of air complicates the pressures in the conduit and therefore affects the dewatering efficiency. This paper presented a numerical model for orifice-induced air–water flow in vertical drains. Using the mass conservation, the model can calculate pipe pressure distributions and water discharge capacity. The model was validated against the results obtained from the computational fluid dynamic calculations. The proposed model was applied to the example problems to examine the effects of orifices on the pipe pressure distributions, water discharge rates, and lift depths. Nonlinear pressure distributions occurred in the drainpipe, and pressure dropped more noticeably in the presence of air. More water was discharged when the orifice was located closer to the lower end than to the upper end. Under one standard atmosphere vacuum pressure the lift depth was approximately 6.3 to 7.5 m depending on the orifice size.

Keyword: Vacuum dewatering; vertical drain; water flow; CFD; lift depth.

5.1. Introduction

Vacuum dewatering is an approach widely used to lower groundwater tables. This approach applies a vacuum force in pipelines and lift groundwater to discharge. The lift depth and water volume to discharge, two dewatering performance indicators, are closely related to the nature of mass transporting in the pipelines. Air that is present in vadose zones often transports with water, forming an air–water flux (Indraratna et al. 2004; Qiu et al. 2007). The air–water flow complicates the determination of the two performance indicators drastically more than water flow does. The complication is evident from analogous examples such as oil–gas extracting (Hanafizadeh et al. 2011) and nuclear reactor coolant recirculating (Quiben 2005). An important step to achieve dewatering efficiency is to monitor pressure distributions in pipelines and to optimise dewatering design.

Pressures in confined pipelines diminish with distance, whether the flux comprises a single phase or a mix of gas and liquid. When transporting gas–liquid mixture, the pressures distribute in more complicate models than in a single-phase flow. The models depend on the flow patterns the fluxes take such as an annular, stratified or transitional pattern (Afshin and Swanand 2014; Ide and Matsumura 1990; Lee and Lee 2001; Lu et al. 2018). The flow pattern is mainly determined by the phase flow velocity and gas–liquid volume ratio (Cheng et al. 2008; Mishima and Ishii 1984; Wu et al. 2017; Xu and Fang 2014). Empirical models (such as Hamad et al. 2017; Kiran et al. 2020; Lockhart and Martinelli 1949; Müller-Steinhagen and Heck 1986) used the two-phase flow velocities as the initial conditions to estimate the pressure distributions in the pipelines or sand columns. Similar estimates were obtained by computational fluid dynamic (CFD) modelling

(Alizadehdakhel et al. 2009; Kiran et al. 2020). These studies can determine pressure drops where pipeline inlet conditions (e.g., gas or liquid moving velocity) are specified. When the inlet conditions are not given in applications such as dewatering, the pressure drops are yet determined. In addition, albeit versatile, the CFD modelling has limitations, such as, convergence difficulties (Vallée et al. 2008), sensitivity to models chosen (Lote et al. 2018), expertise skills for meshing, and high performance computer system (Lote et al. 2018).

In ground dewatering, gas and liquid flow velocities are not available to calculate vacuum pressure distributions. Possible solutions are to approximate two-phase flow based on one-phase flow scenarios (Moreno Quibén and Thome 2005) or to model pressure distributions using measured data (Amaziane et al. 2010; Bhagwat 2015). These approaches are empirical and fail to provide accurate enough results for complex two-phase flow scenarios. Advanced gas–liquid models (such as Conte 2004; Fredlund 1979; Qi et al. 2020; Sheng et al. 2008) can determine pore water and air pressures given the pressure boundary conditions. However, the solutions are restricted to porous media where air–water flow is induced by capillary actions or surcharge pre-loading. Li et al. (2013) studied gas-liquid flow in vacuum pipe when pumping sewage. Their study assumed that liquid and gas are injected at the pipe inlet. The conditions do not apply to vacuum dewatering. In summary, the past studies required the inflow speed of gas and liquid to determine the pressure distribution, air–water ratio and outflow speed when discharged. The inflow speed however is not available when performing vacuum dewatering. Instead, vacuum dewatering merely specifies pressures applied at the inlet and outlet. To these ends, research is needed to explore alternative solutions to depicting air–water flow characteristics.

This study developed a closed-form solution to vacuum powered two-phase flow in vertical drainpipes and presented algorithms to calculate pipe pressures distributions. This model can accommodate the pressures at the inlet and outlet and outperform the CFD modelling in the aspects of convergence, expertise skills and computational effort. Nevertheless, CFD modelling was employed to validate the proposed model. The validated model was applied to some interesting example problems, aiming to examine the effects of the air–water ratio on the vacuum pressure distribution and discharge rate. The solutions determine the maximum depth to lift water, the maximum water discharge rate, the minimum vacuum pressure required to lift water, and the air content, in the presence of air–water flow. The research results are expected to gain insights into vacuum-aided dewatering in particular the pressure variation in response to the transporting of air–water mixture and to optimise dewatering performance.

5.2. Model development

5.2.1 Geometry

An open-ended circular pipe, as shown in Figure 5-1a, has an internal diameter of D and a length of L. The pipe is adequately thin in relation to the diameter, so the thickness is negligible. The pipe sits vertically with the bottom inlet flush with the water table and the top outlet under a pressure P_{out}. The pipe is rigid and does not deform on exposure to the ambient pressure of P_0 (which is > P_{out}). The pipe wall is perforated with an array of (n–1) orifices, where n > 1. The series of orifices divide the pipe into n segments, at lengths of l_1, l_2, … l_n, respectively. The orifices are round, d_1, d_2, … $d_{(n-1)}$ in diameters, and presumably face the same angle. Each orifice allows free access to air.

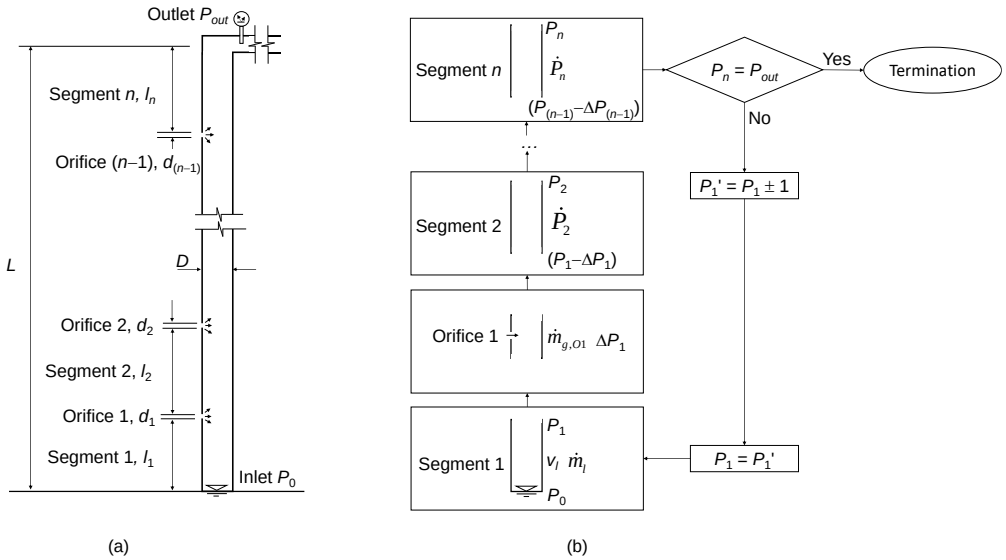

Figure 5-1. Dewatering by vertical drain: (a) Model geometry and (b) algorithm flow chart.

The pressure difference, ($P_0 - P_{out}$), drives a volume of water and air inflowing the pipe and transporting upward against the direction of gravity. The inflowing of water causes a pressure drop ΔP_0 at the inlet, and the inflowing of air causes pressure drops ΔP_i at Orifice i, where i = 1, 2, …, (n–1). Additional pressure drops, at gradient $\dot{P}_i$, occur over Segment i, due to the work acted against the gravity, skin frictions and fluid viscosity. Therefore, the pressure difference ($P_0 - P_{out}$) can be expressed as:

$$\left(P_0 - P_{out}\right) = \Delta P_0 + \sum_{i=1}^{n-1} \Delta P_i + \sum_{i=1}^{n} \dot{P}_i l_i \tag{5-1}$$

Note pressure gradient $\dot{P}_i$ on Segment i is constant as per the steady flow suggested by Lote et al. (2018) and Montoya et al. (2019). Eq. (5-1) is a linear indeterminate equation and can be solved by iterations.

5.2.2 Algorithms

The iterations to solve Eq. (5-1) are shown in Figure 5-1b. Instead of meshing the domain of problem, the proposed algorithm divides the domain into n segments based on the (n – 1) orifices. Iterative method is applied to the segments and orifices in sequence until the pressure difference converges. The first step is to initialise pressure P_1 at the upper end of Segment 1. The initial value of P_1 is determined by trialling a linear pressure distribution, i.e., $P_1 = P_0 - \left(P_0 - P_{out}\right)\left(l_1/L\right)$. Applying the pressure boundaries (P_0 and P_1) to Segment 1, the algorithms determine the water velocity, v_l, and water mass flow rate, $\dot{m}_l$. Moving up to Orifice 1, the algorithms determine gas mass flow rate, $\dot{m}_{g,O1}$, which enters the pipe through Orifice 1 and merges with the pipe water. The merging causes a pressure drop ΔP_1. The next step involves the air–water mixture transporting through Segment 2. The algorithms use the results of v_l, $\dot{m}_l$, $\dot{m}_{g,O1}$ and ($P_1 - \Delta P_1$) to calculate pressure gradient $\dot{P}_2$ and then upper end pressure P_2. Repeat the above processes towards Segment n and determine outlet pressure P_n. If pressure difference $\left(P_n - P_{out}\right)$ satisfies the pre-set small value of 1 Pa, the calculations converge and are terminated. Otherwise adjust initial pressure P_1 by 1 Pa and re-execute the algorithms. The algorithms are carried out by segments and orifices as outlined below.

5.2.2.1 Pressure drop on pipe Segment 1

Segment 1 involves water flow. The flow is governed collectively by the ambient pressure P_0, pressure drop at the inlet ΔP_0, pressure gradient $\dot{P}_1$ of Segment 1, segment length l_1, and the pressure at the upper end

P_1. The governing equation for the segment pressure drop, (P_0–P_1), is written as:

$$P_0 - P_1 = \Delta P_0 + \dot{P}_1 l_1 \tag{5-2}$$

where, ΔP_0 is related to the fluid momentum and as per Elger et al. (2016) is calculated as:

$$\Delta P_0 = \frac{1}{2}\rho_l v_l^{\,2} \tag{5-3}$$

where ρ_l and v_l are the density and superficial velocity (called velocity thereafter) of water respectively. Pressure drop $\dot{P}_1 l_1$ originates from the combined effects of skin friction, fluid viscosity and gravitation actions and is written as:

$$\dot{P}_1 l_1 = l_1 \rho_l g + \frac{f l_1 \rho_l v_l^{\,2}}{2d} \tag{5-4}$$

where g is the acceleration of gravity, and as per Swamee and Swamee (2007) hydraulic friction factor f is determined using the processes given in Appendix E. Note that the processes for friction factor f takes account of the fluid viscosity.

Substituting Eqs. (5-3) and (5-4) into Eq. (5-2) and rearranging Eq. (5-2), the velocity of water in Segment 1 is obtained as:

$$v_l = \left[\frac{2\left(P_0 - P_1 - l_1 \rho_l g\right)}{\left(1 + \frac{f l_1 \rho_l}{d}\right)} \right]^{\frac{1}{2}} \tag{5-5}$$

Note that the friction factor f is a function of the velocity of water, and hence Eq. (5-5) is solved using numerical iterations. Based on the velocity of water, the water mass flow rate in Segment 1, $\dot{m}_l$, is calculated as:

$$\dot{m}_l = \frac{\pi d^2}{4} v_l \rho_l \tag{5-6}$$

The water velocity v_l and mass flow rate $\dot{m}_l$ feed in Segment 2.

5.2.2.2 Pressure drop at Orifice 1

Pipe pressure drops when air enters the pipe through an orifice. The pressure drop, ΔP_1, at Orifice 1, is determined from Appendix D as:

$$\Delta P_1 = \frac{8\left(\dot{m}_{g,O1}\right)^2 RT}{MP_1\left(\pi d_1^{\,2}\right)^2} \tag{5-7}$$

where $\dot{m}_{g,O1}$ is the air mass flow rate, R is the ideal gas constant of 8.314 J/(K $\cdot$ mol), and T is the temperature of air in Kelvin, M is the molar mass of air and is 28.97 g/mol for dry air. Sharipov (2004) suggested to determine the air mass flow rate using the air pressure ratio, P_i/P_0, and the critical pressure ratio, r_c, which is given as:

$$r_c = \left(\frac{2}{\gamma+1}\right)^{\frac{\gamma}{\gamma-1}} \tag{5-8}$$

where γ is the specific heat ratio of air and is approximately 1.4 for air at the normal ambient conditions (Fujimoto and Usami 1984). When $P_i/P_0 \geq r_c$, the air mass flow rate through Orifice 1 is:

$$\dot{m}_{g,O1} = C\frac{\pi d_1^{\,2}\left(M\right)^{0.5} P_0}{4\left(2RT\right)^{0.5}}\left(\frac{P_1}{P_0}\right)^{\frac{1}{\gamma}}\left[\frac{\gamma}{\gamma-1}\left(1-\left(\frac{P_1}{P_0}\right)^{\frac{\gamma+1}{2}}\right)\right]^{0.5} \tag{5-9}$$

When $P_i/P_0 < r_c$, the air mass inflow rate is:

$$\dot{m}_{g,O1} = C\frac{\pi d_1^{\,2} P_0\left(2\gamma M\right)^{0.5}}{4\left(2RT\right)^{0.5}}\left(\frac{2}{\gamma+1}\right)^{\frac{\gamma+1}{2(\gamma-1)}} \tag{5-10}$$

where C is the discharge coefficient and as per Sharipov (2004) is related to the pressure ratio P_i/P_0 as given in Table 5-1.

Table 5-1. Air discharge coefficient for air passing through orifice.

Pressure ratio P_i/P_0	Air discharge coefficient C
0	0.835
0.1	0.830
0.5	0.742
0.9	0.632

5.2.2.3 Pressure drop on pipe Segment 2

Segment 2 involves a two-phase flow, comprising the mass of water inflowing from Segment 1 and the air entering through Orifice 1. Sadatomi et al. (1982) suggested to determine the pressure gradient of the two-phase flow, $\dot{P}_2$, using Eq. (5-11):

$$\dot{P}_2 = \dot{P}_{2grav} + \dot{P}_{2\,frict} \tag{5-11}$$

where $\dot{P}_{2grav}$ and $\dot{P}_{2\,frict}$ are the component pressure gradients induced by gradational and frictional forces respectively. Component pressure gradient $\dot{P}_{2grav}$ is written as:

$$\dot{P}_{2grav} = \left(\alpha\rho_g + (1-\alpha)\rho_l\right) g \tag{5-12}$$

where α is the air volume ratio as determined from Appendix E, and ρ_g is the density of air as determined in Appendix D. Component pressure gradient, $\dot{P}_{2\,frict}$, is determined from the velocities of air and water. Two models are available to calculate $\dot{P}_{2\,frict}$, i.e., the homogeneous flow model (HFM) and the separate flow model (SFM). SFM model works on the liquid and gas fluxes separately and combines the individual flux contributions to determine the total frictional pressure drop (Bhagwat

2015). As per Müller-Steinhagen and Heck (1986), the SFM model is written as:

$$\dot{P}_{2\,frict} = \Phi^2 \dot{P}_{2\,frict,l} \tag{5-13}$$

where Φ is the factor calculated using SFM correlations as in Appendix F, and $\dot{P}_{2\,frict,l}$ is the air–water equivalent pressure gradient and is determined as:

$$\dot{P}_{2\,frict,l} = f \frac{\left(\dot{m}_{g,O1} + \dot{m}_l\right)^2}{2\rho_l \pi d^3} \tag{5-14}$$

Note to use the total air mass flow rate for $\dot{m}_{g,O1}$ when determining pressure gradients for Segments 3 to *n*.

5.3. Validation

The proposed model was validated against the CFD simulations. The validation involved two parts: (i) the CFD parameters calibration, and (ii) the validation against the calibrated CFD model. Part (i) was to determine the computation mesh size, multiphase phase flow and turbulent model, and related discretisation method. Part (i) calibration used the experiment results in Lu et al. (2018). Following the calibration, the CFD and the proposed models were applied to the example problem of vertical drain to validate the proposed model.

Part (i) calibration used the experimental set-up in Lu et al. (2018). As shown in Figure 5-2a, an open-ended vertical pipe, with a D = 50.8 mm internal diameter and a L = 3,200 mm length, is exposed to an air–water injection at the bottom inlet. The air and water inject at an initial speed of (v_g, v_l) respectively, driving the air–water mixture towards the outlet. This calibration considered three speed combinations, (v_g, v_l) = {(0.15, 4), (0.52, 3), (1.3, 2)} m/s, representing

bubbly, *cap-bubbly* and *slug* flow patterns respectively. A 5×10^{-4} s time step was used to attain the convergence criteria: (i) < 1 x 10^{-4} residual, (ii) mass conservation, and (iii) steady volume ratio and pressures at the the outlet and mid-height. The grid sensitivity study arried at the optimal meshs as shown in Figure 5-2c. The meshes consists of a total of 450,000 three-dimensional hexahedron elements. O-grids refinement was applied to the air–water flux domain. The properties of water and air have been adapted from the *Fluent* database. The simulation used the Volume-of-Fluid (VOF) model (Appendix G) for the sake of no fluid interoperating, less computational effort, and reasonable accuracy (Alizadehdakhel et al. 2009). The standard *k-ε* model was selected due to its robust and efficient features in governing turbulent flow. The governing equations in Fluent were discretised using the parameter combinations of Coupled Pressure-Velocity, Least Square Cell Based Gradient, PRESTO pressure, and Second Order Upwind for Momentum, Volume Fraction and Turbulent Discretisation. CFD modelling results were benchmarked to the experimental results in Lu et al. (2018), as shown in Figure 5-3. Excellent agreement between the modelling and experimental results is obtained.

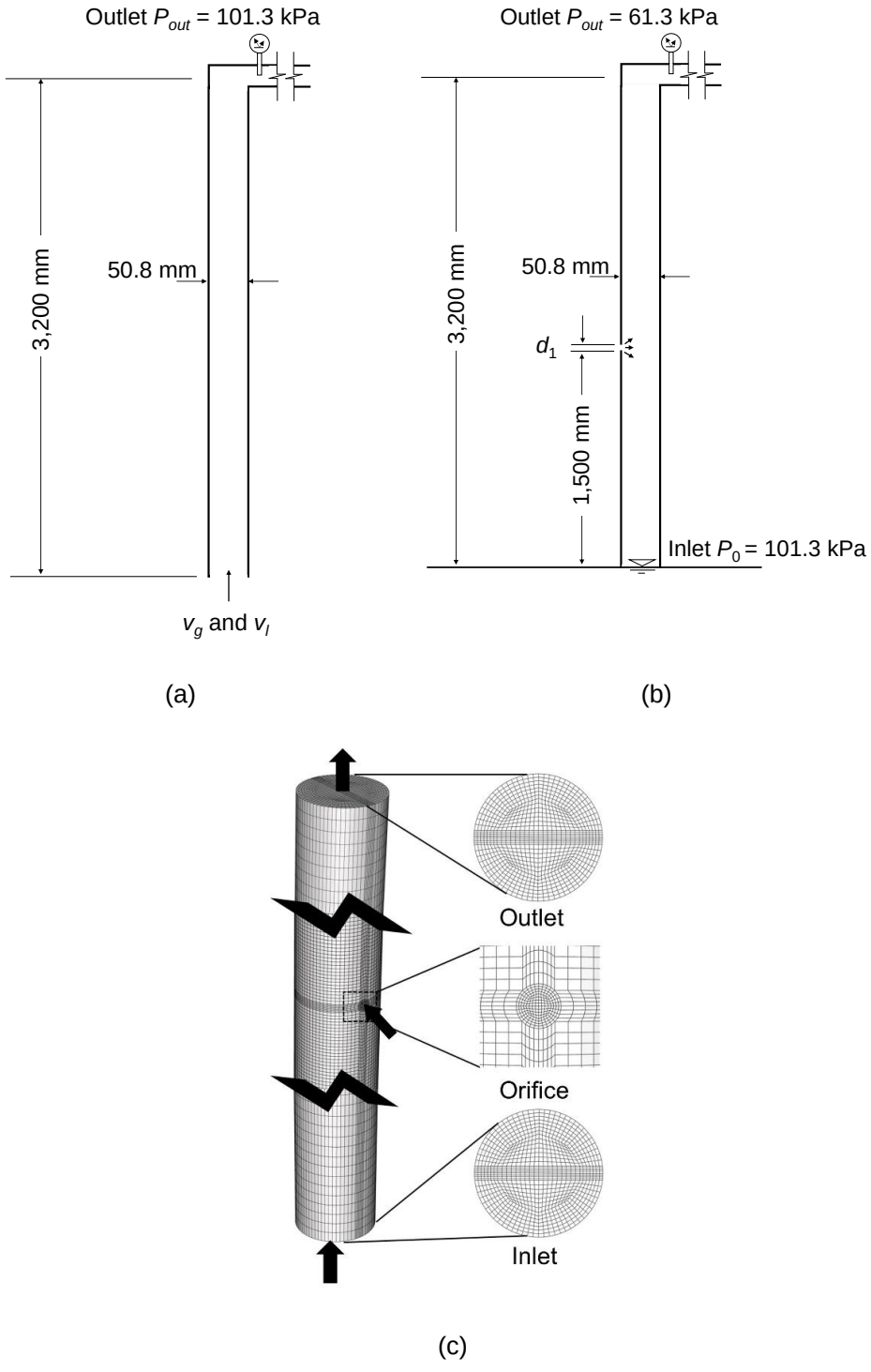

Figure 5-2. Vertical drainpipe for CFD parameter calibration and model validation: (a) Air–water flow in confined drainpipe, (b) orifice-induced air–water flow in confined drainpipe, and (c) CFD meshes.

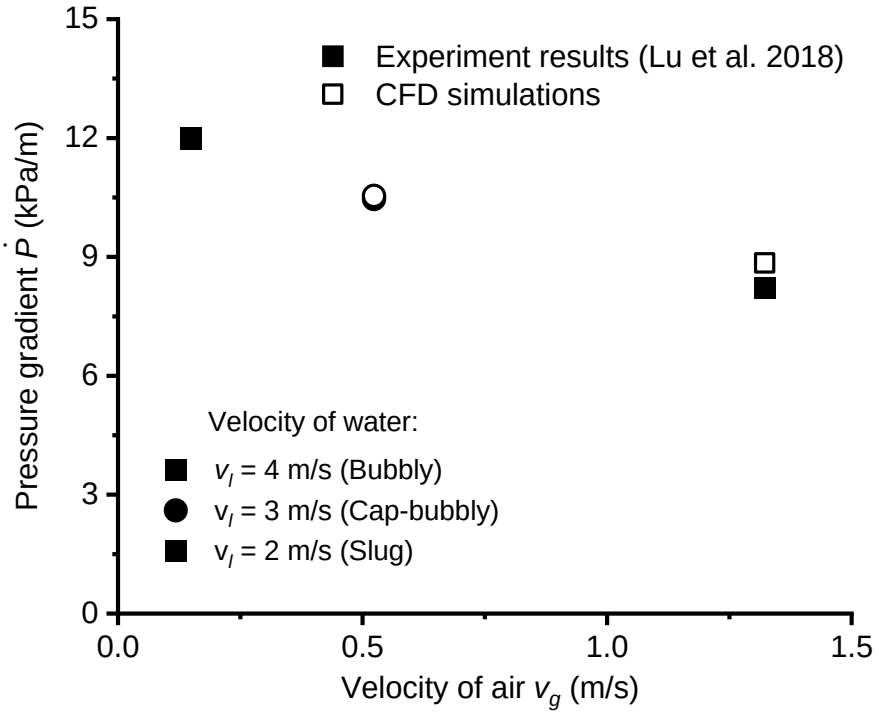

Figure 5-3. Pressure gradients in confined drainpipe comprising air–water mixture in different flow patterns.

Part (ii) involves validating the proposed model using the calibrated CFD model. Both models were applied to the orifice-induced two-phase flow in the drainpipe, as shown in Figure 5-2b. The drainpipe uses the same setting as in the CFD calibration (Figure 5-2a), except the presence of the groundwater table and the orifice. The orifice sits at 1.5 m above the groundwater table. The orifice is open to air, at P_0 = 101.3 kPa ambinent pressure. The vaccum equipment supplies a P_{out} = 61.3 kPa pressure at the outlet, therefore enabling a 40 kPa vacuum pressure across the pipe. The vacuum pressure draws a mass of water from the inlet and air from the orifice towards the outlet. The air–water mass flow obtained by the CFD simulation for a 4 mm orifice is given in Figure 5-4. The figure shows the air volume contours for a *t*

= 0 to 5 s period, on *x-y* and *z-y* planes respectively. Flow can be classified as the slug flow, agreeing to the flow pattern map in Afshin and Swanand (2014). The air volume ratios are varied with the location and time. At *t* = 0.75 s, the air–water volume becomes steady. These observations suggest that the CFD model can simulate the air–water flow and the simulation results are reasonably acceptable.

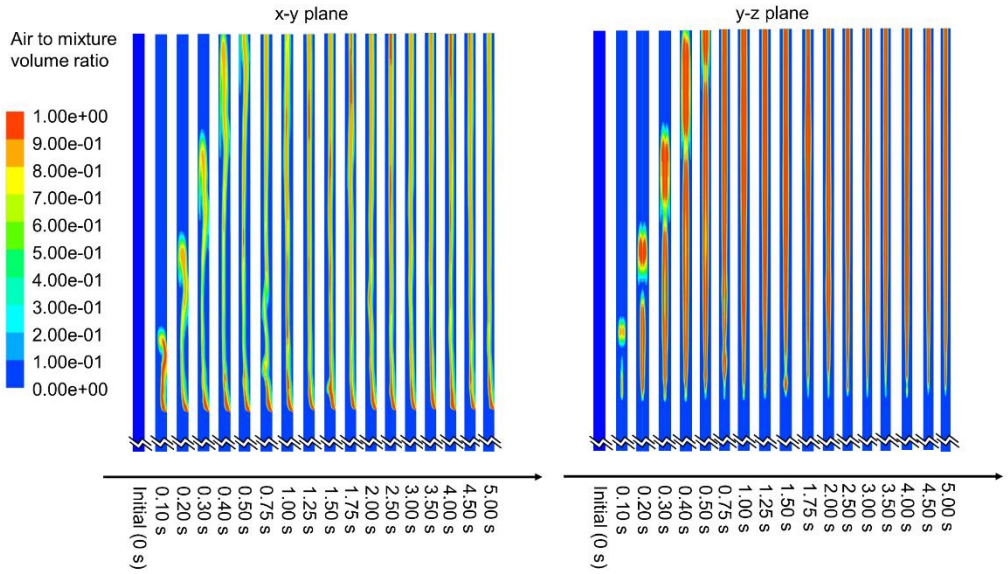

Figure 5-4. Air–water volume contours obtained by CFD simulation for dewatering using drainpipe of 4 mm orifice.

The model validation involved the dewatering in the presence of different orifice sizes, i.e., 2, 4, 6 and 8 mm. The results that were obtained from the CFD simulations and proposed model are given in Figure 5-5. The figure shows the pressure gradients above the orifice (i.e., air–water mixture). Reasonably good agreement between the CFD and the proposed model results is obtained. In addition, in terms of the flow pattern map in Afshin and Swanand (2014), the proposed model suggested a slug flow which agrees with the CFD simulations shown in Figure 5-4. These agreed results mean that the proposed model is validated to capture the air–water flow in the drainpipe. Note

that the proposed model used less than 1 minute for a standard office desktop to complete one scenario simulation. The computation cost is much lower than the over 72 hours for the CFD to complete the same workload, despite the time on meshing and model calibration. The proposed model is computationally efficient.

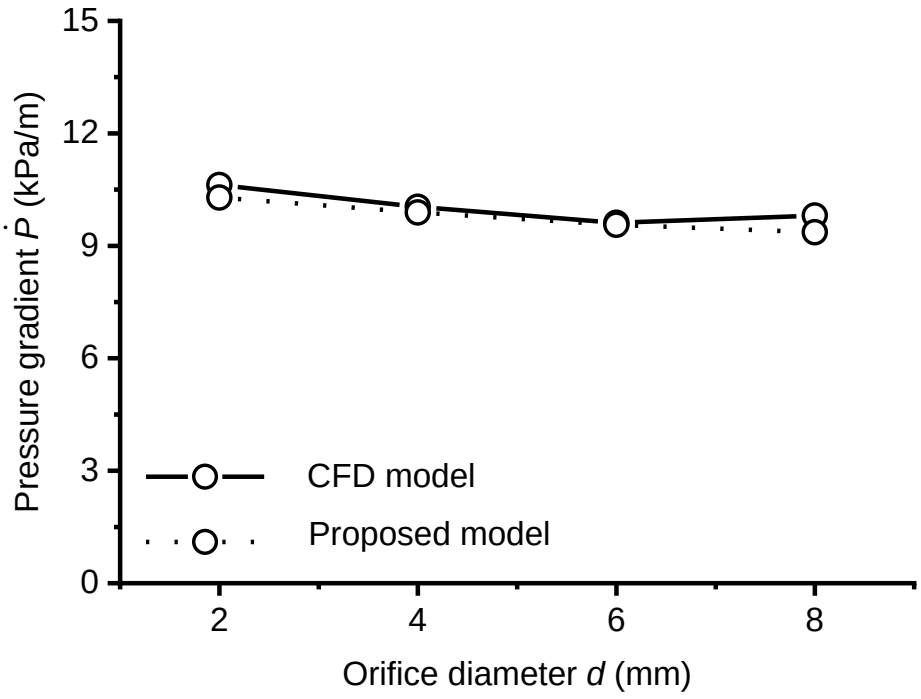

Figure 5-5. Validation of proposed model against CFD simulation results.

5.4. Numerical simulations

5.4.1 Scenarios

The numerical simulations were conducted on a vertical drain, similar to the model in Figure 5-1a. The drain measures 4,000 (Length) × 100 (Width) × 4 (Depth) mm. The lower inlet is flush with the groundwater table, and the upper outlet is connected to the vacuum pressure

supplier. The ambient atmospheric pressure, P_0, is 101.3 kPa (i.e., 1 atm). Orifices are aligned on the centreline of the surface of the vertical drain. The model assumes (i) the ambient pressure and the groundwater table are constant, (ii) the cross-sectional area of the drain remains unchanged, and (iii) no vaporisation occurs.

Four scenarios were designed to examine dewatering capacity of the vertical drain. These scenarios are given in Table 5-2. Scenario 1 involves one orifice and assesses the relationship between the size and location of the orifice. The orifice sits at the elevation of l = 0.5, 0.6, 0.7, …, 3.4 or 3.5 m. At each location, the orifice diameter d is progressively increased until no water is drawn. A no-draw occurs when the velocity of water is equal to or less than v_l = 0.001 m/s, or the air volume ratio is α = 99.99% or above, whichever occurs earlier. The inlet pressure P_0 = 101.3 kPa and outlet pressure P_{out} = 41.3 kPa are maintained when trialling the orifice diameter d. Scenario 2 also involves one orifice, which sits at the l = 2 m elevation. The inlet pressure is P_0 = 101.3 kPa; the outlet pressure is varied as P_{out} = 1.3, 2.3, 3.3, …, and 56.3 kPa. Under each pair of pressures, adjust the orifice size d until a no-draw occurs.

Scenario 3 examines the water volume discharged under a vacuum pressure. The vacuum pressure is P_v = 60 kPa, resulting from a 101.3 kPa inlet pressure and 41.3 kPa outlet pressure. This scenario involves one single orifice placed at one of five locations, i.e., l = 1, 1.5, 2, 2.5 and 3 m. At each location, adjust the orifice size, from d = 0.01 mm to 20 mm or a diameter yielding a no-draw, whichever occurs earlier. The diameter increment is 0.01 mm. On each orifice size, Scenario 3 determines the pressure distributions, air volume ratios, and velocity of water and air. Scenario 4 uses a lot of five orifices in the diameters of 0.15, 0.4, 0.3, 0.25 and 0.2 mm respectively.

Table 5-2. Simulation scenarios

Scenario	Orifice quantity	Orifice location *l* (m)	Orifice diameter *d* (mm)	Pressure at inlet P_0 (kPa)	Pressure at outlet P_{out} (kPa)
1	1	0.5, 0.6, 0.7, …, 3.5	—	101.3	41.3
2	1	2	—	101.3	1.3, 2.3, 3.3, …, 56.3
3	1	1, 1.5, 2, …, 3	0.01, 0.02, 0.03, …, 20.00 (up to)	101.3	41.3
4	5	1, 1.7, 2.3, 3, 3.4	0.15, 0.4, 0.3, 0.25, 0.2	101.3	31.3

The five orifices sit at 1, 1.7, 2.3, 3 and 3.4 m elevations respectively. The quantities, sizes and locations of the orifices were chosen to spread over the drainpipe and to represent varied sizes of orifices. A relatively higher vacuum pressure of 70 kPa was applied to this scenario. Upon flow equilibrium, Scenario 4 plots the pressures and air volume ratios by distance.

5.4.2 Simulation results

The results from Scenario 1 are given in Figure 5-6. Scenario 1 determines the maximum orifice diameter for the drain to lift water at P_v = 60 kPa vacuum pressure. The curve is a parabola (U-shaped) with the vertex at the 2.8 m location and the 6.8 mm orifice diameter. This means that the 60 kPa vacuum pressure can lift water if only the orifice is less than 6.8 mm. When the orifice is larger than 6.8 mm, a no-draw occurs depending on the location of the orifice. When the orifice sits higher than 2.8 m, the no-draw orifice size increases from 6.8 mm to 7.3 mm. When the orifice sits between 2.8 and 0.5 m, the no-draw

orifice size increases from 6.8 mm to 9.5 mm. The parabola relationship suggests that the closer the orifice is to the drain inlet, the larger the orifice is for the drainpipe to lift water. The simulations also suggested that an annular flow pattern occurs upon a no-draw.

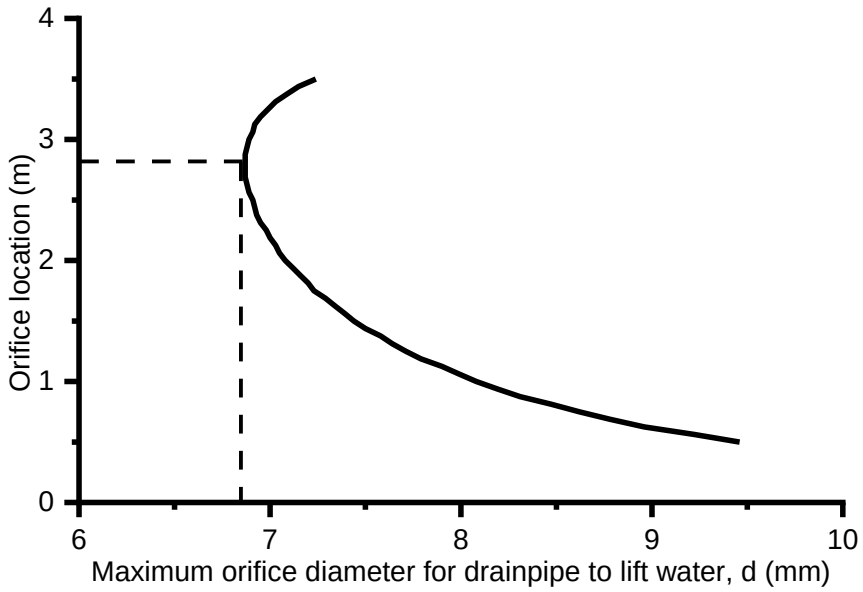

Figure 5-6. Relationship between orifice location and maximum orifice diameter for vertical drain to draw water under 60 kPa vacuum pressure.

Figure 5-7 shows the results from Scenario 2, i.e., the maximum diameter of orifice for the drain to lift water versus the applied vacuum pressure, while the orifice is located at 2 m elevation. The vacuum pressure curve shows that the maximum diameter increases with the applied vacuum pressure. When the vacuum pressure is 100 kPa, the maximum orifice diameter for the drain to lift water is as large as 8.95 mm. The orifice diameter decreases to 5.89 mm when the vacuum pressure reduces to 45 kPa. The orifice size to vacuum pressure ratio (i.e., the line gradient) is approximately 0.055 mm/kPa. Note that the trendline in Figure 5-7 should hold when changing the drain setting

including the drain cross-section and orifice location, but the orifice size for drainpipe to lift water may vary.

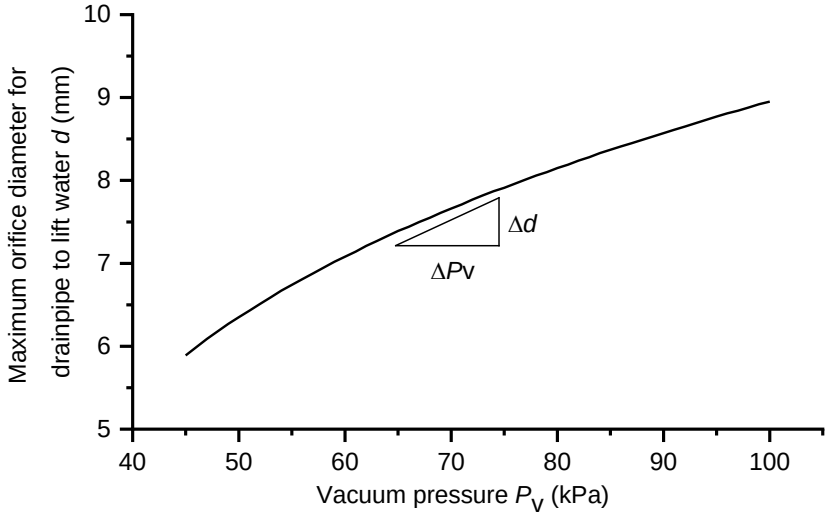

Figure 5-7. Relationship between applied vacuum pressure and maximum orifice diameter for vertical drain to draw water when orifice is at 2 m location.

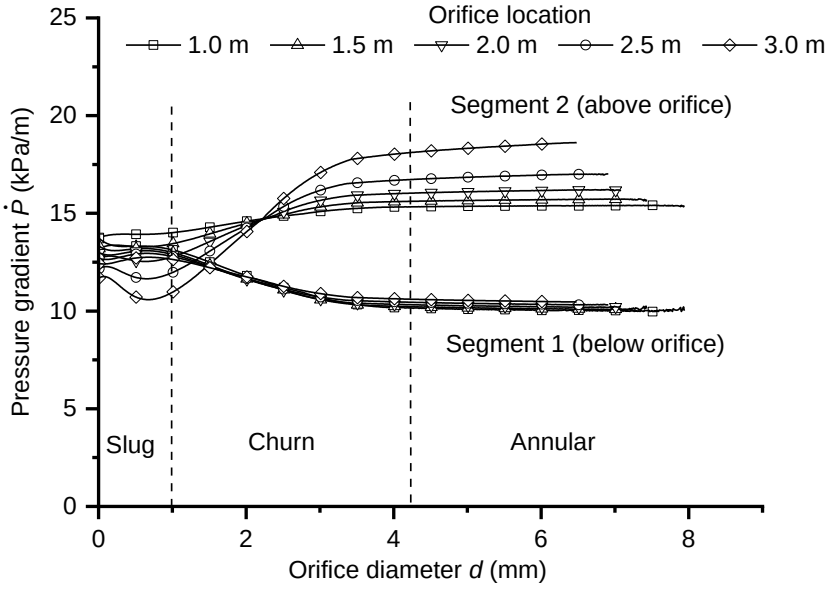

Figure 5-8. Relationship between orifice diameter and pressure gradient for single-orifice vacuum drain.

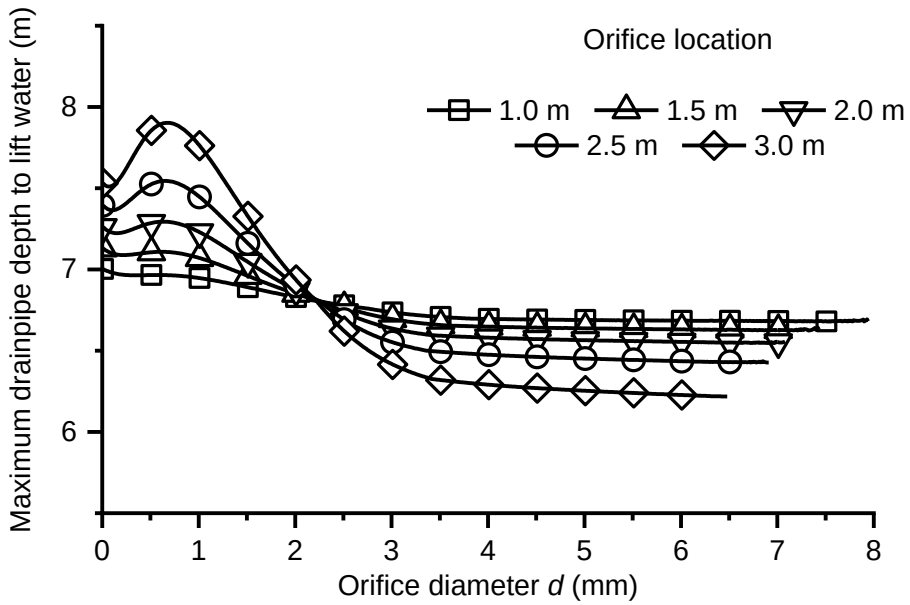

Figure 5-9. Maximum depth for drainpipe to lift water when varying location and size of orifice.

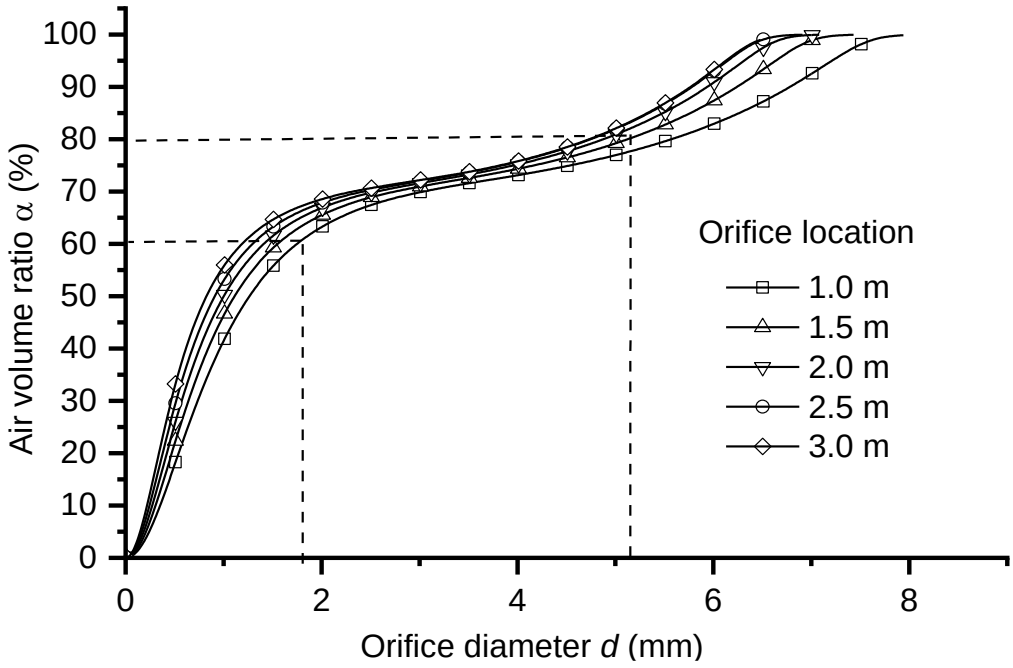

Figure 5-10. Relationship between air volume ratio and orifice diameter for vacuum drain with a single orifice.

The results from Scenario 3 are given in Figure 5-8 to Figure 5-11. Figure 5-8 shows the pressure gradient versus the orifice size when keeping the orifice location and vacuum pressure (of 60 kPa) unchanged. The pressure gradient equals the pressure difference over the distance and is segment specific. The orifice divides the drain into two segments, i.e., Segment 1 of below the orifice and Segment 2 of above.

Segment 1, consisting of water, has pressure gradients varied with the locations and diameters of the orifices. The pressure gradients are up to 13.7 kPa/m when the orifice diameter is as small as 0.65 mm. The gradients decrease with the orifice diameter of up to 3.5 mm and then sit at 10 kPa/m with the diameter until the drain fails to draw water.

The gradient range is narrow considering the varied orifice locations (of 1 to 3 m) and orifice diameters (0.01 to 8.5 mm). In particular, the orifice locations show marginal effects on the pressure gradients, where the orifice diameters remain the same. Note the pressure gradient values fall below the nominal pressure gradient of the drainpipe, i.e., 15 kPa/m (or 60 kPa per 4 m). This means the pressure gradient over the full length of the drain is uneven and Segment 2 acts a pressure gradient higher than Segment 1 does.

Segment 2, comprising a mix of air and water, shows noticeably different results from Segment 1's. First, the air–water mixture transports in one of the three flow patterns, i.e., slug, churn and annular, depending on the orifice diameter. By benchmarking the calculated mass flow rates against the flow pattern in Afshin and Swanand (2014), the mixture transports in a slug pattern when $0 < d < 1.9$ mm, a churn pattern when $1.9 < d < 4.2$ mm, and an annular

pattern when the orifice size is 4.2 mm to as large as 8 mm. No water is lifted for a larger orifice drainpipe.

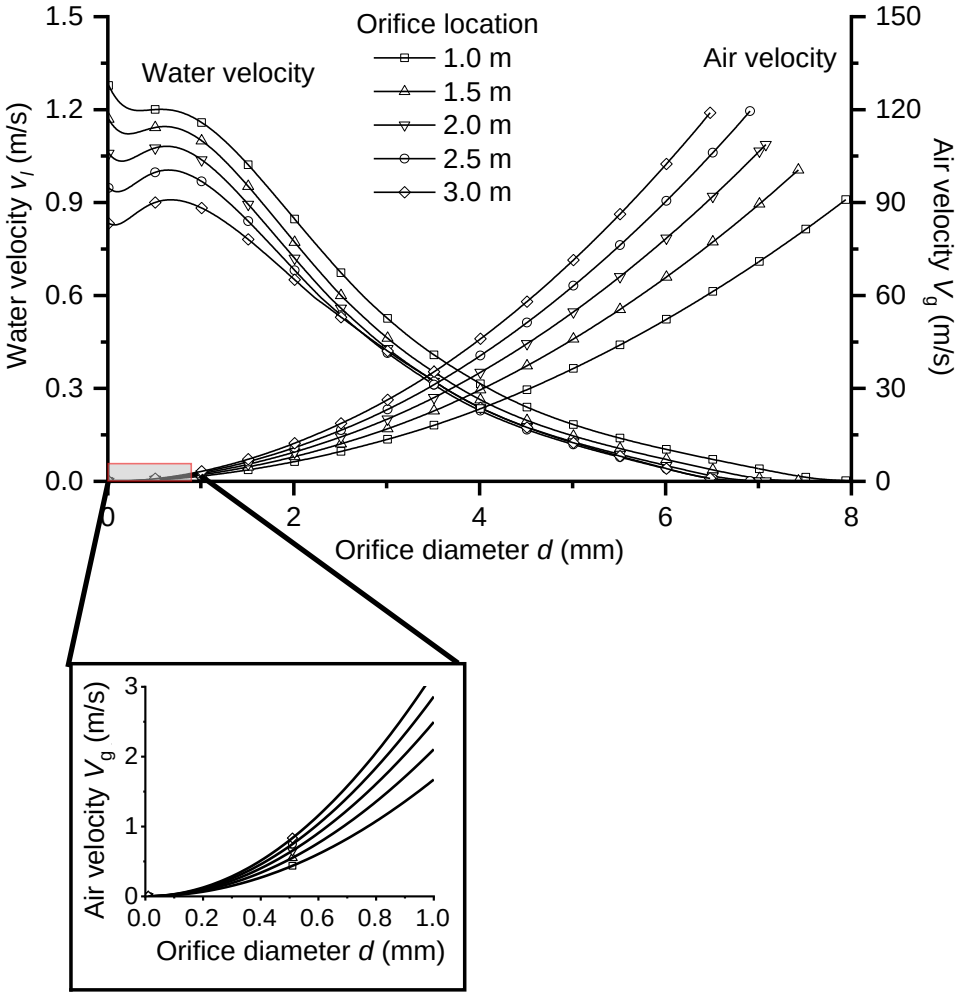

Figure 5-11. Relationships between air velocity, water velocity and orifice diameter for vacuum drain with a single orifice.

Second, Segment 2 shows pressure gradient profiles different from the counterparts of Segment 1. When the orifice is located at 1 m, the pressure gradients slowly increase with the orifice diameter and, when

the diameter is greater than 4 mm, flat out. Moving the orifice to the higher elevations, the pressure gradient profiles change. The pressure gradients initially decrease with the orifice diameters, turn at 0.65 mm diameter, and then increase with the orifice diameters. When the orifices are larger enough e.g., d > 4 mm, the pressure gradients reach constant values. The pressure gradients in Segment 2 on average fall on a wider and higher range than in Segment 1. The values, which are as high as 18 kPa/m, are higher than the maximum 13.7 kPa/m gradient in Segment 1 and the 15 kPa/m nominal gradient. The higher pressure gradients in Segment 2 suggest the drastic pressure drops caused by air. The pressure drops more noticeably when the air contents increase with the orifice size and the flow turns into churn or annular.

The pressure drop is also related to the orifice location. The pressure drops more noticeably when the orifice is closer to the outlet than to the inlet. For example, when the 7 mm orifice sits at the 3 m elevation, the pressure gradient in Segment 2 is 18.1 kPa/m. Moving the same size orifice down to the 1 m elevation, the pressure gradient is 15.30 kPa/m. The main reason is that more air is drawn from the orifice due to the greater pressure difference, resulting in a greater pressure drop. The pressure drop in essence is related to the air volume ratio present in the drainpipe and agrees to the findings from Scenario 1.

The maximum depth, l_c, for a confined drainpipe to lift water assesses the performance of dewatering systems. The lift depth under 1 atm is approximately 10.3 m if no air and orifice present. The lift depth decreases in the presence of orifice and can be determined from the pressure gradient in Figure 5-8. The lift depth is calculated as:

$$l_c = l_1 + \frac{P_{out} - P_1 - \Delta P_0 - \Delta P_1}{\dot{P}_1} \quad (5\text{-}15)$$

The lift depths for one-orifice drainpipe, 100 (Width) × 4 (Depth) mm, under 1 atm are shown in Figure 5-9. The maximum depth to lift water is 7.9 m, where one 0.65 mm orifice is present at 3 m. The lift capacity diminishes nonlinearly with the orifice size and flats out when the orifice is as large as 3 to 4 mm depending on the locations of the orifices. The lift depths eventually fall on 6.3 to 6.8 m depending on where the orifice sits. Interestingly all relationship curves coincide on the coordinate (2.2 mm, 6.8 m). This is also a turn point for the curve trendlines. That is, when the orifice is less than 2.2 mm, the lift capacity goes up with the orifice elevation, and vice versa when the orifice is larger than 2.2 mm. This means that the size and location of orifice interact each other when assessing the lift capacity. These observations agree with the finding in Qiu et al. (2007).

Figure 5-10 shows the air volume ratios in Segment 2 when varying the size and location of the orifice. The air volume ratio is positively related to the orifice diameter. The relationship follows a double logistic curve, showing two growth stages for the air volume ratio and, between the two stages, a phase with nearly zero growth. The growth stages align with the development of flow patterns in Figure 5-8, where the maximum growth rate occurs in the slug flow regime as air continues to enter the pipe. This is followed by the flat-out of the growth rate, indicating the churn flow regime, where the large air bubbles turn into a distinct air phase. The growth rate of the air volume ratio reaches the second peak where a continuous air phase is formed, indicating the annular flow regime. The drain fails to draw water when the orifice diameter is as large as 8 mm. In contrast, the orifice location shows less effects on the air volume ratio than the orifice diameter does.

The velocities of air and water in Segment 2 of the drain are given in Figure 5-11. The air and water move in varied speeds depending on the locations and sizes of the orifices. The water departs at a speed of ranging from 0.8 to 12.8 m/s when involving a 0.01 mm orifice. The speeds go down and up reaching the peak speeds when the orifice diameter increases to 0.6 mm. With the orifice size further increasing, the speeds of water gradually decrease until the drain fails to draw water. In the meantime, the air phase travels faster when the orifice size increases providing the orifice is fixed at a location. With the orifice moving closer to the outlet, the air stream moves drastically faster at a speed as high as 150 m/s. Although the air stream moves as high as 100 times faster than the water stream in the drainpipe, the air does not move as fast as the water when the orifice is less than 0.6 mm in size.

The results from Scenario 4 are given in Figure 5-12. This figure presents the vacuum pressures (Figure 5-12a) and air volume ratios (Figure 5-12b) determined over the five-orifice drainpipe. In Figure 5-12a, the vacuum pressures (in relation to a 101.3 kPa atm) drop from 0 kPa at the lower inlet to 70 kPa on the upper outlet, which agrees to the observation by Qiu et al. (2007). The vacuum pressure profile is stepped at each of the orifice locations, therefore showing the instantaneous pressure drops due to the entering of air. Interestingly the drops are not proportional with the orifice diameters or locations. For example, the maximum pressure drop (10 kPa) occurs at the second smallest orifice (0.2 mm diameter) that is at 3.4 m. The pressure drops verify the results from Scenario 1. That is, the closer the orifice is to the vacuum outlet, the higher the pressure difference at the orifice will be, and hence, the higher the pressure drop is. The stepped slopes represent the pressure gradients. The gradients increase with the elevation and upon approaching the outlet decrease.

One reason for the varied pressure gradients is that the decrease in the air volume ratio decreases the gravitational pressure gradient. The observation agrees with the results in Qiu et al. (2007) that the vacuum pressure distribution is not uniform. The trendlines in the vicinity of the outlet suggest that the frictional component governs the pressure drop when the air volume dominates the flow. The increase in the frictional component may potentially offset the reduction in the gravitational component.

A similarly stepped profile occurs to the air volume ratios as in Figure 5-12b. The air volume accumulates through the steps, reaching a 0.75 air volume ratio at the outlet. The relationships agree to the results from Scenario 1 and suggest that air enters the drainpipe more drastically closer to the inlet, and vice versa. One may explain the relationship using the results in Figure 5-10, where the air volume ratio increases in two stages in terms of the orifice size.

5.4.3 Engineering applications

This proposed model is applicable to the vacuum dewatering practice. In vacuum dewatering, a vertical drain is installed inside the soil with its upper outlet located above the ground surface and connected to the vacuum pump. The lower inlet is submerged below the groundwater table, replicating Segment 1 in Figure 5-1a. The top portion of the pipe is adjacent to the unsaturated zone where air is present. As air can permeate through the fabrics of vertical drain, forming air–water mixed flow as in Segments 2 to *n*. Therefore, the model in Figure 5-1 can represent dewatering applications.

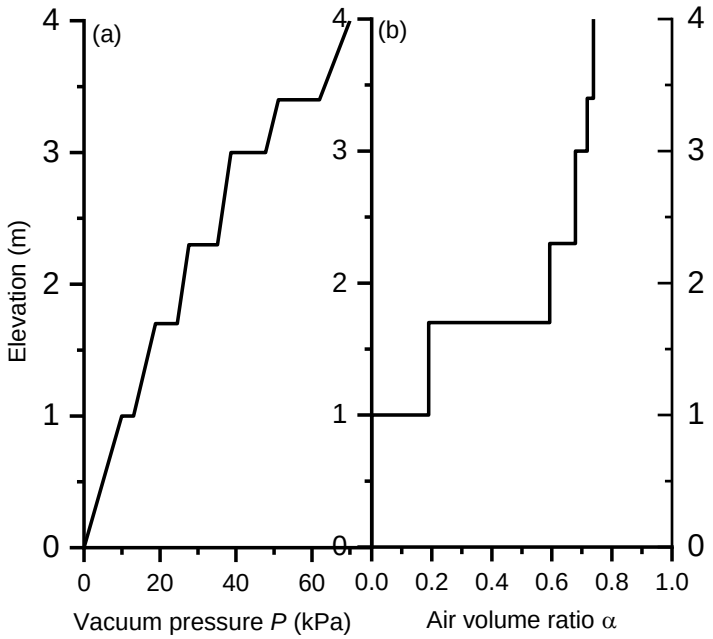

Figure 5-12. Profiles of (a) vacuum pressure; and (b) air volume ratio of drainpipe involving multiple orifices.

The solutions to the four example problems give some interesting results. First the vacuum pressure inside the drainpipe is non-linear. The upper portion, which is near the ground surface, shows a greater pressure drop than the lower portion. The fluid follows a slug flow pattern and comprises a chain of large bubbles which likely impact on steady flow. As the vacuum pressure in practice is often less than 1 atm, the lift depth is less than 10 m. The presence of orifices tents to further reduce the lift depth. This means, less water will be lifted in unsaturated zones than in the saturated zones.

5.5. Conclusion

This study modelled the orifice induced air–water flow in vertical drainpipes. The proposed model took account of the compressibility of air, drift flux velocity in confined pipelines, and Bernoulli's energy principle. This study presented the numerical algorithms to solve the

proposed model and validated the solutions. The model was applied to the example problems and arrived at the following results:

- The vacuum pressures distribute nonlinearly inside the drainpipe. The nonlinear distributions are related to the size and location of orifices. The vacuum pressure drops more noticeable in unsaturated zones.
- Under 1 atm vacuum pressure, the drainpipe lift depth falls on 6.8 to 7.5 m for a one-orifice drainpipe provided orifice diameter is less than 2.2 mm and 6.3 to 6.8 m if the diameter is 2.2 to up to 7 mm. One >7 mm orifice stops the drainpipe from lifting water.
- Pipe pressures drop more noticeably when lifting air–water mixture than lifting water. Drawing up air–water flux in unsaturated zones reduces drainpipe lift capacity.
- The air volume ratio in the drainpipe increases with the orifice diameter. The relationship follows a double logistic curve. The air volume ratio increases relatively noticeably when the orifice size falls in the ranges of from 0 to 1.8 mm and from 5.2 to 6.5 mm.

5.6. Notations

Roman

C	Discharge coefficient
D	Drainpipe diameter
d	Orifice diameter
f	Friction factor
g	Gravity acceleration
L	Drainpipe length
l	Orifice location
M	Molar mass

m	Mass flow rate
P	Pressure
$\dot{P}$	Pressure gradient
R	Ideal gas constant
R_e	Reynold's number
r_c	Critical pressure ratio
T	Temperature
V	Volume
v	Velocity
z	Elevation

Greek

α	Air volume ratio
γ	Specific heat ratio
ε	Pipe roughness height
μ	Dynamic viscosity
ρ	Density
σ	Surface tension
Φ	Two-phase correlation factor

Subscripts

0	Initial value
$frict$	Frictional
g	Gas or air
gm	Drift flux
$grav$	Gravitational
i	The i^{th} orifice or segment
l	Liquid or water
O	Orifice
out	Outlet
v	Vacuum

Chapter 6 Conclusions

6.1. Research contributions

The thesis comprised four theoretical research articles. These articles systemically studied the drain aided consolidation of partially saturated soil.

A novel finite strain two-dimensional unsaturated consolidation model was proposed in Chapter 2 (paper 1). The model utilised the Lagrangian and Convective coordinate system and was solved via the in-house finite difference code. The model enabled non-linear soil parameters including soil Water characteristic curve, shrinkage curve, and permeability curve. The proposed governing equation was written in a conventional advection and diffusion equation form, enabling adaption with different numerical solver.

A parametric study was conducted in Chapter 2 with a focus on the initial wet degree of layer on consolidation. The modelling result suggested that the initial soil saturation degree affects the consolidation curve. The higher the initial degree of saturation, the greater the settlement is, and vice versa. The air tends to dissipate faster than the water in the same soil layer.

Using the consolidation model in Chapter 2, Chapter 3 studied the effect of the consolidation method on dewatering and solute transport efficiency. A solute transport model was coupled with the proposed consolidation model, simulating the contaminate transport during the

unsaturated soil consolidation. The coupled equation was solved via the unconditional stable Alternative Direction Finite Different Time Domain method. The method enhanced the computational time compared to the conventional explicit method.

The proposed governing equations and numerical algorithm were verified against the laboratory test. A numerical study was carried out to examine the consolidation and solute discharge efficiency for different consolidation method and contaminate types. The results suggested that vacuum consolidation approach has a greater dewatering efficiency compared to the conventional preloading consolidation. The consolidation accelerated the transport of reactive chemicals but showed limited effects on transport of non-reactive chemicals. The solute dispersion process contributed to the contaminate discharge; however, became less noticeable when soil became unsaturated. The sorption process reduced the contaminate clean-up rate.

Chapter 4 proposed a numerical model governing the vacuum air booster consolidation. The model utilised the Lagrangian-Convective finite strain framework and solved via the ADI-FDTD method. The model considered the soil unsaturation induced by the pressurised air system by determining the soil fracture state in each iteration. The model was verified against the field test.

Chapter 5 studied the drainage efficiency of the vertical drain when air was present in soil. A preliminary modelling framework was proposed. The framework comprised empirical void fraction and two-phase pressure drop correlation and determined the pressure gradient of the drain well by inputting the applied vacuum pressure and soil void ratio. It should be noted that the preliminary model considered the soil

medium as the orifices along the drain. A detailed model is required to accurately estimate the pressure drop.

A preliminary study was conducted by the proposed model. The result stated that the nonlinear pressure distributions occurred in the drainpipe, and pressure dropped more noticeably in the presence of air. More water was discharged when the orifice was located closer to the lower end than to the upper end. Under one standard atmosphere vacuum pressure the lift depth was approximately 6.3 to 7.5 m depending on the orifice size.

In summary, this research provides a comprehensive modelling approaches for drain-aided consolidation of unsaturated soil. Models were developed using finite deformation approach and enables accurate prediction of the consolidation time and settlement. With guidelines proposed in this thesis, engineers or researchers can:

- Evaluate the unsaturated soil consolidation behaviour,
- Evaluate the saturated and unsaturated soil solute transport,
- Assess the drainage efficiency when vertical drains are utilised for unsaturated soil improvement, and
- Estimate the consolidation time and settlement when vacuum-air-booster consolidation method is adopted.

6.2. Scope of future work

The recommendation for future work is related to soil consolidation test and drain well efficiency assessment.

The proposed large-strain unsaturated soil consolidation model has been verified against the laboratory tests and analytical models. The tests however did not consider some important soil properties, such as the non-linear soil water characteristic curve and shrinkage curve, as the existing laboratory test did not provide the detailed soil parameters. A mesoscale laboratory experiment with vertical drains was also missed in existing documents. To verify the model accuracy, and hence apply the model in estimating the consolidation settlement/time in situ, a mesoscale laboratory experiment utilising the vertical drain with SWCC, shrinkage, permeability and compression curves measurement is warranted.

The developed unsaturated soil consolidation models can simulate either saturated or unsaturated soil consolidation individually. However, the model is unable to smoothly transition from a fully saturated state to an unsaturated state because it is governed by the SWCC, where soil suction and air entry values are used to determine the soil saturation degree. Soils become unsaturated only when the soil suction exceeds the air entry value. In cases where vacuum consolidation or preloading consolidation is employed, quantifying soil suction becomes challenging. Further research is needed to facilitate a seamless transition from saturated to partially saturated states, thus improving the modelling of in-situ soil consolidation.

For the vacuum air booster consolidation, it is clear the soil unsaturation is present due to the pressurised air; however,

unsaturated soil parameters were missed in some field and laboratory tests. A detailed mesoscale test is required to verify the proposed model.

The two-phase flow model of the drain well in its current form is considered as a preliminary model. To apply the model in practice, further enhancement by detailing the orifice layout, i.e., >100,000 orifices with orifice diameter <20 μm, is required. This can be achieved by upscaling the model automation and computational efficiency. A field or mesoscale laboratory test is also warranted.

References

Afshin, G., and Swanand, B., 2014. Flow Patterns, Void Fraction and Pressure Drop in Gas-Liquid Two Phase Flow at Different Pipe Orientations. Front. Prog. Multiph. Flow I, L. Cheng, ed., Springer International Publishing, 157–212. https://doi.org/10.1007/978-3-319-04358-6.

Afshin J, G., and Swanand M, B., 2014. *Frontiers and Progress in Multiphase Flow I*. Front. Prog. Multiph. Flow I, (L. Cheng, ed.), Springer International Publishing. https://doi.org/10.1007/978-3-319-04358-6.

Alizadehdakhel, A., Rahimi, M., Sanjari, J., and Alsairafi, A. A., 2009. CFD and artificial neural network modeling of two-phase flow pressure drop. Int. Commun. Heat Mass Transf., 36(8), 850–856. https://doi.org/10.1016/j.icheatmasstransfer.2009.05.005.

Alonso, E. E., Gens, A., and Josa, A., 1990. A constitutive model for partially saturated soils. Geotechnique, 40(3), 405–430.

Alshawabkeh, A. N., Rahbar, N., and Sheahan, T., 2005. A model for contaminant mass flux in capped sediment under consolidation. J. Contam. Hydrol., 78(3), 147–165. https://doi.org/10.1016/j.jconhyd.2005.05.003.

Amaziane, B., Jurak, M., and Žgaljić Keko, A., 2010. Modeling and numerical simulations of immiscible compressible two-phase flow in porous media by the concept of global pressure. Transp. porous

media, Springer, 84(1), 133–152.

Anda, R., Fu, H., Wang, J., Lei, H., Hu, X., Ye, Q., Cai, Y., and Xie, Z., 2020. Effects of pressurizing timing on air booster vacuum consolidation of dredged slurry. Geotext. Geomembranes, Elsevier, 48(4), 491–503. https://doi.org/10.1016/j.geotexmem.2020.02.007.

Ansys Inc., 2020. ANSYS FLUENT Theory Guide. ANSYS Inc., USA, Release 20(R1), 814.

Azzouz, A. S., Krizek, R. J., and Corotis, R. B., 1976. Regression Analysis of Soil Compressibility. Soils Found., 16(2), 19–29. https://doi.org/https://doi.org/10.3208/sandf1972.16.2_19.

Ba-Te, Zhang, L., and Fredlund, D. G., 2005. A General Air-phase Permeability Function for Airflow through Unsaturated Soils. Slopes Retaining Struct. under Seism. Static Cond., 1–15. https://doi.org/10.1061/40787(166)29.

Barron, R. A., 1948. Consolidation of fine-grained soils by drain wells. Trans. Am. Soc. Civ. Eng., 113(1), 718–742.

Bear, J., 1972. Dynamics of fluids in porous media. Eisevier, New York, 1–783.

Bhagwat, S. M., 2015. Experimental Measurements and Modelling of Void Fraction and Pressure Drop in Upward and Downward Inclined Non-Boling Gas-Liquid Two-Phase Flow. Oklahoma State University.

Bilardi, S., Ielo, D., and Moraci, N., 2020. Predicting the Saturated

Hydraulic Conductivity of Clayey Soils and Clayey or Silty Sands. Geosciences, MDPI, 10(10), 393.

Brooks, R. H., and Corey, A. T., 1964. Properties of Porous Media Affecting Fluid Flow. J. Irrig. Drain. Div., 92(2), 61–88. https://doi.org/10.1061/jrcea4.0000425.

Cai, Y., Xie, Z., Wang, J., Wang, P., and Geng, X., 2019. New approach of vacuum preloading with booster prefabricated vertical drains (PVDs) to improve deep marine clay strata. Can. Geotech. J., 56(12), 2017. https://doi.org/10.1139/cgj-2019-0250.

Chen, Z., Ni, P., Zhu, X., Chen, D., and Mei, G., 2021. Consolidation of unsaturated soil by vertical drain considering smear and well resistance. Geosynth. Int., 29(3), 1–32. https://doi.org/10.1680/jgein.21.00010.

Chen, Z. X., 1988. Some Invariant Solutions to Two-Phase Fluid Displacement Problems Including Capillary Effect. SPE Reserv. Eng., Society of Petroleum Engineers, 3(02), 691–700. https://doi.org/10.2118/14874-PA.

Cheng, L., Ribatski, G., and Thome, J. R., 2008. Two-Phase Flow Patterns and Flow-Pattern Maps: Fundamentals and Applications. Appl. Mech. Rev., 61(5). https://doi.org/10.1115/1.2955990.

Conte, E., 2004. Consolidation analysis for unsaturated soils. Can. Geotech. J., 41(4), 599–612. https://doi.org/10.1139/T04-017.

Dakshanamurthy, V., and Fredlund, D. G., 1980a. Moisture and air flow in an unsaturated soil. Expans. Soils, ASCE, 514–532.

Dakshanamurthy, V., and Fredlund, D. G., 1980b. Moisture and air flow in an unsaturated soil. Proc. fourth Int. Conf. Expans. soils, , vol. 1, ASCE, 514–532.

Deng, A., and Wang, C., 2014. A finite difference model for electric field derived solute transport. Proc. 7th Int. Congr. Environ. Geotech., (Esrig 1967), 597–604.

Douglas, J., and Rachford, H. H., 1956. On the Numerical Solution of Heat Conduction Problems in Two and Three Space Variables. Trans. Am. Math. Soc., 82(2), 421. https://doi.org/10.2307/1993056.

Elger, D. F., Crowe, C. T., and Roberson, J. A., 2016. *Engineering Fluid Mechanics*. Wiley.

Feng, S., and Zhou, J., 2022. Field instrumentation and evaluation of ground treatment by combined air-booster and straight-line vacuum preloading without sand. Mar. Georesources Geotechnol., Taylor & Francis, 40(3), 267–280. https://doi.org/10.1080/1064119X.2021.1886204.

Fox, P. J., 2007a. Coupled Large Strain Consolidation and Solute Transport. I: Model Development. J. Geotech. Geoenvironmental Eng., 133(1), 3–15. https://doi.org/10.1061/(asce)1090-0241(2007)133:1(3).

Fox, P. J., 2007b. Coupled Large Strain Consolidation and Solute Transport. II: Model Verification and Simulation Results. J. Geotech. Geoenvironmental Eng., 133(1), 3–15. https://doi.org/10.1061/(asce)1090-0241(2007)133:1(3).

Fox, P. J., and Berles, J. D., 1997. CS2: A piecewise-linear model for large strain consolidation. Int. J. Numer. Anal. Methods Geomech., 21(7), 453–475. https://doi.org/10.1002/(SICI)1096-9853(199707)21:7<453::AID-NAG887>3.0.CO;2-B.

Fox, P. J., and Lee, J., 2008. Model for Consolidation-Induced Solute Transport with Nonlinear and Nonequilibrium Sorption. Int. J. Geomech., 8(3), 188–198. https://doi.org/10.1061/(asce)1532-3641(2008)8:3(188).

Fredlund, D. G., 1979. Appropriate concepts and technology for unsaturated soils. Can. Geotech. J., 16(1), 121–139. https://doi.org/10.1139/t79-011.

Fredlund, D. G., and Hasan, J. U., 1979a. One-dimensional consolidation theory: unsaturated soils. Can. Geotech. J., 16(3), 521–531. https://doi.org/10.1139/t79-058.

Fredlund, D. G., and Hasan, J. U., 1979b. One-dimensional consolidation theory: unsaturated soils. Can. Geotech. J., 16, 521–531. https://doi.org/10.1139/t79-058.

Fredlund, D. G., and Morgenstern, N. R., 1976. Constitutive Relations for Volume Change in Unsaturated Soils. Can. Geotech. J., 13(3), 261–276. https://doi.org/10.1139/t76-029.

Fredlund, D. G., and Rahardjo, H., 1993. *Soil Mechanics for Unsaturated Soils*. John Wiley & Sons, Inc, Hoboken, New Jersey.

Fredlund, D. G., Rahardjo, H., and Fredlund, M. D., 2012. *Unsaturated soil mechanics in engineering practice*. Unsaturated soil Mech. Eng. Pract., John Wiley & Sons, Inc, Hoboken, New Jersey.

Fredlund, D. G., and Xing, A., 1994. Equations for the soil-water characteristic curve. Can. Geotech. J., NRC Research Press Ottawa, Canada, 31(4), 521–532.

Fredlund, D. G., and Zhang, F., 2013. Combination of shrinkage curve and soil-water characteristic curves for soils that undergo volume change as soil suction is increased. 18th Int. Conf. Soil Mech. Geotech. Eng. Challenges Innov. Geotech. ICSMGE 2013, 2, 1109–1112.

Fredlund, M. D., Wilson, G. W., and Fredlund, D. G., 2002. Representation and estimation of the shrinkage curve. UNSAT 2002, Proc. Third Int. Conf. Unsaturated Soils, 10–13.

Fujimoto, T., and Usami, M., 1984. Rarefied gas flow through a circular orifice and short tubes.

Gao, Y. Bin, and Zhang, Z., 2020. Vertical compression of soft clay within PVD-improved zone under vacuum loading: Theoretical and practical study. Geotext. Geomembranes, Elsevier, 48(3), 306–314. https://doi.org/10.1016/j.geotexmem.2019.12.003.

Geng, X., and Yu, H.-S., 2017. A large-strain radial consolidation theory for soft clays improved by vertical drains. Géotechnique, 67(11), 1020–1028. https://doi.org/10.1680/jgeot.15.t.013.

Ghajar, A. J., 2020. *Two-Phase Gas-Liquid Flow in Pipes with Different Orientations*. Stillwater, OK, USA.

Gibson, R. E., Schiffman, R. L., and Cargill, K. W., 1981. The theory of one-dimensional consolidation of saturated clays. II. Finite nonlinear consolidation of thick homogeneous layers. Can.

Geotech. J., 18(2), 280–293. https://doi.org/10.1139/t81-030.

Hamad, F. A., Faraji, F., Santim, C. G. S., Basha, N., and Ali, Z., 2017. Investigation of pressure drop in horizontal pipes with different diameters. Int. J. Multiph. Flow, Elsevier Ltd, 91, 120–129. https://doi.org/10.1016/j.ijmultiphaseflow.2017.01.007.

Hanafizadeh, P., Ghanbarzadeh, S., and Saidi, M. H., 2011. Visual technique for detection of gas–liquid two-phase flow regime in the airlift pump. J. Pet. Sci. Eng., 75(3), 327–335. https://doi.org/https://doi.org/10.1016/j.petrol.2010.11.028.

Ho, L., and Fatahi, B., 2015a. Analytical solution for the two-dimensional plane strain consolidation of an unsaturated soil stratum subjected to time-dependent loading. Comput. Geotech., Elsevier Ltd, 67, 1–16. https://doi.org/10.1016/j.compgeo.2015.02.011.

Ho, L., and Fatahi, B., 2015b. Analytical solution for the two-dimensional plane strain consolidation of an unsaturated soil stratum subjected to time-dependent loading. Comput. Geotech., Elsevier Ltd, 67, 1–16. https://doi.org/10.1016/j.compgeo.2015.02.011.

Ho, L., Fatahi, B., and Khabbaz, H., 2015. A closed form analytical solution for two-dimensional plane strain consolidation of unsaturated soil stratum. Int. J. Numer. Anal. Methods Geomech., 39, 1665–1692. https://doi.org/10.1002/nag.2369.

Ho, L., Fatahi, B., and Khabbaz, H., 2016a. Analytical solution to axisymmetric consolidation in unsaturated soils with linearly depth-

dependent initial conditions. Comput. Geotech., Elsevier Ltd, 74, 102–121. https://doi.org/10.1016/j.compgeo.2015.12.019.

Ho, L., Fatahi, B., and Khabbaz, H., 2016b. Analytical solution to axisymmetric consolidation in unsaturated soils with linearly depth-dependent initial conditions. Comput. Geotech., Elsevier Ltd, 74, 102–121. https://doi.org/10.1016/j.compgeo.2015.12.019.

Hoffman, J. D., and Frankel, S., 2018. *Numerical methods for engineers and scientists*. CRC press.

Hu, X., Zhang, W., Fu, H., Wang, J., and Ni, J., 2021. Clogging effect of prefabricated horizontal drains in dredged soil by air booster vacuum consolidation. Geotext. Geomembranes, Elsevier Ltd, 49(6), 1529–1538. https://doi.org/10.1016/j.geotexmem.2021.07.002.

Hu, Y.-Y., Zhou, W.-H., and Cai, Y.-Q., 2014. Large-strain elastic viscoplastic consolidation analysis of very soft clay layers with vertical drains under preloading. Can. Geotech. J., 51, 144–157. https://doi.org/10.1139/cgj-2014-0383.

Huang, M., and Zhao, M., 2021. Semi-analytical solutions for two-dimensional plane strain consolidation of layered unsaturated soil. Comput. Geotech., Elsevier, 129, 103886.

Huangfu, Z., and Deng, A., 2023. Large strain consolidation of unsaturated soil: Model formulation and numerical analysis. Int. J. Geomech., 23(9), 1–15. https://doi.org/10.1061/IJGNAI.GMENG-7120.

Ide, H., and Matsumura, H., 1990. Frictional pressure drops of two-

phase gas-liquid flow in rectangular channels. Exp. Therm. Fluid Sci., 3(4), 362–372. https://doi.org/10.1016/0894-1777(90)90034-5.

Indraratna, B., Bamunawita, C., and Khabbaz, H., 2004. Numerical modeling of vacuum preloading and field applications. Can. Geotech. J., NRC Research Press, 41(6), 1098–1110. https://doi.org/10.1139/t04-054.

Indraratna, B., Rujikiatkamjorn, C., Ameratunga, J., and Boyle, P., 2011. Performance and prediction of vacuum combined surcharge consolidation at port of brisbane. J. Geotech. Geoenvironmental Eng., 137(11), 1009–1018. https://doi.org/10.1061/(ASCE)GT.1943-5606.0000519.

Ishii, M., 1977. *One-dimensional drift-flux model and constitutive equations for relative motion between phases in various two-phase flow regimes*. Argonne National Lab., Ill.(USA).

Jiang, L., Qin, A., Li, L., Mei, G., and Li, T., 2022. Coupled consolidation via vertical drains in unsaturated soils induced by time-varying loading based on continuous permeable boundary. Geotext. Geomembranes, 50(3), 383–392. https://doi.org/https://doi.org/10.1016/j.geotexmem.2021.11.010.

Ju Lee, H., and Yong Lee, S., 2001. Pressure drop correlations for two-phase flow within horizontal rectangular channels with small heights. Int. J. Multiph. Flow, 27(5), 783–796. https://doi.org/10.1016/S0301-9322(00)00050-1.

Khalili, N., Habte, M. A., and Zargarbashi, S., 2008. A fully coupled flow deformation model for cyclic analysis of unsaturated soils

including hydraulic and mechanical hystereses. Comput. Geotech., Elsevier, 35(6), 872–889.

Kiran, R., Ahmed, R., and Salehi, S., 2020. Experiments and CFD modelling for two phase flow in a vertical annulus. Chem. Eng. Res. Des., Institution of Chemical Engineers, 153, 201–211. https://doi.org/10.1016/j.cherd.2019.10.012.

Kjellman, W., 1952. Consolidation of clayey soils by atmospheric pressure. Proc. Conf. Soil Stab., Massachusetts Institute of Technology, USA, 258–263.

Lambe, W., and Whitman, R., 1979. *Soil Mechanics, SI Version*. John Wiley & Sons, Inc.

Lee, J., and Fox, P. J., 2009. Investigation of Consolidation-Induced Solute Transport. II: Experimental and Numerical Results. J. Geotech. Geoenvironmental Eng., 135(9), 1239–1253. https://doi.org/10.1061/(asce)gt.1943-5606.0000048.

Leverett, M. C., 1941. Capillary Behavior in Porous Solids. Trans. AIME, Society of Petroleum Engineers, 142(01), 152–169. https://doi.org/10.2118/941152-G.

Lewis, T. W., Pivonka, P., and Smith, D. W., 2009. Theoretical investigation of the effects of consolidation on contaminant transport through clay barriers T. Int. J. Numer. Anal. Methods Geomech., 33, 95–116. https://doi.org/10.1002/nag.708.

Li, M., Tang, Y. C., Li, J. J., and Meng, P. P., 2013. A Two-Phase Hydrodynamic Model for Transport Pipelines in Vacuum Sewer Systems. Appl. Mech. Mater., Trans Tech Publ, 508–512.

Li, S., and Liu, Y., 2006. Application of fractal models to water and solute transport in unsaturated soils. Adv. Unsaturated Soil, Seepage, Environ. Geotech., 195–202.

Liu, Y., Zheng, J., Ph, D., You, L., Ph, D., Asce, A. M., Lu, J., Cui, L., Ph, D., Yang, W., Huang, Z., and Ph, D., 2022. An Analytical Solution for 2D Plane Strain Consolidation in Unsaturated Soils with Lateral and Vertical Semipermeable Drainage Boundaries under Time-Dependent Loading. 22(12), 1–13. https://doi.org/10.1061/(ASCE)GM.1943-5622.0002508.

Lloret, A., and Alonso, E. E., 1980. Consolidation of unsaturated soils including swelling and collapse behaviour. Géotechnique, Thomas Telford Ltd, 30(4), 449–477.

Lockhart, R. ., and Martinelli, R. ., 1949. Proposed Correlation of Data for Isothermal Two-Phase, Two-Component Flow in Pipes. Chem. Eng. Prog., 45(1), 38–48.

Loroy, J. J. C., Soga, K., Savvidou, C., and Britto, A. M., 1996. Finite element analysis of consolidation and contaminant transport in porous media. Proc. 2nd Int. Congr. Environ. Geotech., 263–268.

Lote, D. A., Vinod, V., and Patwardhan, A. W., 2018. Computational Fluid Dynamics Simulations of the Air-Water Two-Phase Vertically Upward Bubbly Flow in Pipes. Ind. Eng. Chem. Res., 57(31), 10609–10627. https://doi.org/10.1021/acs.iecr.8b01579.

Lu, C., Kong, R., Qiao, S., Larimer, J., Kim, S., Bajorek, S., Tien, K., and Hoxie, C., 2018. Frictional pressure drop analysis for horizontal and vertical air-water two-phase flows in different pipe

sizes. Nucl. Eng. Des., Elsevier, 332(September 2017), 147–161. https://doi.org/10.1016/j.nucengdes.2018.03.036.

Lu, M., and Sun, J., 2022. Analytical model for consolidation of soft ground improved by PVDs with air-boosted system. Comput. Geotech., Elsevier Ltd, 151(August), 104968. https://doi.org/10.1016/j.compgeo.2022.104968.

McWhorter, D. B., and Sunada, D. K., 1990. Exact integral solutions for two-phase flow. Water Resour. Res., 26(3), 399–413. https://doi.org/10.1029/WR026i003p00399.

Micic, S., Shang, J. Q., Lo, K. Y., Lee, Y. N., and Lee, S. W., 2001. Electrokinetic strengthening of a marine sediment using intermittent current. Can. Geotech. J., NRC Research Press, 38(2), 287–302. https://doi.org/10.1139/t00-098.

Mishima, K., and Ishii, M., 1984. Flow regime transition criteria for upward two-phase flow in vertical tube. Int. J. Heat Mass Transf., 27(5), 723–737.

Montoya, G., Sanyal, J., and Braun, M., 2019. Assessment, implementation, validation, and verification of interfacial closures in multiphase flows for the CFD codes fluent and CFX. 18th Int. Top. Meet. Nucl. React. Therm. Hydraul. NURETH 2019, 1(4), 3014–3029.

Moreno Quibén, J., and Thome, J. R., 2005. Experimental and analytical study of two-phase pressure drops during evaporation in horizontal tubes. Fac. des Sci. Tech. l'ingénieur STI, Université Pierre et Marie Curie, Ph.D., 159.

Müller-Steinhagen, H., and Heck, K., 1986. A simple friction pressure drop correlation for two-phase flow in pipes. Chem. Eng. Process. Process Intensif., 20(6), 297–308. https://doi.org/https://doi.org/10.1016/0255-2701(86)80008-3.

Noye, B. J., and Tan, H. H., 1989. Finite difference methods for solving the two-dimensional advection-diffusion equation. Int. J. Numer. Methods Fluids, Wiley, 9(1), 75–98. https://doi.org/10.1002/fld.1650090107.

Pedroso, D. M., and Farias, M. M., 2011. Extended Barcelona Basic Model for unsaturated soils under cyclic loadings. Comput. Geotech., 38(5), 731–740. https://doi.org/https://doi.org/10.1016/j.compgeo.2011.02.004.

Peng, W., Gu, B., Yang, H., Yang, X., and Yu, Z., 2022. Analysis method for consolidation of soil under vacuum preloading assisted by air booster. Mar. Georesources Geotechnol., Taylor & Francis, 40(11), 1397–1401. https://doi.org/10.1080/1064119X.2021.2001611.

Peters, G. P., and Smith, D. W., 1998. One-dimensional contaminant transport through a consolidating soil: Application to contaminant transport through a geocomposite liner. Poromechanics, CRC Press, 481–486.

Peters, G. P., and Smith, D. W., 2002. Solute transport through a deforming porous medium. Int. J. Numer. Anal. Methods Geomech., 26(7), 683–717. https://doi.org/10.1002/nag.219.

Pham, H. Q., and Fredlund, D. G., 2011. Volume-mass unsaturated

soil constitutive model for drying-wetting under isotropic loading-unloading conditions. Can. Geotech. J., 48(2), 280–313. https://doi.org/10.1139/T10-061.

Potter, L. J., Savvidou, C., and Gibson, R. E., 1994. Consolidation and pollutant transport associated with slurried mineral waste disposal. 1st Int. Congr. Environ. Geotech., Edmonton, Canada, 525–530.

Pu, H., and Fox, P. J., 2015. Consolidation-Induced Solute Transport for Constant Rate of Strain. I: Model Development and Simulation Results. J. Geotech. Geoenvironmental Eng., 141(4), 04014127. https://doi.org/10.1061/(asce)gt.1943-5606.0001171.

Pu, H., and Fox, P. J., 2016. Model for Coupled Large Strain Consolidation and Solute Transport in Layered Soils. Int. J. Geomech., 16(2), 04015064. https://doi.org/10.1061/(asce)gm.1943-5622.0000539.

Pu, H., Wang, K., Qiu, J., and Chen, X., 2020. Large-strain numerical solution for coupled self-weight consolidation and contaminant transport considering nonlinear compressibility and permeability. Appl. Math. Model., Elsevier Inc., 88, 916–932. https://doi.org/10.1016/j.apm.2020.07.010.

Purnaditya, N. P., Soeryantono, H., Marthanty, D. R., and Sjah, J., 2019. Alternating direction implicit scheme as Finite-Difference method to solve coupled groundwater flow and contaminant transport model in the coastal aquifer. J. Phys. Conf. Ser., 1218(1), 0–9. https://doi.org/10.1088/1742-6596/1218/1/012006.

Qi, S., Simms, P., Daliri, F., and Vanapalli, S., 2020. Coupling elasto-

plastic behaviour of unsaturated soils with piecewise linear large-strain consolidation. Geotechnique, 70(6), 518–537. https://doi.org/10.1680/jgeot.18.P.261.

Qi, S., Simms, P., and Vanapalli, S., 2017a. Piecewise-linear formulation of coupled large-strain consolidation and unsaturated flow. I: Model development and implementation. J. Geotech. Geoenvironmental Eng., 143(7), 1–11. https://doi.org/10.1061/(ASCE)GT.1943-5606.0001657.

Qi, S., Simms, P., Vanapalli, S., and Soleimani, S., 2017b. Piecewise-linear formulation of coupled large-strain consolidation and unsaturated flow. II: Testing and performance. J. Geotech. Geoenvironmental Eng., 143(7), 1–12. https://doi.org/10.1061/(ASCE)GT.1943-5606.0001658.

Qin, A., Sun, D., Yang, L., and Weng, Y., 2010. A semi-analytical solution to consolidation of unsaturated soils with the free drainage well. Comput. Geotech. https://doi.org/10.1016/j.compgeo.2010.07.006.

Qiu, Q. C., Mo, H. H., and Dong, Z. L., 2007a. Vacuum pressure distribution and pore pressure variation in ground improved by vacuum preloading. 1445, 1433–1445. https://doi.org/10.1139/T07-064.

Qiu, Q. C., Mo, H. H., and Dong, Z. L., 2007b. Vacuum pressure distribution and pore pressure variation in ground improved by vacuum preloading. Can. Geotech. J., 44(12), 1433–1445. https://doi.org/10.1139/T07-064.

Quiben, J. M., 2005. Experimental and analytical study of two-phase pressure drops during evaporation in horizontal tubes. Université Pierre et Marie Curie.

Rahardjo, H., 1990. The study of undrained and drained behaviour of unsaturated soils. University of Saskatchewan.

Rujikiatkamjorn, C., Indraratna, B., and Chu, J., 2007. Numerical modelling of soft soil stabilized by vertical drains, combining surcharge and vacuum preloading for a storage yard. Can. Geotech. J., article, NRC Research Press, Ottawa, Canada, 44(3), 326–342. https://doi.org/10.1139/T06-124.

Rujikiatkamjorn, C., Indraratna, B., and Chu, J., 2008. 2D and 3D Numerical Modeling of Combined Surcharge and Vacuum Preloading with Vertical Drains. Int. J. Geomech., 8(2), 144–156. https://doi.org/10.1061/(ASCE)1532-3641(2008)8:2(144).

Sadatomi, M., Sato, Y., and Saruwatari, S., 1982. Two-phase flow in vertical noncircular channels. Int. J. Multiph. Flow, Pergamon, 8(6), 641–655. https://doi.org/10.1016/0301-9322(82)90068-4.

Seneviratne, N. H., Fahey, M., Newson, T. A., and Fujiyasu, Y., 1996. Numerical modelling of consolidation and evaporation of slurried mine tailings. Int. J. Numer. Anal. Methods Geomech., Wiley Online Library, 20(9), 647–671.

Sharipov, F., 2004. Numerical simulation of rarefied gas flow through a thin orifice. J. Fluid Mech., Cambridge University Press, 518, 35–60.

Shen, Y., Wang, H., Tian, Y., Feng, R., Liu, J., and Wu, L., 2015. A

new approach to improve soft ground in a railway station applying air-boosted vacuum preloading. Geotech. Test. J., 38(4), 373–386. https://doi.org/10.1520/GTJ20140106.

Sheng, D., Fredlund, D. G., and Gens, A., 2008a. A new modelling approach for unsaturated soils using independent stress variables. Can. Geotech. J., 45(4), 511–534. https://doi.org/10.1139/T07-112.

Sheng, D., Gens, A., Fredlund, D. G., and Sloan, S. W., 2008b. Unsaturated soils: From constitutive modelling to numerical algorithms. Comput. Geotech., 35(6), 810–824. https://doi.org/10.1016/j.compgeo.2008.08.011.

Shi, L., Wang, Q. qi, Xu, S. lin, Pan, X. dong, Sun, H. lei, and Cai, Y. qiang., 2018. Numerical study on clogging of prefabricated vertical drain in slurry under vacuum loading. Granul. Matter, Springer Berlin Heidelberg, 20(4), 1–14. https://doi.org/10.1007/s10035-018-0846-6.

Shuai, F., 1996a. Simulation of swelling pressure measurements on expansive soils. The University of Saskatchewan.

Shuai, F., 1996b. Simulation of swelling pressure measurements on expansive soils. Saskatoon, SK, Canada: University of Saskatchewan.

Smith, D. W., 2000. One-dimensional contaminant transport through a deforming porous medium: Theory and a solution for a quasi-steady-state problem. Int. J. Numer. Anal. Methods Geomech., 24(8), 693–722. https://doi.org/10.1002/1096-9853(200007)24:8<693::AID-NAG91>3.0.CO;2-E.

Song, D.-B., Pu, H.-F., Yin, Z.-Y., Min, M., and Qiu, J.-W., 2023. Plane-strain model for large strain consolidation induced by vacuum-assisted prefabricated horizontal drains. Int. J. Numer. Anal. Methods Geomech., 47(10), 1911–1935. https://doi.org/https://doi.org/10.1002/nag.3544.

Staker, S. W., Holloway, C. L., Bhobe, A. U., and Piket-May, M., 2003. Alternating-direction implicit (ADI) formulation of the finite-difference time-domain (FDTD) method: Algorithm and material dispersion implementation. IEEE Trans. Electromagn. Compat., IEEE, 45(2), 156–166. https://doi.org/10.1109/TEMC.2003.810815.

Sun, J., and Lu, M., 2023. Analytical solutions for consolidation of soft soil improved by air-boosted vacuum preloading considering clogging effect. Int. J. Numer. Anal. Methods Geomech., (September 2022), 1830–1851. https://doi.org/10.1002/nag.3540.

Swamee, P. K., and Swamee, N., 2007. Full-range pipe-flow equations. J. Hydraul. Res., 45(6), 841–843. https://doi.org/10.1080/00221686.2007.9521821.

Tang, Y., Taiebat, H. A., and Russell, A. R., 2018. Numerical Modeling of Consolidation of Unsaturated Soils Considering Hydraulic Hysteresis. Int. J. Geomech., 18(2), 04017136. https://doi.org/10.1061/(asce)gm.1943-5622.0001047.

Terzaghi, K., 1943. Theory of Consolidation. Theor. Soil Mech., Wiley Online Books. https://doi.org/doi:10.1002/9780470172766.ch13.

The Bentley System Team., 2020. SVSOILS.

Thomas, L. H., 1949. Elliptic problems in linear difference equations

over a network. Watson Sci. Comput. Lab. Rept., Columbia Univ. New York, 1, 71.

Vallée, C., Höhne, T., Prasser, H.-M., and Sühnel, T., 2008. Experimental investigation and CFD simulation of horizontal stratified two-phase flow phenomena. Nucl. Eng. Des., 238(3), 637–646.

Vu, H. Q., and Fredlund, D. G., 2006. Challenges to modelling heave in expansive soils. Can. Geotech. J., 43(12), 1249–1272. https://doi.org/10.1139/T06-073.

Wang, J., Cai, Y., Ma, J., Chu, J., Fu, H., Wang, P., and Jin, Y., 2016. Improved Vacuum Preloading Method for Consolidation of Dredged Clay-Slurry Fill. J. Geotech. Geoenvironmental Eng., 142(11), 2–6. https://doi.org/10.1061/(asce)gt.1943-5606.0001516.

Wang, J., Ding, J., Wang, H., and Mou, C., 2020a. Large-strain consolidation model considering radial transfer attenuation of vacuum pressure. Comput. Geotech., Elsevier, 122(August 2019), 103498. https://doi.org/10.1016/j.compgeo.2020.103498.

Wang, L., Xu, Y., Xia, X., He, Y., and Li, T., 2019a. Semi-analytical solutions to two-dimensional plane strain consolidation for unsaturated soils under time-dependent loading. Comput. Geotech., 109, 144–165. https://doi.org/10.1016/j.compgeo.2019.01.002.

Wang, L., Xu, Y., Xia, X., He, Y., and Li, T., 2019b. Semi-analytical solutions to two-dimensional plane strain consolidation for unsaturated soils under time-dependent loading. Comput.

Geotech., 109, 144–165. https://doi.org/https://doi.org/10.1016/j.compgeo.2019.01.002.

Wang, L., Xu, Y., Xia, X., and Sun, D., 2018. Semi-analytical solutions to two-dimensional plane strain consolidation for unsaturated soil. Comput. Geotech., 101, 100–113. https://doi.org/https://doi.org/10.1016/j.compgeo.2018.04.015.

Wang, L., Xu, Y., Xia, X., and Zhou, A., 2020b. Semi-analytical solutions to the two-dimensional plane strain consolidation for unsaturated soil with the lateral semi-permeable drainage boundary under time-dependent loading. Comput. Geotech., Elsevier, 124, 103562.

Wang, L., Zhou, A., Xu, Y., and Xia, X., 2020c. Consolidation of unsaturated composite ground reinforced by permeable columns. Comput. Geotech., Elsevier, 125, 103706.

Wheeler, S. J., Sharma, R. S., and Buisson, M. S. R., 2003. Coupling of hydraulic hysteresis and stress–strain behaviour in unsaturated soils. Géotechnique, 53(1), 41–54. https://doi.org/10.1680/geot.2003.53.1.41.

Wu, B., Firouzi, M., Mitchell, T., Rufford, T. E., Leonardi, C., and Towler, B., 2017. A critical review of flow maps for gas-liquid flows in vertical pipes and annuli. Chem. Eng. J., Elsevier. https://doi.org/10.1016/j.cej.2017.05.135.

Wu, S., 2019. Numerical Simulation for Solute Transport in a Deformable Porous Medium.

Wu, S., Jeng, D. S., and Seymour, B. R., 2020. Numerical Modelling of

consolidation-induced solute transport in unsaturated soil with dynamic hydraulic conductivity and degree of saturation. Adv. Water Resour., 135(May 2019). https://doi.org/10.1016/j.advwatres.2019.103466.

Xu, Y., and Fang, X., 2014. Correlations of void fraction for two-phase refrigerant flow in pipes. Appl. Therm. Eng., Elsevier, 64(1–2), 242–251.

Yang, S.-F., Lou, Y., Dong, Z.-L., Mo, H.-H., Chen, P.-S., and Zhou, R.-B., 2014. Causes and countermeasures for vacuum consolidation failure of newly-dredged mud foundation. Chinese J. Geotech. Eng., 36(7), 1350–1359. https://doi.org/10.11779/CJGE201407020.

Yao, D. T. C., de Oliveira-Filho, W. L., Cai, X., and Znidarcic, D., 2002. Numerical solution for consolidation and desiccation of soft soils. Int. J. Numer. Anal. Methods Geomech., Wiley Online Library, 26(2), 139–161.

Yao, K., Cheng, D., Sheng, J., Shi, L., Hu, L., and Yu, Y., 2023. Real-Time Behaviour of Dredged Slurry Treated by Air-Booster Vacuum Consolidation. Appl. Sci., 13(6), 3550. https://doi.org/10.3390/app13063550.

Yu, C., Liu, J., Ma, J., and Yu, X., 2018. Study on transport and transformation of contaminant through layered soil with large deformation. Environ. Sci. Pollut. Res., Environmental Science and Pollution Research, 25(13), 12764–12779. https://doi.org/10.1007/s11356-018-1325-7.

Zhang, D., Liu, S., and Chen, L., 2008. Fracturing Mechanism in Soils with Three Dimension Stress State. GeoCongress 2008, Proceedings. https://doi.org/doi:10.1061/40970(309)68.

Zhang, H. J., Jeng, D. S., Barry, D. A., Seymour, B. R., and Li, L., 2013. Solute transport in nearly saturated porous media under landfill clay liners: A finite deformation approach. J. Hydrol., 479, 189–199. https://doi.org/10.1016/j.jhydrol.2012.11.063.

Zhang, H. J., Jeng, D. S., Seymour, B. R., Barry, D. A., and Li, L., 2012. Solute transport in partially-saturated deformable porous media: Application to a landfill clay liner. Adv. Water Resour., 40(Ccl), 1–10. https://doi.org/10.1016/j.advwatres.2012.01.007.

Zhou, A. N., Sheng, D., Sloan, S. W., and Gens, A., 2012. Interpretation of unsaturated soil behaviour in the stress - Saturation space, I: Volume change and water retention behaviour. Comput. Geotech., Elsevier Ltd, 43, 178–187. https://doi.org/10.1016/j.compgeo.2012.04.010.

Zhou, A., and Sheng, D., 2015. An advanced hydro-mechanical constitutive model for unsaturated soils with different initial densities. Comput. Geotech., Elsevier Ltd, 63, 46–66. https://doi.org/10.1016/j.compgeo.2014.07.017.

Zhou, W. H., 2013. Axisymmetric consolidation of unsaturated soils by differential quadrature method. Math. Probl. Eng., 2013. https://doi.org/10.1155/2013/497161.

Zhou, Y., Deng, A., and Wang, C., 2013. Finite-difference model for one-dimensional electro-osmotic consolidation. Comput. Geotech.,

Elsevier Ltd, 54, 152–165.
https://doi.org/10.1016/j.compgeo.2013.06.003.

Appendix A. Initial pore pressures induced by surcharge load

The pore pressures at location (*x*, *y*), u^w and u^a, that are induced by a surcharge load *p* are herein summarised in terms of Fredlund and Rahardjo (1993) and Fredlund et al. (2012). Assuming a K_0 loading condition for the layer in Figure 2-1(a), the soil volume change ratio, dV^v/V_0, can be expressed by using the net stress increment, $d(\sigma_y - u^a)$, and matric suction increment, $d(u^a - u^w)$:

$$\frac{dV^v}{V_0} = m_1 d\left(\sigma_y - u^a\right) + m_2 d\left(u^a - u^w\right) \quad \text{(A-1)}$$

where V^v is the volume of void. The volume change ratio can also be expressed in terms of pore−fluid compressibility:

$$\frac{dV^v}{V_0} = C^{aw} n d\sigma_y \quad \text{(A-2)}$$

where *n* is the soil porosity, and C^{aw} is the coefficient of air−water compressibility and is expressed as:

$$C^{aw} = SC^w \left(\frac{du^w}{d\sigma_y}\right) + \left(\frac{1 - S + hS}{u^a_{abs}}\right)\left(\frac{du^a}{d\sigma_y}\right) \quad \text{(A-3)}$$

where *S* is the degree of saturation, C^w is the compressibility of water and equals 4.2×10^{-7} kPa^{-1} at 293.1 K and 1 atm, and *h* is the volumetric coefficient of solubility and is 0.02.

Combining Eqs. (A-1) to (A-3) and rearranging it, the change in pore water pressure, du^w, is rewritten as:

$$du^w = R_1 du^a + R_2 d\sigma_y \tag{A-4}$$

where coefficients R_1 and R_2 are:

$$\begin{cases} R_1 = \dfrac{m_2 - m_1 - \left[\dfrac{(1-S+hS)(n)}{u^a_{abs}}\right]}{m_2 + SnC^w} \\ R_2 = \dfrac{m_1}{m_2 + SnC^w} \end{cases} \tag{A-5}$$

Eq. (A-4) consists of two unknowns, i.e., du^w and du^a, and can be solved by introducing air volume compressibility relationship which is as follows:

$$\frac{dV^a}{V_0} = m_1^a d\left(\sigma_y - u^a\right) + m_2^a d\left(u^a - u^w\right) \tag{A-6}$$

Based on compressibility of air, the air volume change ratio, dV^a/V_0, can be also expressed as:

$$\frac{dV^a}{V_0} = \left(\frac{(1-S+hS)n}{\bar{u}^a}\right) du^a \tag{A-7}$$

Combining Eqs. (A-6) and (A-7), du^a can be expressed using du^w and $d\sigma_y$ as follows:

$$du^a = R_3\left(du^w\right) + R_4\left(d\sigma_y\right) \tag{A-8}$$

where coefficients R_3 and R_4 are:

$$\begin{cases} R_3 = \dfrac{m_2^a}{m_2^a - m_1^a - \left[\dfrac{(1-S+hS)n}{u^a_{abs}}\right]} \\ R_4 = \dfrac{m_1^a}{m_2^a - m_1^a - \left[\dfrac{(1-S+hS)n}{u^a_{abs}}\right]} \end{cases} \tag{A-9}$$

Solving the combination of Eqs. (A-4) and (A-8), the changes in pore air and pore water pressure are written as:

$$\begin{cases} du^a = \dfrac{R_2 R_3 - R_4}{1 - R_1 R_3} d\sigma_y \\ du^w = \dfrac{R_2 - R_1 R_4}{1 - R_1 R_3} d\sigma_y \end{cases} \tag{A-10}$$

Apparently, the three stress increments represent the excess pore pressures and surcharge load respectively, i.e. $du^a = u_0^a$, $du^w = u_0^w$ and $\sigma_y = p$.

It is noteworthy that coefficients R_1, R_3 and R_4 contain the absolute pore air pressure $u_{abs}^a = u^a + u_{atm}^a$. Excess pore pressure u^a is an unknown in the first instance and therefore has to be solved by iterations.

Appendix B. Hydro-mechanical model

The model adapted constitutive relationships as given in Fredlund and Xing (1994), Shuai (1996) and Fredlund et al. (2002). The drying curve is given as:

$$w(\psi) = w_s \left[1 - \frac{\ln\left(1+\frac{\psi}{h_r}\right)}{\ln\left(1+\frac{10^6}{h_r}\right)} \right] \left[\frac{1}{\left[\ln\left[\exp(1) + \left(\frac{\psi}{a_f} \right)^{n_f} \right] \right]^{m_f}} \right] \tag{B-1}$$

where w_s is the saturated water content, h_r is the residual matric suction, and a_f, n_f and m_f are the curve fitting parameters. Differentiating Eq. (B-1) with respective to matric suction ψ yields parameter b_m. Substituting b_m to Eq. (2-40) gives the coefficient of water volume change with respect to the matric suction as:

$$m_2^w = \frac{w_s G_s}{1+e_0} \left(\begin{array}{c} -\dfrac{1}{\ln\left(\frac{10^6}{h_r}+1\right)(\psi+h_r)\left(\ln\left(\exp(1)a_f^{n_f}+\psi^{n_f}\right)-n_f\ln\left(a_f\right)\right)^m} \\ -\dfrac{n_f m_f \psi^{n_f-1}\left(\ln\left(1+\frac{10^6}{h_r}\right)-\ln\left(1+\frac{\psi}{h_r}\right)\right)\left(\ln\left(\exp(1)a_f^{n_f}+\psi^{n_f}\right)-n_f\ln\left(a_f\right)\right)^{-m_f-1}}{a_f^{n_f}\ln\left(\frac{h_r+10^6}{h_r}\right)\left(\exp(1)+\left(\frac{\psi}{a_f}\right)^{n_f}\right)} \end{array} \right) \tag{B-2}$$

Fredlund et al. (2002) represented soil shrinkage curve as:

$$e(w) = a_{sh}\left[\frac{w^{c_{sh}}}{b_{sh}^{\,c_{sh}}} + 1\right]^{\frac{1}{c_{sh}}} \tag{B-3}$$

where a_{sh} is the minimum void ratio, b_{sh} is the slope of the line of tangency, and c_{sh} is the curvature of the shrinkage curve.

Differentiating Eq. (B-3) with respective to the water content gives:

$$\frac{de}{dw} = a_{sh} w^{(c_{sh}-1)} \frac{\left(w^{c_{sh}} + b_{sh}^{c_{sh}}\right)^{\frac{1-c_{sh}}{c_{sh}}}}{b_{sh}} \tag{B-4}$$

Substituting Eq. (B-1) to Eq. (B-4) and considering Eq. (2-40), the coefficient of soil volume change with respected to the matric suction, m_2, becomes:

$$m_2 = \frac{w_s a_{sh}}{1+e_0} \frac{\left(\left[w_s\left[1-\frac{\ln\left(1+\frac{\psi}{h_r}\right)}{\ln\left(1+\frac{10^6}{h_r}\right)}\right]\left[\frac{1}{\left[\ln\left[\exp(1)+\left(\frac{\psi}{a_f}\right)^{n_f}\right]\right]^{m_f}}\right]\right]^{c_{sh}} + b_{sh}^{c_{sh}}\right)^{\frac{1-c_{sh}}{c_{sh}}}}{b_{sh}}$$
$$\left[w_s\left[1-\frac{\ln\left(1+\frac{\psi}{h_r}\right)}{\ln\left(1+\frac{10^6}{h_r}\right)}\right]\left[\frac{1}{\left[\ln\left[\exp(1)+\left(\frac{\psi}{a_f}\right)^{n_f}\right]\right]^{m_f}}\right]\right]^{c_{sh}-1}$$
$$\left(-\frac{1}{\ln\left(\frac{10^6}{h_r}+1\right)(\psi+h_r)\left(\ln\left(\exp(1)a_f^{n_f}+\psi^{n_f}\right)-n_f\ln(a_f)\right)^m}\right.$$
$$\left.-\frac{n_f m_f \psi^{n_f-1}\left(\ln\left(1+\frac{10^6}{h_r}\right)-\ln\left(1+\frac{\psi}{h_r}\right)\right)\left(\ln\left(\exp(1)a_f^{n_f}+\psi^{n_f}\right)-n_f\ln(a_f)\right)^{-m_f-1}}{a_f^{n_f}\ln\left(\frac{h_r+10^6}{h_r}\right)\left(\exp(1)+\left(\frac{\psi}{a_f}\right)^{n_f}\right)}\right) \tag{B-5}$$

In Shuai (1996), the compressibility curve gives:

$$a_t = 0.435 C_c \psi^{-\frac{\psi}{C_{a1}+\psi C_{a2}}} \tag{B-6}$$

where C_c is the compression index, C_{a1} and C_{a2} are the fitting parameters. Substituting Eq. (B-6) to Eq. (2-40), the coefficient of soil volume change with respected to the net stress, m_1, is:

$$m_1 = \frac{0.435 C_c \psi^{-\frac{\psi}{C_{a1}+\psi C_{a2}}}}{1+e_0} \qquad \text{(B-7)}$$

As per Shuai (1996), the coefficient of water volume change with respected to the net stress, m_1^w, becomes :

$$m_1^w = \frac{0.435 C_c \psi^{-\frac{\psi}{C_{a1}+\psi C_{a2}}}}{1+e_0} \psi^{-C_e} \qquad \text{(B-8)}$$

where C_e is an index that shows the relationship between water (m_1^w) and soil (m_1^s) volume change indexes in term of the matrix suction. The index is determined experimentally.

Appendix C. Model derivation

As per Fredlund et al. (2012), the unsaturated soil volume change indexes, m_1^w, m_2^w, are reduced to the fully saturated soil volume change index, m_v. In fully saturated condition, the Eq. (3-3) is simplified to:

$$\frac{\partial e^w}{\partial t} = m_v \left(1+e_0\right) \frac{\partial}{\partial t}\left[\sigma_x + \sigma_y - u^w\right] \quad \text{(C-1)}$$

The change of total stress with respect to time, $\partial\sigma_y / \partial t$, is expressed as:

$$\frac{\partial \sigma_y}{\partial t} = \frac{\partial \sigma_y}{\partial \xi}\frac{\partial \xi}{\partial t} \quad \text{(C-2)}$$

The term $\partial\sigma_y / \partial\xi$ equals $\rho^s g$, and the Eq.(C-2) is then written as:

$$\frac{\partial \sigma_y}{\partial t} = -\frac{\Delta y \rho^s g}{1+e_0}\frac{\partial e^w}{\partial t} \quad \text{(C-3)}$$

The pore water pressure, u^w, is the sum of the hydrostatic pressure, $u^{w,hst}$, and the excess pore water pressure, u'^w, and the change of pore water pressure with respect to time, $\partial u^w / \partial t$, is expressed as:

$$\frac{\partial u^w}{\partial t} = \frac{\partial u^{w,hst}}{\partial t} + \frac{\partial u'^w}{\partial t} \quad \text{(C-4)}$$

And similarly, the term $\partial u^{w,hst} / \partial t$ is written as $\left(\partial u^{w,hst} / \partial \xi\right)\left(\partial \xi / \partial t\right)$, and Eq. (C-4) becomes:

$$\frac{\partial u^w}{\partial t} = -\frac{\Delta y \rho^w g}{1+e_0}\frac{\partial e^w}{\partial t} + \frac{\partial u'^w}{\partial t} \quad \text{(C-5)}$$

Substituting Eqs. (C-3) and (C-5) into Eq. (C-1), and assuming the change of horizontal stress during the consolidation is neglected, the change of void ratio with respect to time, $\partial e^w / \partial t$, is written as:

$$\frac{\partial e^w}{\partial t} = -\frac{m_v\left(1+e_0\right)}{1+m_v\Delta y\left(\rho^s-\rho^w\right)g}\frac{\partial u'^w}{\partial t} \tag{C-6}$$

Combining Eqs. (C-6) and (3-2), the governing equation for excess pore water pressure dissipation in the fully saturated condition is simplified as:

$$\frac{\partial u'^w}{\partial t} = -\frac{k_\xi^w\left(1+e^{w0}\right)\left(1+m_v\Delta y\left(\rho^s-\rho^w\right)g\right)}{\gamma^w m_v\left(1+e^w\right)}\frac{\partial^2 u'^w}{\partial y^2} - \frac{k_x^w\left(1+e^w\right)\left(1+m_v\Delta y\left(\rho^s-\rho^w\right)g\right)}{\gamma^w m_v\left(1+e^{w0}\right)}\frac{\partial^2 u'^w}{\partial x^2} \tag{C-7}$$

where, as per Lambe and Whitman (1979) and Lewis et al. (2009), the volume change index, m_v, is written as:

$$m_v = \frac{Cc10^{\left(e^w-e^{w0}\right)/Cc}}{\sigma'_0\ln(10)\left(1+e^{w0}\right)} \tag{C-8}$$

Appendix D. Pressure drop at orifice

Pipe pressure will drop when a mass of air enters the pipe through an orifice. Adapting Eq. (5-3), the pressure drop at Orifice 1 is written as:

$$\Delta P_1 = \frac{1}{2}\rho_{g1} v_{g,O1}^2 \tag{D-1}$$

where the density of air, ρ_{g1}, is determined from the Ideal Gas Law, as

$$\rho_{g1} = \frac{MP_1}{RT} \tag{D-2}$$

where M is the molar mass of air and is 28.97 g/mol for dry air, P_1 is the pipe pressure at Orifice 1, R is the ideal gas constant of 8.314 J/(K $\cdot$ mol), and T is the temperature of air in Kelvin. In Eq. (D-1), the air velocity at the orifice $v_{g,O1}$ is determined from the air mass flow rate $\dot{m}_{g,O1}$ as:

$$v_{g,O1} = \frac{\dot{m}_{g,O1}}{\rho_{g1}\left(\frac{\pi d_1^2}{4}\right)} \tag{D-3}$$

where d_1 is the diameter of Orifice 1. Substituting Eq. (D-2) for Eq. (D-3), gives

$$v_{g,O1} = \frac{4\dot{m}_{g,O1}}{MP_1\pi d_1^2} RT \tag{D-4}$$

Substituting Eqs. (D-2) and (D-4) for Eq. (D-1), the pressure drop at Orifice 1 is:

$$\Delta P_1 = \frac{8\left(\dot{m}_{g,O1}\right)^2 RT}{MP_1\left(\pi d_1{}^2\right)^2} \quad \text{(D-5)}$$

Appendix E. Gas volume ratio

As per Hibiki et al. (2004), the gas volume ratio, α, of a gas–liquid mixture transporting in a pipeline is determined as:

$$\alpha = \frac{v_g}{v_{gm} + C_0 v_m} \tag{E-1}$$

where v_{gm} is the drift-flux velocity, v_m is the mixture velocity and equals (v_l + v_g) (Afshin and Swanand 2014), and v_g is the velocity of air and equals

$$v_g = \frac{m_g}{MP_1 D} RT \tag{E-2}$$

where m_g is the cumulative mass flow rate of air, D is the pipe diameter, and C_0 is the distribution parameter and is written as:

$$C_0 = \frac{2 - \left(\rho_g / \rho_l\right)^2}{1 + \left(Re_m / 1000\right)^2} + \frac{\left\{\left[\left(1 + \left(\rho_g / \rho_l\right)^2 \cos\theta\right) / \left(1 + \cos\theta\right)\right]^{\frac{1-\alpha_g}{2}}\right\}^{2/5} + C_{0,1}}{1 + \left(Re_m / 1000\right)^2} \tag{E-3}$$

where θ is the pipe orientation angle from horizontal, Re_m is the mixture Reynold number and equals ($v_m \rho_l D / \mu_l$) where μ_l is the liquid dynamic viscosity, and $C_{0,1}$ is a variable and is written as:

$$C_{0,1} = \left(c_1 - c_1\sqrt{\rho_g / \rho_l}\right)\left[\left(2.6 - \lambda\right)^{0.15} - \sqrt{f_M}\right]\left(1 - x\right)^{1.5} \tag{E-4}$$

where, the constant c_1 is 0.2 for a circular pipe, λ is the gas to mixture velocity ratio, i.e. (v_g/v_m), x is the gas to mixture mass flow rate ratio and equals ($m_g/(m_g+m_l)$), and f_m is the friction factor and is determined by substituting the mixture velocity for the liquid friction factor equation in Swamee and Swamee (2007), as:

$$f_m = \left\{ \left(\frac{64}{Re_m} \right)^8 + 9.5 \left[\ln \left(\frac{\varepsilon}{3.7d} + \frac{5.74}{Re_m^{0.9}} \right) - \left(\frac{2500}{Re_m} \right)^6 \right]^{-16} \right\}^{0.125} \quad \text{(E-5)}$$

where ε is the pipe roughness height and equals 0.0015 mm for smooth pipe.

The drift-flux velocity, v_{gm}, in Eq. (E-1) is written as:

$$v_{gm} = c_2 c_3 \left(0.35 \sin\theta + 0.45 \cos\theta \right) \sqrt{\frac{g d_n \left(1-\alpha\right)\left(\rho_l - \rho_g\right)}{\rho_l}} \quad \text{(E-6)}$$

where g is the gravity acceleration, coefficient c_2 is 1 for the liquid dynamic viscosity $\mu_l \le 0.01$ Pa·s. Otherwise c_2 is written as:

$$c_2 = \left(\frac{0.434}{\log_{10}\left(\mu_l / 0.001\right)} \right)^{0.15} \quad \text{(E-7)}$$

Coefficient c_3 is related to the Laplace number, La. c_3 = 1 for $La \ge 0.025$. Otherwise c_3 is expressed as:

$$c_3 = \left(La / 0.025 \right)^{0.9} \quad \text{(E-8)}$$

Laplace number La is related to the surface tension of mixture, σ, and is determined as:

$$La = \sqrt{\frac{\sigma}{g\left(\rho_l - \rho_g\right)}} \frac{1}{d} \quad \text{(E-9)}$$

Note that Eqs. (E-1) to (E-9) are solved through iterations. Assuming an initial gas volume ratio α, calculate the required parameters to determine the new gas volume ratio. Compare the assumed and new volume ratios with the pre-set criterion. If the criterion is satisfied, the gas volume ratio is accepted. otherwise, adjust it until the criterion is satisfied.

Appendix F. Two-phase frictional pressure factor

As per Bhagwat (2015) and Ghajar (2020), the factor, Φ, for two-phase friction pressure is given as:

$$\Phi^2 = \left\{(1-x)^{0.33}\left[1+B_1 x\left(Y^2-1\right)\right]+B_2 Y^2 x^3\right\}\left[1+B_3(1-x)^2\right] \quad \text{(F-1)}$$

where, Y is the parameter determined from Müller-Steinhagen and Heck's equation (Müller-Steinhagen and Heck 1986) as:

$$Y = \sqrt{\frac{\dot{P}_{frict,g}}{\dot{P}_{frict,l}}} \quad \text{(F-2)}$$

where $\dot{P}_{frict,g}$ is the pressure gradient of the gas by assuming the gas flows at the mixture mass flux, and is written as:

$$\dot{P}_{frict,g} = 2 f_g \frac{4\left(\dot{m}_g+\dot{m}_l\right)^2}{\pi \rho_g d^3} \quad \text{(F-3)}$$

where f_g is the gas friction factor and determined using the method for the liquid friction factor.

The fitting parameters, B_1, B_2, and B_3 are given as:

$$B_1 = \left\{0.85+1.703\left[1-\exp\left(-6.25\zeta Bo\right)\right]\right\}\Pi_1\Pi_2\Pi_3 \quad \text{(F-4)}$$

$$B_2 = 1-\sqrt{\rho_g/\rho_l} \quad \text{(F-5)}$$

$$B_3 = \begin{cases} -0.3\left(1+\sin\theta\right)^{-16.25}+0.3 & \text{for } 0° \le \theta \le 20° \\ -0.012\left(1+\sin\theta\right)^{4.1}+0.34 & \text{for } 20° < \theta \le 90° \end{cases} \quad \text{(F-6)}$$

where:

$$\Pi_1 = \left\{1 + 2.65\left[1 - \exp\left(-1.677 N_{\mu l}\right)\right]\right\} \tag{F-7}$$

$$\Pi_2 = \begin{cases} 0.55 \text{ for } \zeta \le 1,\ Bo \ge 1 \\ 1 \quad \text{for } \zeta > 1,\ Bo < 1 \end{cases} \tag{F-8}$$

$$\Pi_3 = \sqrt{1 + 0.005\frac{1-x}{x}} \tag{F-9}$$

$$Bo = \frac{g\left(\rho_l - \rho_g\right)\left(d/2\right)^2}{\sigma} \tag{F-10}$$

$$N_{\mu l} = \frac{\mu_l}{\left[\rho_l \sigma \sqrt{\frac{\sigma}{g\left(\rho_l - \rho_g\right)}}\right]^{0.5}} \tag{F-11}$$

$$\zeta = 2.5\sqrt{\frac{\rho_l}{\rho_{ref}}}\left(\frac{\mu_g}{\mu_l}\right)^{0.25} \tag{F-12}$$

where ρ_{ref} is the reference value of density and equals the density of water, and μ_g are dynamic viscosity of air

Appendix G. Two-phase VOF model

As per Ansys Inc. (2020)**,** the VOF model assumes the velocity field is shared among phases. A single momentum equation is solved:

$$\frac{\partial}{\partial t}\left(\rho_m \vec{V}\right)+\nabla\left(\rho_m \vec{V}\vec{V}\right)=-\nabla P+\nabla\left[\mu\left(\nabla\vec{V}+\vec{V}^T\right)\right]+\rho_m \vec{g}+\vec{F} \quad \text{(G-1)}$$

where $\vec{F}$ is the surface force vector; ρ_m and μ_m are mixture density and viscosity, and are written as:

$$\rho_m=\alpha_l\rho_l+\left(1-\alpha_l\right)\rho_g \quad \text{(G-2)}$$

$$\mu_m=\frac{\alpha_l\rho_l\mu_l+\left(1-\alpha_l\right)\rho_g\mu_g}{\alpha_l\rho_l+\left(1-\alpha_l\right)\rho_g} \quad \text{(G-3)}$$

Assuming the gas (air) is the primary phase and liquid (water) is the secondary phase, and no mass transfer between phases, the liquid volume ratio α_l satisfies the following equation:

$$\frac{\partial}{\partial t}\left(\alpha_l\right)+\nabla\left(\alpha_l\vec{V}_l\right)=0 \quad \text{(G-4)}$$